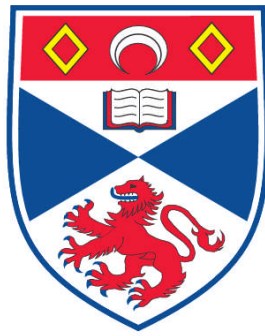


**ATMOSPHERIC TRANSPORT AND CRITICAL LAYER MIXING IN
THE TROPOSPHERE AND STRATOSPHERE**

Louise Ann Smy

**A Thesis Submitted for the Degree of PhD
at the
University of St. Andrews**



2012

**Full metadata for this item is available in
Research@StAndrews:FullText
at:**

<http://research-repository.st-andrews.ac.uk/>

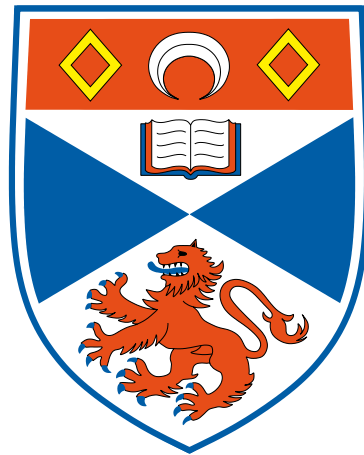
Please use this identifier to cite or link to this item:

<http://hdl.handle.net/10023/2538>

This item is protected by original copyright

Atmospheric Transport and Critical Layer Mixing in the Troposphere and Stratosphere

Louise Ann Smy



A thesis submitted for the degree of Doctor of Philosophy at the
University of St Andrews

25th October 2011

Abstract

This thesis aims to improve the understanding of transport and critical layer mixing in the troposphere and stratosphere. A dynamical approach is taken based on potential vorticity which has long been recognised as the essential field inducing the flow and thermodynamic structure of the atmosphere. Within the dynamical framework of critical layer mixing of potential vorticity, three main topics are addressed.

First, an idealised model of critical layer mixing in the stratospheric surf zone is examined. The effect of the shear across the critical layer on the critical layer evolution itself is investigated. In particular it is found that at small shear barotropic instability occurs and the mixing efficiency of the critical layer increases due to the instability. The effect of finite deformation length is also considered which extends previous work.

Secondly, the dynamical coupling between the stratosphere and troposphere is examined by considering the effect of direct perturbations to stratospheric potential vorticity on the evolution of midlatitude baroclinic instability. Both zonally symmetric and asymmetric perturbations to the stratospheric potential vorticity are considered, the former representative of a strong polar vortex, the latter representative of the stratospheric state following a major sudden warming. A comparison of these perturbations gives some insight into the possible influence of pre or post-sudden warming conditions on the tropospheric evolution.

Finally, the influence of the stratospheric potential vorticity distribution on lateral mixing and transport into and out of the tropical pipe, the low latitude ascending branch of the Brewer-Dobson circulation, is investigated. The stratospheric potential vorticity distribution in the tropical stratosphere is found to have a clear pattern according to the phase of the quasi-biennial oscillation (QBO). The extent of the QBO influence is quantified, by analysing trajectories of Lagrangian particles using an online trajectory code recently implemented in the Met Office's Unified Model.

Acknowledgements

Firstly, I would like to thank my partner Nicholas Owen and both our families for their endless love and support throughout my PhD.

Thanks to my supervisor Richard Scott for all the help, advice and encouragement that he has given me throughout my PhD. I would also like to thank the Earth System and Mitigation Science team at the Met Office in Exeter for making my visits there enjoyable. In particular I would like to thank Neal Butchart and Steven Hardiman for all of their help throughout my time in Exeter and Steven for his computing help whilst I was learning to run the Unified Model. I am also grateful to Colin Johnson who helped me to write the code that retrieves the fields, necessary to run the trajectory code, from the Unified Model.

Finally I would like to thank UK EPSRC who financially supported me throughout this project (CASE/CNA/06/76).

Declaration

1. Candidates declarations:

I, Louise Ann Smy, hereby certify that this thesis, which is approximately 35,000 words in length, has been written by me, that it is the record of work carried out by me and that it has not been submitted in any previous application for a higher degree.

I was admitted as a research student in September 2007 and as a candidate for the degree of Doctor of Philosophy in September 2008; the higher study for which this is a record was carried out in the University of St Andrews between 2007 and 2011.

Signature:..... **Date:**

2. Supervisors declaration:

I hereby certify that the candidate has fulfilled the conditions of the Resolution and Regulations appropriate for the degree of Doctor of Philosophy in the University of St Andrews and that the candidate is qualified to submit this thesis in application for that degree.

Signature:..... **Date:**

3. Permission for electronic publication:

In submitting this thesis to the University of St Andrews I understand that I am giving permission for it to be made available for use in accordance with the regulations of the University Library for the time being in force, subject to any copyright vested in the work not being affected thereby. I also understand that the title and the abstract will be published, and that a copy of the work may be made and supplied to any bona fide library or research worker, that my thesis will be electronically accessible for personal or research use unless exempt by award of an embargo as requested below, and that the library has the right to migrate my thesis into new electronic forms as required to ensure continued access to the thesis. I have obtained any third-party copyright permissions that may be required in order to allow such access and migration, or have requested the appropriate embargo below.

The following is an agreed request by candidate and supervisor regarding the electronic publication of this thesis:

- (i) Access to printed copy and electronic publication of thesis through the University of St Andrews.

Signature of Candidate:.....

Signature of Supervisor:.....

Date:

Contents

Abstract	i
Acknowledgements	iii
Declaration	iv
1 Introduction	4
1.1 Structure of the Atmosphere	4
1.2 The Governing Equations Of Atmospheric Motion	6
1.3 Atmospheric Transport and Mixing	9
1.3.1 Rossby Waves	9
1.3.2 Rossby Wave Critical Layers	11
1.3.3 Barotropic And Baroclinic Instability	13
1.3.4 Mixing And Transport Across The Tropopause	16
1.3.5 Dynamical Structure Of The Winter Stratosphere	17
1.4 Quantifying Mixing and Transport	18
1.4.1 Calculation of Effective Diffusivity	20
1.5 Outline of Thesis	27

2	Mixing in a Rossby Wave Critical Layer	29
2.1	Introduction	29
2.2	Model Description	31
2.3	Critical Layer Evolution	35
2.4	Evolution at Finite Deformation Length	40
2.4.1	The Basic State	40
2.4.2	Scaling of the Critical Layer Width	45
2.5	Conclusions	47
3	The Influence of Stratospheric Potential Vorticity on Baroclinic Instability	49
3.1	Introduction	49
3.2	Model description	53
3.3	Results	60
3.3.1	Control	60
3.3.2	Zonally Symmetric Perturbation	62
3.3.3	Asymmetric Perturbations	66
3.3.4	Influence of the basic state	72
3.4	Discussion	76
4	An Online Trajectory Model	78
4.1	Offline trajectory code	78
4.2	Online trajectory code	81
4.3	Error Analysis	83

5	The Effect of the Quasi-Biennial Oscillation on Transport and Mixing in the Stratosphere	89
5.1	Introduction	89
5.2	The Effect of the Phase of the QBO on the Potential Vorticity Structure	96
5.2.1	The QBO	96
5.2.2	Potential Vorticity Structure	97
5.2.3	Experiment Design	102
5.3	Analysis of Trajectories	108
5.3.1	In-Mixing	118
5.4	Discussion	119
6	Conclusions	123
7	Appendix: Online Trajectory Code	128
7.1	Where to Find the Online Code and How to Use It	128
7.2	Information on Parameters	129
7.2.1	Particles Initial Positions	131
7.3	Output	132
	Bibliography	135

Chapter 1

Introduction

The Earth's atmosphere is a complex environment. The atmosphere continually strives to reach a state of equilibrium by transporting warm air from the equator to the poles and cold air from the poles to the equator. At the same time this movement of air is affected by the Earth's rotation and friction at the Earth's surface. The combination of all these processes creates very complex flow patterns and behaviour which requires extensive research to fully explore and understand.

1.1 Structure of the Atmosphere

The atmosphere can be divided into layers based on its vertical temperature profile. The layer nearest the Earth's surface is known as the troposphere and it extends from the ground up to between 8 and 16km. It is a region of particular interest for meteorologists since most of our weather occurs here. The troposphere is a region of low stratification and weak potential vorticity (potential vorticity can be interpreted as the absolute circulation divided by the mass of a small volume enclosed between two isentropic surfaces). It is dynamically unsta-

ble due to baroclinic instability at middle latitudes (see section 1.3.3 for more details on baroclinic instability) and due to convection in the tropics (Shepherd, 2002). Therefore transport time-scales in the troposphere are reasonably fast and are typically a matter of hours for convective transport or a matter of days for baroclinic transport (transport due to baroclinic instability). The temperature in the troposphere decreases with height by an average of 7°C per km (Burroughs *et al.*, 1996) reaching its coldest point at the thermal tropical tropopause. The tropopause is defined as the notional boundary between the troposphere and the stratosphere (the second layer of the atmosphere). Conventionally the tropopause is defined, in terms of the thermal structure of the atmosphere, as the level where there is an abrupt change in the temperature lapse rate (Andrews *et al.*, 1987). A dynamical tropopause is defined based on the jump in potential vorticity between the troposphere and stratosphere (stratospheric potential vorticity is two orders of magnitude greater than tropospheric potential vorticity). The height of the tropopause varies with the amount of solar energy that reaches the Earth and therefore it is lowest at the poles and highest at the equator. The tropopause plays a crucial role in understanding the dynamics of the atmosphere (Haynes *et al.*, 2001).

The second layer of the atmosphere is the stratosphere which extends from the tropopause up to approximately 50km. In contrast to the troposphere, which is rather moist, the stratosphere is quite dry. The distribution of water vapour along with carbon dioxide and ozone are responsible for the thermal structure of the stratosphere by absorption of solar radiation. As the name suggests, the stratosphere is strongly stably stratified as a result of the increase in temperature with height. The dominant motions in the stratosphere are quasi-horizontal due to this strong stable stratification. The temperature in the stratosphere reaches a maximum at the stratopause (the “boundary” between the stratosphere and the mesosphere, the third layer in the atmosphere) due to the absorption of solar

ultraviolet radiation by ozone (Andrews *et al.*, 1987). In the mesosphere (50 to 80km) the concentration of ozone decreases reducing the absorption of solar ultraviolet radiation and consequently the temperature decreases with height. In the mesosphere the main dynamics are due to gravity wave breaking. Gravity waves are waves that only exist in a stably stratified fluid and their restoring force is due to gravity (*e.g.* buoyancy).

In this thesis we focus on the dynamics of the first two layers of the atmosphere, namely the troposphere and stratosphere.

1.2 The Governing Equations Of Atmospheric Motion

In order to model the atmosphere we need to understand the equations that govern atmospheric motion and then solve these simultaneously. The full equations are far too complicated to be used for research purposes and so we simplify them using many standard approximations.

The Equation of Motion (or Conservation of Momentum), assuming that viscous effects are negligible, the fluid is incompressible ($\nabla \cdot \mathbf{u} = 0$) and the horizontal length scales are much smaller than the curvature of the Earth (f-plane approximation), is detailed below

$$\frac{D\mathbf{u}}{Dt} + f\mathbf{k} \times \mathbf{u} = -\frac{\nabla p}{\rho} - \nabla\phi \quad (1.1)$$

where \mathbf{u} is the velocity, $\frac{D}{Dt}$ denotes the material derivative i.e. $\frac{\partial}{\partial t} + \mathbf{u} \cdot \nabla$, the vector quantity $f\mathbf{k}$ is known as the “planetary vorticity” where $f = 2\Omega\sin\phi$ is the coriolis frequency and denotes the vertical component of the Earth’s rotation vector (Ω), and \mathbf{k} denotes the local vertical unit vector. This equation represents

Newton's second law of motion which is the balance between force (in this case centrifugal force, coriolis force, pressure force and gravity) and acceleration. Here the centrifugal force is absorbed into the geopotential term ($\phi = gz - \frac{1}{2}\Omega^2(x^2 + y^2)$, where g is the acceleration due to gravity).

The Continuity Equation (or Conservation of Mass)

$$\frac{\partial \rho}{\partial t} + \nabla \cdot (\rho \mathbf{u}) = 0 \quad (1.2)$$

where ρ is density. This states that mass is neither created nor destroyed in a material volume.

A Thermodynamic Equation such as conservation of entropy

$$\frac{D\theta}{Dt} = 0 \quad (1.3)$$

where $\theta = T(p_s/p)^\kappa$ is the potential temperature distribution (functionally related to entropy). Here T is the temperature, p is pressure, p_s is a reference surface pressure and $\kappa = 2/7$ for the atmosphere.

An Equation of State for an ideal gas

$$p = \rho RT \quad (1.4)$$

where R is the gas constant for dry air.

A quantity of dynamical importance is Ertel's potential vorticity which is defined, following the same approximations as for the Equation of Motion, by

$$EPV = \rho^{-1} \omega_a \cdot \nabla \theta \quad (1.5)$$

where $\omega_a = \nabla \times \mathbf{u} + f\mathbf{k}$ is the absolute vorticity. Potential vorticity has long been recognised as the essential field inducing the flow and thermodynamic structure

of the atmosphere. Moreover, it is materially conserved (i.e. following the motion of fluid elements) in adiabatic and inviscid flows. Hence many aspects of geophysical flows can be described compactly in terms of potential vorticity (a scalar) dynamics (Hoskins *et al.*, 1985; Schneider *et al.*, 2003). The “invertibility principle” states that if the total mass under each isentropic surface is specified, then a knowledge of the global distribution of potential vorticity on each isentropic surface (surface of constant potential temperature, θ) and of potential temperature at the lower boundary (which within certain limitations can be considered to be part of the potential vorticity distribution (Bretherton, 1966)) is sufficient to deduce, diagnostically, all the other dynamical fields, such as winds, temperatures, geopotential heights, static stabilities, and vertical velocities, under a suitable balance condition (Andrews *et al.*, 1987). In this thesis we examine the structure of potential vorticity in a variety of different models and stratospheric contexts.

Using the standard approximations for rapidly rotating and strongly stratified flows, i.e. taking the Rossby number $Ro = \zeta/f$ (ζ denotes the vertical vorticity, $\frac{\partial v}{\partial x} - \frac{\partial u}{\partial y}$) and the Froude number $Fr = |\boldsymbol{\omega}_h|/N$ ($\boldsymbol{\omega}_h$ denotes the horizontal vorticity, $(\nabla \times \mathbf{u})_h$ and N is the buoyancy frequency) both much less than one, we arrive at the quasi-geostrophic equations (or QG equations for short). These can be written in the following convenient form:

$$\frac{D_h Q}{Dt} = 0 \quad (1.6)$$

where Q is the quasi-geostrophic potential vorticity which is conserved following motion and $\frac{D_h}{Dt} = \frac{\partial}{\partial t} + u \frac{\partial}{\partial x} + v \frac{\partial}{\partial y}$. Note that the velocity in the material derivative is the geostrophic velocity. The quasi-geostrophic potential vorticity is related to a streamfunction ψ by the linear “inversion relation”

$$Q - f = \nabla_h^2 \psi + \frac{1}{\rho_0} \frac{\partial}{\partial z} \left(\rho_0 \frac{f^2}{N^2} \frac{\partial \psi}{\partial z} \right) \quad (1.7)$$

where $\psi = \frac{p'}{\rho_0 f}$ (from geostrophic balance), p' is the pressure perturbation, f is the Coriolis frequency, N is the buoyancy frequency, and ∇_h^2 is the horizontal Laplacian. Here p' is the total pressure minus the basic-state pressure $\bar{p}_0(z)$, and $\rho_0(z) = \rho_s \exp(-z/H_\rho)$ is the basic-state density, where ρ_s is a reference surface density and H_ρ is the “density scale height”, above 7km in the atmosphere (Andrews *et al.*, 1987). Note, in general N^2 varies with height z .

From the streamfunction ψ , the two-dimensional flow field is recovered from

$$(u, v) = \left(-\frac{\partial\psi}{\partial y}, \frac{\partial\psi}{\partial x} \right). \quad (1.8)$$

1.3 Atmospheric Transport and Mixing

1.3.1 Rossby Waves

One of the most important dynamical properties of the atmosphere is its ability to support wave motions. Rossby waves are the fundamental building blocks of weather systems at midlatitudes. They are potential vorticity conserving motions that exist wherever there are large-scale potential vorticity gradients along isentropic surfaces (surfaces of constant potential temperature, θ). Rossby waves are often large-scale waves (*i.e.* large wavelength) so much so that typically they only have a few wavelengths around the whole of the Earth (Kundu & Cohen, 2004).

The dynamical mechanism of Rossby waves and Rossby wave propagation is a restoring mechanism that depends on the existence of a latitudinal gradient of potential vorticity on isentropic surfaces. Figure 1.1 shows a schematic of Rossby wave propagation on a material contour separating an area of high potential vorticity from an area of low potential vorticity. The material contour is perturbed

and this results in positive and negative potential vorticity anomalies, the circulations of which are indicated by the green arrows in Figure 1.1. The circulations of these anomalies cause part of the material contour to move polewards and part to move equatorwards. This movement is indicated by the double blue arrows in Figure 1.1 and this results in the westward movement of the wave pattern. Therefore Rossby waves propagate westward.

The depth of the atmosphere is very small compared to its horizontal scale. The trajectories of particles in the atmosphere are very shallow with the horizontal velocities being much larger than the vertical velocities. The effect of the rapid rotation of the Earth and the strong stratification in the stratosphere is to ensure vertical velocities are significantly smaller than horizontal velocities and therefore a two dimensional approximation is a reasonable one for describing large-scale motions.

The dispersion relation for a Rossby wave in two dimensions is given by

$$\omega = -\frac{\beta k}{k^2 + l^2} \quad (1.9)$$

where k and l are the x and y wavenumbers respectively and $\beta = \frac{\partial f}{\partial y}$ is the rate of change of the Coriolis parameter with y . The phase speed of the Rossby wave is

$$c = \frac{\omega}{k} = -\frac{\beta}{k^2 + l^2} \quad (1.10)$$

The negative in (1.10) is consistent with the Rossby wave phase propagation being westward.

In the atmosphere Rossby waves often exist where there is an eastward mean background flow (let's denote the speed of the mean flow by U). When this occurs the observed phase speed of the Rossby wave is

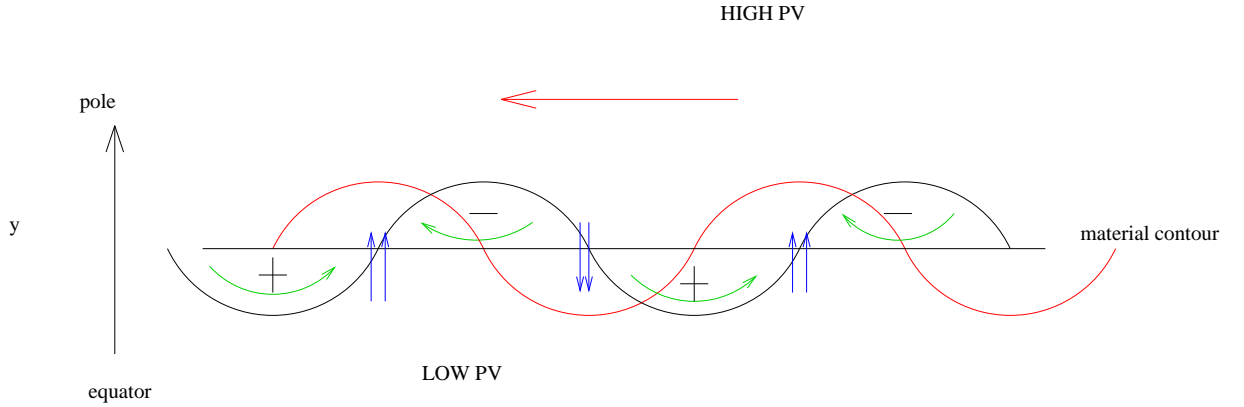


Figure 1.1: Schematic of Rossby wave propagation on a material contour.

$$c = U - \frac{\beta}{k^2 + l^2} \quad (1.11)$$

It is therefore possible to have stationary Rossby waves and they occur when the eastward mean background flow equals the westward phase speed resulting in $c = 0$.

1.3.2 Rossby Wave Critical Layers

Rossby waves propagate through a medium with a phase speed c . A critical surface (or critical line in two dimensions) occurs where the speed of the background flow equals the phase speed of the Rossby wave. Nonlinear effects become important in the region surrounding the critical surface (or critical line) and this region is known as a Rossby wave critical layer.

The evolution within the critical layer is characterised by the wrapping up of material contours of potential vorticity into the well known cat's eye pattern (see Figure 1.2). This wrapping up of potential vorticity mixes potential vorticity by moving low potential vorticity into areas of high potential vorticity and high potential vorticity into areas of low potential vorticity. After some time a zonal average of the potential vorticity will reveal that the potential vorticity is

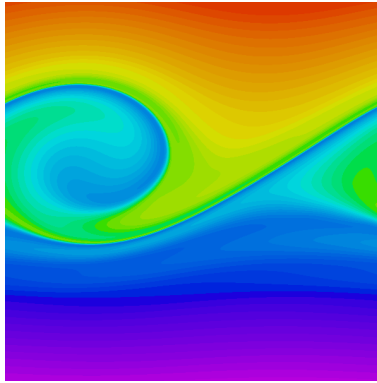


Figure 1.2: Snapshot of potential vorticity contours wrapping up into a cat's eye pattern.

homogenised across the critical layer region.

The study of critical layers goes back to the work of Benney & Bergeron (1969), Davis (1969), Dickinson (1970) and other authors. A significant advance in the theory of critical layers was made by the analytical work of Stewartson (1978) and Warn & Warn (1978) (hereafter SWW). They forced Rossby waves by flow over a corrugated boundary and applied the method of matched asymptotic expansions to the resulting critical layer. The critical layer was treated as the inner region in this analytical approach. A complete analytical solution was found for a particular choice of boundary conditions and this allowed accurate predictions to be made about the time evolution of the critical layer. One interesting prediction of the SWW solution concerned the wave motion outside the critical layer. The critical layer exerts its influence on the flow outside the critical layer and oscillates between a wave absorber (absorbs energy from incident Rossby waves) and an over-reflector (reflects the incoming wave and releases some of the wave activity previously absorbed). In the long-time limit the critical layer tends to a state of perfect reflection. The absorbing and reflecting properties of critical layers was examined further by Killworth & McIntyre (1985).

The study of critical layers is important for understanding large-scale atmo-

spheric flows. The theoretical models of Rossby wave critical layers predicted behaviour that was in broad agreement with the wave breaking structures observed by McIntyre & Palmer (1983, 1984) in coarse-grain maps of potential vorticity on isentropic surfaces in the northern winter hemisphere stratosphere. These maps of potential vorticity on isentropic surfaces made the large-scale wave breaking in the surf zone visible for the first time. In particular these maps showed the rapid and irreversible deformation of material contours along isentropic surfaces which was predicted by the theoretical models of critical layers. Therefore the study of critical layers is important for understanding Rossby wave breaking events in the atmosphere. The study of critical layers is also important for understanding the banded structures observed in our atmosphere and the atmosphere of Jupiter. Critical layers mix potential vorticity across the critical layer region leading to strong potential vorticity gradients on either side of the critical layer resembling a potential vorticity staircase (McIntyre, 1982). Critical layer mixing is therefore important for jet sharpening and recent work has focussed on the link between potential vorticity mixing and jet sharpening (Dritschel & McIntyre, 2008).

1.3.3 Barotropic And Baroclinic Instability

There are two types of instability that are important in the atmosphere, barotropic and baroclinic instability. An atmosphere, or model, is barotropic if the pressure only depends on the density and therefore surfaces of constant pressure are parallel to surfaces of constant density. The large-scale motion in a barotropic model is horizontal and does not depend on the structure in the vertical. Barotropic instability can be thought of as a horizontal shear instability. It occurs where there is non-monotonic potential vorticity, *i.e.* the potential vorticity gradient changes sign in the horizontal domain (which is dynamically unstable, (Drazin & Reid, 2004)).

In contrast to barotropic instability baroclinic instability can be thought of as a vertical shear instability (opposite signs of the latitudinal potential vorticity gradient on the upper and lower levels). In a baroclinic atmosphere, or model, density depends on both the pressure and the temperature. In the troposphere the dominant dynamics are due to baroclinic instability. We can think of baroclinic instability arising from the interaction of two Rossby waves, one at the tropopause and one at the Earth's surface (see Figure 1.3). At the surface the temperature gradient is equivalent to a negative potential vorticity gradient, *i.e.* it is opposite to the potential vorticity gradient at the tropopause. This results in the surface Rossby waves propagating eastward. There is a vertical shear associated with the surface temperature gradient (warm at the equator and cold at the pole due to the pole-equator difference in solar heating). The relationship between the vertical shear and the horizontal temperature gradient is given by the equation of thermal wind balance $\left(\frac{\partial T}{\partial y} = -\frac{\partial u}{\partial z}\right)$ which is a direct result of hydrostatic and geostrophic balance in the atmosphere. Due to the vertical shear in the troposphere the two Rossby waves, which otherwise move in opposite directions, can become phase locked. The winds strengthen in the eastward direction with increasing height due to the vertical shear. The Rossby waves at the tropopause are propagating westward with respect to the flow. However relative to the surface the Rossby waves (at the tropopause) propagate with a speed equal to their phase speed plus the background velocity. Therefore if the vertical shear is strong enough the Rossby waves (at the tropopause) will move eastwards relative to the surface which is the same direction as the surface Rossby waves. These waves can then become phase locked, keeping each other in step and if the phase is correct then the circulation of the upper potential vorticity anomalies will have an effect on the surface potential vorticity anomalies and vice versa. In this way they cause each other to grow in amplitude until they become nonlinear where they saturate and break (flow instability).

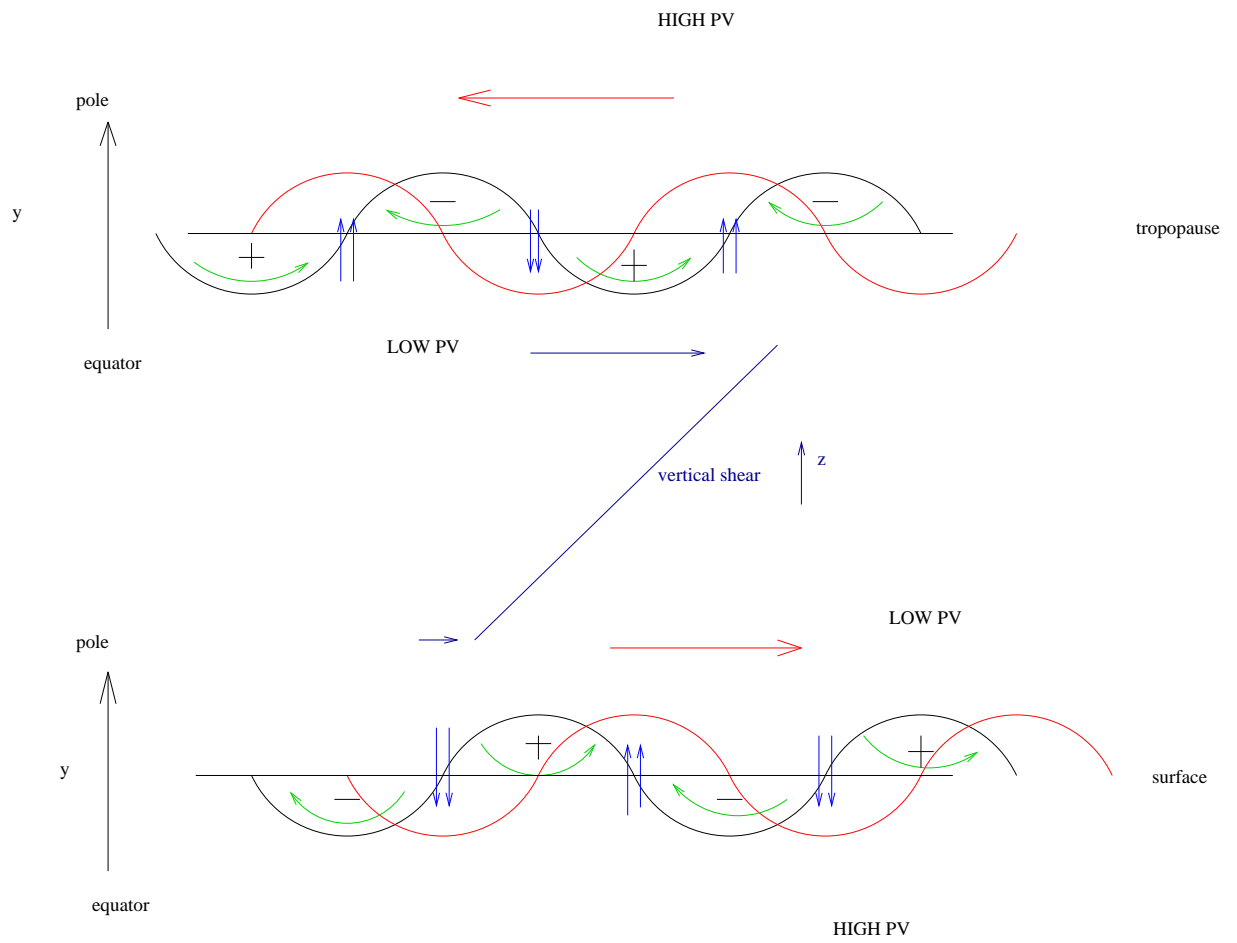


Figure 1.3: Schematic of the interaction of two Rossby waves: one at the tropopause and one at the surface.

The baroclinic eddies generated via the instability due to Rossby wave phase locking grow by extracting energy from the mean flow which is associated with the pole-equator difference in solar heating. The eddies thus generated give rise to our midlatitude weather systems and are mainly responsible for the atmospheric heat transport from the tropics to midlatitudes.

1.3.4 Mixing And Transport Across The Tropopause

Mixing and transport across the tropopause is important for understanding the distributions of chemical constituents in the troposphere and stratosphere and their consequent effects on the atmosphere, for example its thermal structure and ozone depletion.

There are many processes that contribute to transport across the tropopause. The Brewer-Dobson circulation, named after the pioneering work of Alan Brewer (1949) and Gordon Dobson (1956), is a large-scale middle atmosphere circulation. It is responsible for the long-time persistent transport of air and chemical constituents from the troposphere into the stratosphere through the tropical tropopause (for more details on the Brewer-Dobson circulation see chapter 5). Air in the tropical troposphere is drawn upwards by the Brewer-Dobson circulation, it expands due to the reducing pressure with increasing height and this expansion results in the temperature of the air decreasing (note that for adiabatic motion the temperature lapse rate is given by $-\frac{g}{c_p}$ where g is gravity and c_p is the specific heat capacity). Where this reduction in temperature, due to ascent, is strongest is known as the thermal tropical tropopause or cold trap. Air passing through the thermal tropical tropopause is dehydrated by the condensation of water vapour. Dehydration of air entering the stratosphere influences the distribution of water vapour in this atmospheric layer. Another consequence of the transport of chemicals into the stratosphere by the Brewer-Dobson circulation is

that some of these chemicals (*e.g.* CFCs) are involved in processes such as ozone destruction.

At middle latitudes transport across the tropopause is predominantly due to tropopause folding. Tropopause folding is a process in which the tropopause (defined in terms of potential vorticity) intrudes deeply into the troposphere (Andrews *et al.*, 1987). This results in high potential vorticity air from the stratosphere entering the troposphere and then being mixed with tropospheric air along the edges of the tropopause fold. Tropopause folds are responsible for transport of air from the stratosphere into the troposphere.

1.3.5 Dynamical Structure Of The Winter Stratosphere

In the winter stratosphere potential vorticity on isentropic surfaces is high at the pole and low in the tropics. The winter polar stratosphere is dominated by the polar vortex. Due to cooling over the winter pole (the winter pole is tilted away from the sun) there is a strong eastward flow around the pole in the stratosphere which is the polar vortex. This situation allows the propagation of planetary scale Rossby waves from the troposphere into the stratosphere (Charney & Drazin, 1961). Rossby waves are excited by flow over topography (*e.g.* Himalayas, Rocky Mountains) and by land-sea temperature contrasts. These waves propagate up from the troposphere and break in a region of the stratosphere known as the surf zone (McIntyre, 1982; McIntyre & Palmer, 1983, 1984). The surf zone is a large Rossby wave critical layer (see chapter 2 for more details on critical layers) and when Rossby wave breaking occurs it mixes air isentropically over large areas of the stratosphere.

Very large amplitude wave breaking on the edge of the polar vortex is known as a stratospheric sudden warming. In a stratospheric sudden warming the wave breaking, due to its large amplitude, typically leads to a breakdown of the po-

lar vortex. Stratospheric sudden warmings mix cold polar air equatorward and warmer midlatitude air poleward and therefore have a significant impact on the temperature at the pole and the distribution of chemicals, such as ozone, in the stratosphere.

The dynamical structure of the stratosphere is characterised by strong gradients of potential vorticity in the subtropics and at polar latitudes. These strong potential vorticity gradients are formed by mixing in the stratospheric surf zone which steepens the potential vorticity gradients in these two regions and weakens potential vorticity gradients in the surf zone resulting in a potential vorticity staircase profile (McIntyre, 1982). Strong gradients of potential vorticity are barriers to mixing and transport and therefore these potential vorticity gradients isolate air in the tropics and at the poles from the vigorous mixing of the extratropical surf zone.

Several studies have examined mixing and transport across the subtropical barrier, for example Plumb (1996), Neu & Plumb (1999), Ray *et al.* (2010). Mixing and transport into the tropics has significant implications for tracer concentrations within the stratosphere.

1.4 Quantifying Mixing and Transport

Mixing of a fluid is a result of advection (“stirring”), which stretches and folds material contours, and also of diffusion, which is an irreversible process. There are several diagnostics that can be used to quantify the mixing and transport properties of a given fluid flow. Mixing and transport can be measured directly by analysing the movement of particles in Lagrangian trajectories (see chapter 5).

Lagrangian measures such as Lyapunov exponents and contour lengths can

be used to quantify mixing. Lyapunov exponents characterise the average rate of separation of particles in a flow. If δx_0 denotes the separation of two particles at time $t = t_0$ their separation after some time t is given by

$$|\delta x(t)| = e^{\lambda t} |\delta x_0| \quad (1.12)$$

where λ is the Lyapunov exponent. Contour lengths are also a good measure of mixing. The length of a material contour is greater than its initial length when it has been stretched and folded due to stirring. As a result of this stirring there is more contour interface for diffusion to act upon which enhances the mixing.

Effective diffusivity (κ_{eff}) as described by Nakamura (1996) is a hybrid Eulerian-Lagrangian quantity and is a useful diagnostic for calculating the mixing properties of a given flow. Effective diffusivity is a measure of how much more a tracer particle, say, has been transported compared to how it would have moved due to molecular diffusion alone. Calculating the effective diffusivity comes from transforming the advection-diffusion equation (1.13) to tracer coordinates, using a mapping between tracer concentration and area, to give a diffusion only equation (see section 1.4.1). Another diagnostic linked to the effective diffusivity is the equivalent length (L_e). Equivalent length is related to the contour length in that it increases as contours are stretched and folded due to stirring.

Nakamura (1996), Haynes & Shuckburgh (2000a) and Haynes & Shuckburgh (2000b) have shown the usefulness of effective diffusivity as a diagnostic of mixing. In particular Shuckburgh & Haynes (2003) show that effective diffusivity can be used as a *quantitative* diagnostic of transport and mixing with their results illustrating how effective diffusivity accurately captures the location and character of barrier and mixing regions.

Effective diffusivity has been used to examine mixing in the upper troposphere and lower stratosphere (Scott *et al.*, 2003). It was found that the sub-

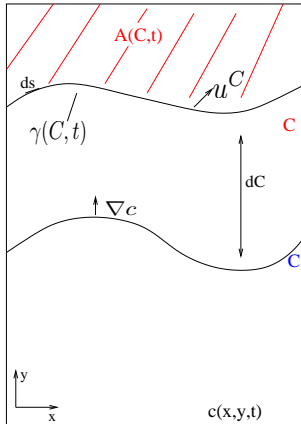


Figure 1.4: Diagram of the area coordinate. It shows 2 contours C of the tracer $c(x, y, t)$ with the area $A(C, t)$ being that enclosed above the contours.

tropical tropopause was a region of low effective diffusivity suggesting that it acts as a partial barrier to the transport of particles from the troposphere into the stratosphere. More recently effective diffusivity has also been used to investigate two-dimensional mixing and transport in idealised hurricane-like vortices (Hendricks & Schubert, 2009).

1.4.1 Calculation of Effective Diffusivity

In order to calculate the effective diffusivity (*i.e.* transforming the advection-diffusion equation (1.13) to a diffusion only equation) it is useful to begin by considering the evolution of a passive tracer in a given flow. The advection-diffusion equation for a passive tracer in an incompressible flow ($\nabla \cdot \mathbf{u} = 0$) is

$$\frac{\partial c}{\partial t} + \mathbf{u} \cdot \nabla c = \nabla \cdot (\kappa \nabla c) \quad (1.13)$$

where $c(x, y, t)$ is the concentration of the passive tracer and κ is the constant diffusivity.

This advection-diffusion equation (1.13) can be reduced to a diffusion only

equation by making a transformation from Cartesian coordinates (x, y) to tracer coordinates (C, s) (following Nakamura (1996) and Hendricks & Schubert (2009)). C represents a given value of the passive tracer $c(x, y, t)$, $\gamma(C, t)$ is defined as the contour enclosing all the tracer where $c(x, y, t) \geq C$ and s is the position on the contour $\gamma(C, t)$. Let the region enclosed by the contour $\gamma(C, t)$ be denoted by $A(C, t)$ so that

$$A(C, t) = \iint_{c \geq C} dx dy \quad (1.14)$$

Note that as the value of C increases, the area enclosed by C decreases (*i.e.* $A(C, t)$ is a monotonically decreasing function of C) with $A(C_{max}, t) = 0$.

Let \mathbf{u}^C be the velocity of the contour $\gamma(C, t)$ and define it such that

$$\frac{\partial c}{\partial t} + \mathbf{u}^C \cdot \nabla c = 0 \quad (1.15)$$

This is not a unique definition. Note that the contour $\gamma(C, t)$ is not a material contour since diffusion allows fluid to move across the contour. However \mathbf{u}^C is the velocity of the contour, not the fluid velocity, and therefore $\gamma(C, t)$ is a material contour w.r.t. \mathbf{u}^C .

As the contour $\gamma(C, t)$ moves in time, we want an expression for the rate of change of the area, $A(C, t)$, enclosed by this contour. The rate of change of area is the circumference of the contour $\gamma(C, t)$ multiplied by the normal component of the velocity of the contour, \mathbf{u}^C .

$$\frac{\partial A(C, t)}{\partial t} = \frac{\partial}{\partial t} \iint_{c \geq C} dx dy = - \int_{\gamma(C, t)} \mathbf{u}^C \cdot \frac{\nabla c}{|\nabla c|} ds \quad (1.16)$$

Note that the normal is the *outward* normal and ∇c is *inward*. Therefore the normal is $-\frac{\nabla c}{|\nabla c|}$.

Now substituting (1.15) into (1.13) we can write \mathbf{u}^C in terms of the fluid velocity \mathbf{u} as follows

$$\mathbf{u}^C \cdot \nabla c = \mathbf{u} \cdot \nabla c - \nabla \cdot (\kappa \nabla c) \quad (1.17)$$

Substituting this into the last equality of (1.16) produces

$$\frac{\partial A(C, t)}{\partial t} = \int_{\gamma(C, t)} \nabla \cdot (\kappa \nabla c) \frac{ds}{|\nabla c|} - \int_{\gamma(C, t)} \mathbf{u} \cdot \nabla c \frac{ds}{|\nabla c|} \quad (1.18)$$

The second term on the right hand side of (1.18) is an advection term and can be written as

$$- \int_{\gamma(C, t)} \nabla \cdot (c\mathbf{u}) \frac{ds}{|\nabla c|} \quad (1.19)$$

using $\mathbf{u} \cdot \nabla c = \nabla \cdot (c\mathbf{u})$ for an incompressible flow.

In order to take the factor c outside the integrand and therefore have $\nabla \cdot \mathbf{u} = 0$, thus making the whole term zero, we need to transform (1.19) into a surface integral and then back to a line integral using the divergence theorem ($\iint_A \nabla \cdot \mathbf{F} dA = \int_\gamma \mathbf{F} \cdot d\mathbf{s}$).

The area element in Cartesian coordinates is $dA = dx dy$. In tracer coordinates $dA = \frac{ds dC'}{|\nabla c|}$ where $\frac{1}{|\nabla c|}$ is the Jacobian for the transformation from Cartesian coordinates to tracer coordinates. Therefore

$$\frac{\partial}{\partial C} \iint_{c \geq C} (\dots) dx dy = \frac{\partial}{\partial C} \iint_{c \geq C} (\dots) \frac{ds dC'}{|\nabla c|} = - \int_{\gamma(C, t)} (\dots) \frac{ds}{|\nabla c|} \quad (1.20)$$

The last equality comes from the use of first principles to write the derivative in the limit $C \rightarrow 0$.

Now reading (1.20) in reverse and substituting into (1.19) yields

$$\frac{\partial}{\partial C} \iint_{c \geq C} \nabla \cdot (c\mathbf{u}) \frac{dsdC'}{|\nabla c|} \quad (1.21)$$

Using the divergence theorem, noting again that the normal \mathbf{n} is the outward normal *i.e.* $-\frac{\nabla c}{|\nabla c|}$, (1.21) becomes

$$-\frac{\partial}{\partial C} \int_{\gamma(C,t)} c\mathbf{u} \cdot \frac{\nabla c}{|\nabla c|} ds \quad (1.22)$$

The factor c can now be taken outside the integrand leaving

$$\int_{\gamma(C,t)} \mathbf{u} \cdot \mathbf{n} ds = \iint_A \nabla \cdot \mathbf{u} dA = 0 \quad (1.23)$$

Hence the advection term on the right hand side of (1.18) is zero. This means that the contour $\gamma(C, t)$ can be advected but the area enclosed by $\gamma(C, t)$ won't change. Therefore only the first term on the right hand side of (1.18) can change the area enclosed by $\gamma(C, t)$ and this is by diffusion across the contour. From (1.18) we now have

$$\frac{\partial A(c, t)}{\partial t} = \int_{\gamma(C,t)} \nabla \cdot (\kappa \nabla c) \frac{ds}{|\nabla c|} \quad (1.24)$$

To put (1.24) into a more useful form we follow a similar analysis to that of the advection term on the right hand side of (1.18). Firstly, reading (1.20) backwards and substituting into (1.24) we obtain

$$\frac{\partial A(C, t)}{\partial t} = -\frac{\partial}{\partial C} \iint_{c \geq C} \nabla \cdot (\kappa \nabla c) \frac{dsdC'}{|\nabla c|} \quad (1.25)$$

Then using the divergence theorem, this becomes

$$\frac{\partial A(C, t)}{\partial t} = \frac{\partial}{\partial C} \int_{\gamma(C,t)} \kappa |\nabla c| ds \quad (1.26)$$

To examine mixing and transport in a fluid we want to know how the value of tracer enclosing a given area, A , changes in time. The area $A(C, t)$ is a monotonic (decreasing) function of tracer value C . This means that the inverse $C(A, t)$ is unique. Using the chain rule we obtain the following relation

$$\frac{\partial A(C, t)}{\partial t} \frac{\partial C(A, t)}{\partial A(C, t)} = -\frac{\partial C(A, t)}{\partial t} \quad (1.27)$$

Substituting (1.27) into (1.26) produces

$$\frac{\partial C(A, t)}{\partial t} = -\frac{\partial C(A, t)}{\partial A} \frac{\partial}{\partial C} \int_{\gamma(C, t)} \kappa |\nabla c| ds = -\frac{\partial}{\partial A} \int_{\gamma(C, t)} \kappa |\nabla c| ds \quad (1.28)$$

From (1.20), the integral on the right hand side of (1.28) can be written as follows

$$\int_{\gamma(C, t)} \kappa |\nabla c| ds = \int_{\gamma(C, t)} \kappa |\nabla c|^2 \frac{ds}{|\nabla c|} = -\frac{\partial}{\partial C} \iint_{c \geq C} \kappa |\nabla c|^2 dx dy \quad (1.29)$$

Substituting this into (1.28), we obtain

$$\frac{\partial C(A, t)}{\partial t} = \frac{\partial}{\partial A} \left(\frac{\partial}{\partial C} \iint_{c \geq C} \kappa |\nabla c|^2 dx dy \right) \quad (1.30)$$

This can be rewritten to the form

$$\frac{\partial C(A, t)}{\partial t} = \frac{\partial}{\partial A} \left(K_{\text{eff}}(A, t) \frac{\partial C(A, t)}{\partial A} \right) \quad (1.31)$$

where

$$K_{\text{eff}}(A, t) = \left(\frac{\partial C(A, t)}{\partial A} \right)^{-2} \frac{\partial}{\partial A} \iint_{c \geq C} \kappa |\nabla c|^2 dx dy \quad (1.32)$$

Therefore, using the area coordinate, the advection-diffusion equation (1.13) has become a diffusion-only equation (1.31). The effective diffusivity defined by (1.32) is a useful diagnostic of mixing and transport in a fluid. It has been shown by Shuckburgh & Haynes (2003) to capture the precise location and character of mixing regions and barriers to transport within a flow. Note, however, that the effective diffusivity does not have the normal dimensions of diffusion (m^2s^{-1}) but rather the dimensions m^4s^{-1} . This is due to the use of the area coordinate. In order for the effective diffusivity to have more convenient dimensions, *i.e.* those of normal diffusion, (1.32) can be rewritten replacing the area coordinate A with either an equivalent radius coordinate, r_e , for cylindrical geometry or an equivalent latitude coordinate, y_e , for channel geometry.

Firstly consider an equivalent radius coordinate, r_e , for a cylindrical domain, where

$$\pi r_e^2 = A \quad (1.33)$$

From (1.33) it can be seen that

$$\frac{1}{2\pi r_e} \frac{\partial}{\partial r_e} = \frac{\partial}{\partial A} \quad (1.34)$$

Substituting this into (1.31) yields

$$\frac{\partial C(r_e, t)}{\partial t} = \frac{1}{r_e} \frac{\partial}{\partial r_e} \left(r_e \kappa_{\text{eff}}(r_e, t) \frac{\partial C(r_e, t)}{\partial r_e} \right) \quad (1.35)$$

with

$$\kappa_{\text{eff}}(r_e, t) = \frac{K_{\text{eff}}(A, t)}{4\pi A} \quad (1.36)$$

Now, for mixing in a channel, we consider an equivalent latitude coordinate, y_e , where

$$L_x y_e = A \quad (1.37)$$

Let the width of the channel be $L_x = 2\pi$. Then

$$2\pi y_e = A \quad (1.38)$$

From this, it can be seen that

$$\frac{1}{2\pi} \frac{\partial}{\partial y_e} = \frac{\partial}{\partial A} \quad (1.39)$$

Substituting this into (1.31) produces

$$\frac{\partial C(y_e, t)}{\partial t} = \frac{\partial}{\partial y_e} \left(y_e \kappa_{\text{eff}}(y_e, t) \frac{\partial C(y_e, t)}{\partial y_e} \right) \quad (1.40)$$

with

$$\kappa_{\text{eff}}(y_e, t) = \frac{K_{\text{eff}}(A, t)}{2\pi A} \quad (1.41)$$

Another equivalent diagnostic is equivalent length, defined as

$$L_e(A, t)^2 = \frac{1}{\kappa} K_{\text{eff}}(A, t) \quad (1.42)$$

The equivalent length is related to the length of the contour $\gamma(C, t)$. $L_e \geq L$ always, where L is the length of the contour $\gamma(C, t)$ enclosing a given tracer value. Note that equality is achieved in the special case where $\nabla c = 0$ along the contour $\gamma(C, t)$.

1.5 Outline of Thesis

In this thesis we investigate atmospheric transport and critical layer mixing in the troposphere and stratosphere in a range of models, from very idealised models through to a more realistic model of the atmosphere.

In chapter 2 we model critical layer mixing in a two dimensional channel and investigate the effect of the background shear flow on the evolution of the flow inside the critical layer, with particular attention to the occurrence of barotropic instability. We also consider how the mixing efficiency depends on the shear across the critical layer and we compare two different measures of mixing (effective diffusivity and contour lengths). Consideration is also given to the effect of finite Rossby deformation length on the critical layer evolution.

In chapter 3 we investigate how the location of the stratospheric polar vortex affects the location of the critical layer on the subtropical jet and how this then affects the dynamics in the troposphere. In particular we examine in detail how a significant redistribution of the stratospheric potential vorticity, as is observed during major stratospheric sudden warmings, can effect the evolution in the troposphere and at the Earth's surface.

Chapter 4 describes a trajectory model, developed in conjunction with the UK Met Office, which will be used for the study of atmospheric transport and mixing in more realistic situations. A brief outline of the model is given along with the results of some sensitivity experiments.

In chapter 5 the trajectory model described in chapter 4 is used to investigate the effect of the quasi-biennial oscillation (hereafter QBO) on mixing and transport in the stratosphere. We form a hypothesis, of how the QBO may affect mixing and transport, based on the potential vorticity structure. Here we examine mixing and transport directly by analysing trajectories of Lagrangian particles in order to test the hypothesis and determine if an effect exists. In

chapter 6 our findings throughout this thesis are summarised and discussed.

Finally chapter 7 contains the documentation for the trajectory model described and used in chapters 4 and 5. It details where to find the code and how to view the model output along with some information about specific parameters.

Chapter 2

Mixing in a Rossby Wave Critical Layer

2.1 Introduction

Critical layers can be thought of as a model of Rossby wave breaking in the stratosphere. The continued interest in the study of critical layers is invaluable to aid the understanding of large scale atmospheric flows.

The equation for linear Rossby wave propagation on a non-uniform basic state $U(y)$ has a singularity at points y for which the Rossby wave phase speed c equals the basic state: $U - c = 0$. In the vicinity of such points linear theory breaks down and nonlinear terms in the governing equation must be retained. The region over which where nonlinearity is important is referred to as a Rossby wave critical layer. Within the critical layer the evolution is characterised by the wrapping up of material contours of potential vorticity in the well known Kelvin cat's eye pattern. The cat's eye evolution mixes potential vorticity inside the critical layer. Critical layers are regions of great importance due to the strong mixing and transport that occurs within them. Another important issue is whether critical

layers act as wave absorbers or reflectors (depending on the details of the mixing).

The study of critical layers goes back to the work of Benney & Bergeron (1969), Davis (1969), Dickinson (1970) and other authors. A significant advance in the theory of critical layers was made simultaneously by Stewartson (1978) and Warn & Warn (1978) (hereafter SWW). They investigated analytically the structure of the critical layer formed by forcing Rossby waves in a uniform shear flow. SWW applied the method of matched asymptotic expansions to the problem of Rossby wave critical layers and treated the critical layer as the inner region. An exact analytical solution was found for a particular choice of boundary conditions. The SWW solution for this special case allowed accurate predictions to be made about the time evolution of the critical layer. One such prediction of the SWW solution is that the critical layer oscillates between an absorbing state (absorbs energy from incident Rossby waves) and an over-reflecting state (reflects the incoming wave and releases some of the wave activity previously absorbed). In the long-time limit the critical layer tends to a state of perfect reflection. The absorbing and reflecting properties of critical layers was examined further by Killworth & McIntyre (1985).

The work of SWW was extended by Haynes (1989). Haynes (1989) used a generalisation of the SWW solution for the exact critical layer dynamics to explore the evolution of the critical layer over a range of the single non-dimensional parameter which governed the system. Killworth & McIntyre (1985) have shown that the SWW critical layer flow is unstable. In particular Haynes (1989) investigated the development of the instability within the critical layer and its effect on the critical layer absorptivity. Haynes (1989) showed that the simple wrap-up within the critical layer may break down due to barotropic instability in regions where the potential vorticity is locally non-monotonic. This barotropic instability makes a substantial difference to the potential vorticity distribution in the critical layer. Haynes (1989) also found that the instability increased the time

integrated absorptivity of the critical layer to three or four times that predicted by the SWW solution.

The objective of this chapter is to investigate further the evolution of barotropic instability within the critical layer. We adopt a numerical approach at a higher resolution than Haynes (1989) and examine mixing within the critical layer over a wider parameter range. We also consider how the mixing efficiency (defined here as the rate at which potential vorticity across the critical layer is homogenised) depends on the shear across the critical layer and use this dynamically consistent flow to compare different measures of mixing (effective diffusivity and contour stretching rates). In an extension to previous studies we consider a systematic treatment of the effects of finite Rossby deformation length on the critical layer evolution (which was far as we are aware has not been done before).

In section 2.2 a description of the model is given, including details of the direct forcing in the critical layer and the scaling used in the problem. The results for an infinite Rossby deformation length are presented in section 2.3 along with a discussion on the effect of the shear across the critical layer on the mixing efficiency within the critical layer. The finite Rossby deformation length case is then considered in section 2.4. A summary of the conclusions drawn follows in section 2.5.

2.2 Model Description

The numerical model used is a high resolution contour advection semi-Lagrangian (CASL) model, originally developed by Dritschel & Ambaum (1997), which solves the equivalent barotropic vorticity equation on the midlatitude β -plane in a periodic channel. The equations take the form

$$\frac{Dq}{Dt} = \frac{\partial q}{\partial t} + \mathbf{u} \cdot \nabla q = 0 \quad (2.1)$$

$$q = \beta y + (\Delta - L_D^{-2})\psi + q_{\text{topo}} \quad (2.2)$$

$$\mathbf{u} = (-\psi_y, \psi_x) \quad (2.3)$$

along with the boundary condition at the walls

$$v = \psi_x = 0 \quad \text{at } y = \pm L_y \quad (2.4)$$

Here q is the potential vorticity, ψ is the streamfunction, $\mathbf{u} = (u, v)$ is the horizontal velocity, β is the linear coefficient of the Coriolis frequency and L_D is the Rossby deformation length.

Critical layers can be forced in many ways (upward propagation, lateral forcing). Both SWW (1978) and Haynes (1989) consider the case where the critical layer is forced laterally. In this investigation we do not approach the problem in the same way as SWW (1978) and Haynes (1989), instead we force the streamfunction in the critical layer directly. Ideally to examine realistic flow one needs to force waves with an exact wave at the top boundary and have a semi-infinite channel, *i.e.* $y \rightarrow -\infty$. In this model we have two solid boundaries at $y = \pm L_y$. Initially we tried forcing waves by topography at the upper boundary ($y = L_y$) however we found that the wave propagation from the boundary depended on the shear of the flow (propagation when shear sufficiently small). Also the potential vorticity anomaly of the topography was non local and so the streamfunction associated with the topography extended further than the intended forcing region and created a weak instantaneous response in the critical layer region (for large shear). Hence the mechanisms for the critical layer forcing were not the same between the large and the small shear flows. Therefore we chose to instead focus on the critical layer itself and force directly in that region. This would then result in a much cleaner problem (due to no wave propagation).

We use the SWW (1978) solution as a model for the critical layer. We decompose ψ into a basic state and a perturbation

$$\psi = \Psi(y) + \varphi(x, y, t) \quad (2.5)$$

where $\Psi(y) = -\frac{1}{2}\Lambda y^2$ is a linear shear flow $U(y) = \Lambda y$. The perturbation streamfunction consists of a topographic forcing term ψ_{topo} such that $\Psi(y) + \psi_{\text{topo}} = -\frac{1}{2}\Lambda y^2 + A \cos(x)$ is the SWW (1978) solution (A is the forcing amplitude). Note that $\varphi(x, y, t)$ can be thought of as $\psi_{\text{topo}} + \psi'(x, y, t)$ where ψ_{topo} is the streamfunction associated with the topographic forcing and ψ' is a perturbation. We solve (2.1) numerically within the critical layer (critical layer at $y = 0$). The wave solution in the critical layer is represented by a fixed topographic forcing term q_{topo} that coincides with the perturbation streamfunction of the SWW solution (ψ_{topo} here). To satisfy the boundary conditions (2.4) and to ensure the streamlines are independent of the shear, the topographic streamfunction, becomes

$$\psi_{\text{topo}} = \epsilon\Lambda \left(1 - \frac{\cosh y}{\cosh L_y} \right) \cos x \quad (2.6)$$

where $\epsilon \ll 1$ and $y = \pm L_y$ denotes the walls of the channel.

In the model we use dimensional variables and therefore (2.1) is different to (2.5) in Haynes (1989). To ensure that the critical layer in non-dimensional variables is of a fixed width for all shears Λ we rescale y . As the shear decreases the critical layer width decreases (forcing amplitude decreases with shear) and therefore y must decrease so that the critical layer width remains the same fraction of the channel for all shears considered (note that this is $\frac{2}{5}$ of the channel width). This is achieved by defining an aspect ratio $\frac{\beta}{2k\Lambda}$ such that the ratio of the along- to cross-channel lengths is the aspect ratio, *i.e.* $\frac{L_x}{L_y} = \text{aspect}$, where Λ denotes the shear and k denotes the x-wavenumber.

The system is described by the non-dimensional parameter $\mu = \frac{k\Lambda}{\beta}$, following

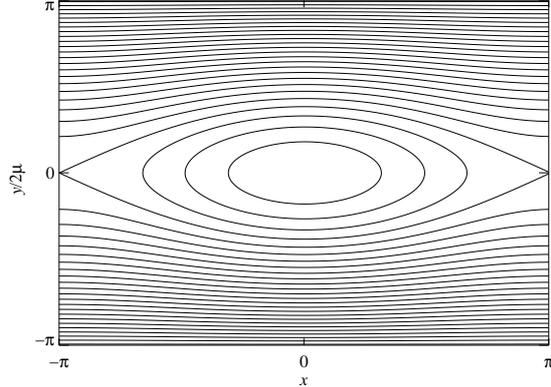


Figure 2.1: The critical layer streamfunction due to topography: $\Psi(y) + \psi_{\text{topo}}$.

Haynes (1989), which is the ratio of the cross- to along- channel length scales. To investigate the effect of the shear on the critical layer evolution we set $\beta = k = 1$ so that $\mu = \Lambda$. We non-dimensionalise (following Haynes (1989)):

$$y^* = \frac{\Lambda}{\beta}y, \quad x^* = \frac{x}{k}, \quad t^* = \frac{\beta}{k\Lambda^2}t \quad (2.7)$$

Note the starred quantities are dimensional. Using the non-dimensional parameter μ the topographic streamfunction can be generalised to

$$\psi_{\text{topo}} = \epsilon\mu \left(1 - \frac{\cosh y}{\cosh(2\pi\mu)} \right) \cos x \quad (2.8)$$

The channel walls are at $y = \pm L_y = \pm 2\pi\mu$. The critical layer streamlines due to the background shear and topography are displayed in Figure 2.1.

The model resolution is 257 points in y (cross channel) and 256 points in x (along channel). The topographic forcing is ramped up over the first tenth of the calculation to reduce transients and therefore give cleaner dynamics.

2.3 Critical Layer Evolution

In this section we investigate the effect of the shear on the evolution of the critical layer with an infinite deformation length (*i.e.* $L_D^{-1} = 0$). We examine critical layers with a variety of background shear flows, $\frac{1}{16} \leq \Lambda \leq 1$. There are two main stages in the evolution of a critical layer. The first is the wrap up of potential vorticity into the well known “cat’s eye” pattern. This wrap up of potential vorticity is displayed in Figure 2.2 for the case where the shear is one ($\Lambda = 1$). The wrapping up of potential vorticity into cat’s eyes moves low potential vorticity into an area of high potential vorticity creating a non-monotonic potential vorticity profile locally in a region. In this case ($\Lambda = 1$) these regions of non-monotonic potential vorticity are stabilised by the background shear.

The second stage of the critical layer evolution is the growth of barotropic instability. The local non-monotonic potential vorticity profile is unstable by the same mechanism in Dritschel *et al.* (1991) which is barotropic instability. Note that barotropic instability only occurs in certain cases. Figure 2.3 shows the critical layer evolution for the cases where $\Lambda = \frac{1}{2}, \frac{1}{4}, \frac{1}{8}$ and $\frac{1}{16}$. The aspect ratio depends on the shear (Λ) and therefore the potential vorticity contour plots have been stretched in the y direction by an amount proportional to $\frac{1}{\Lambda}$. From this figure we can see that barotropic instability appears in the critical layer evolution around $\Lambda = \frac{1}{4}$. A feature of the instability is the appearance of secondary cat’s eyes of reduced wavelength in the along-channel direction (x direction) consistent with the work of Haynes (1989). As the shear of the background flow decreases the wavelength of the secondary cat’s eyes decreases. The high resolution in x in the model is justified due to this shortening of along-channel wavelengths at low shears. For shears greater than $\Lambda = \frac{1}{4}$ there is no barotropic instability. This is because the filament is stabilised by the background shear (shear suppresses

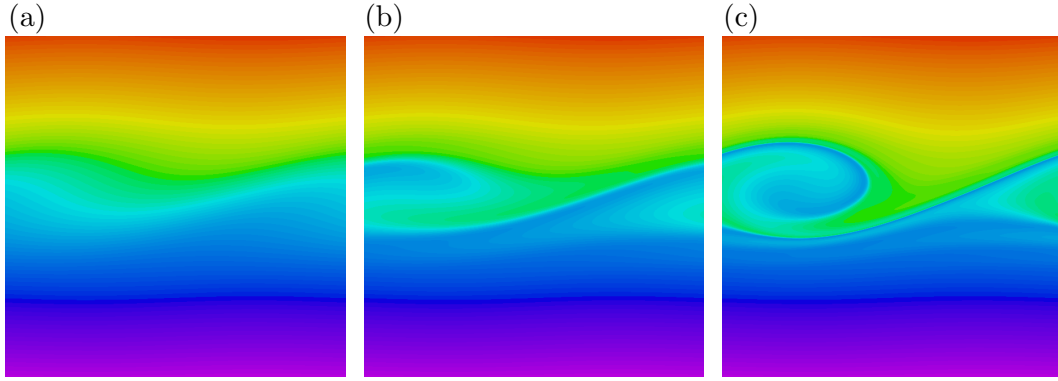


Figure 2.2: Snapshots of potential vorticity for the case $\Lambda = 1$ at (a) $t = 1$, (b) $t = 2$ and (c) $t = 3$. Note: only the middle half of the domain is shown.

the instability). This condition for stability is similar to that found by Dritschel *et al.* (1991) who examined the stability of filaments in strain. For $\Lambda \ll 1$ the local background flow is approximately uniform and so does not act to stabilise the filament and hence the instability grows quickly on this background flow. This is demonstrated by Figure 2.3 (c) and (d). Also as the shear decreases, the instability occurs at earlier times. For all the cases studied we found that the critical layer becomes barotropically unstable when $\Lambda \leq 0.3$.

Haynes (1989) found that there were certain values of μ (here $\mu = \Lambda$ because $\beta = k = 1$) where resonance occurred ($\mu = \frac{1}{3}, \frac{1}{4}, \frac{1}{5}$). In our model, a resonance appears to occur for $0.4 < \Lambda < 0.7$. The resonance, *i.e.* the linear growth of the critical layer width in time can be seen in Figure 2.4 for the case $\Lambda = \frac{1}{2}$. The occurrence of resonance explains why the evolution of the critical layer differs between $\Lambda = 1$ and $\Lambda = \frac{1}{2}$.

Critical layers mix potential vorticity. We consider here how the mixing efficiency of the critical layer depends on the shear across it. We examine the zonal mean potential vorticity, $\bar{q}(y)$ at several times (minus the constant arising from the background shear, for ease of comparison). The zonal mean potential vorticity at $t = 10$ (non-dimensional time) for shears $\Lambda = \frac{1}{2}, \frac{1}{4}, \frac{1}{8}$ and $\frac{1}{16}$ is shown

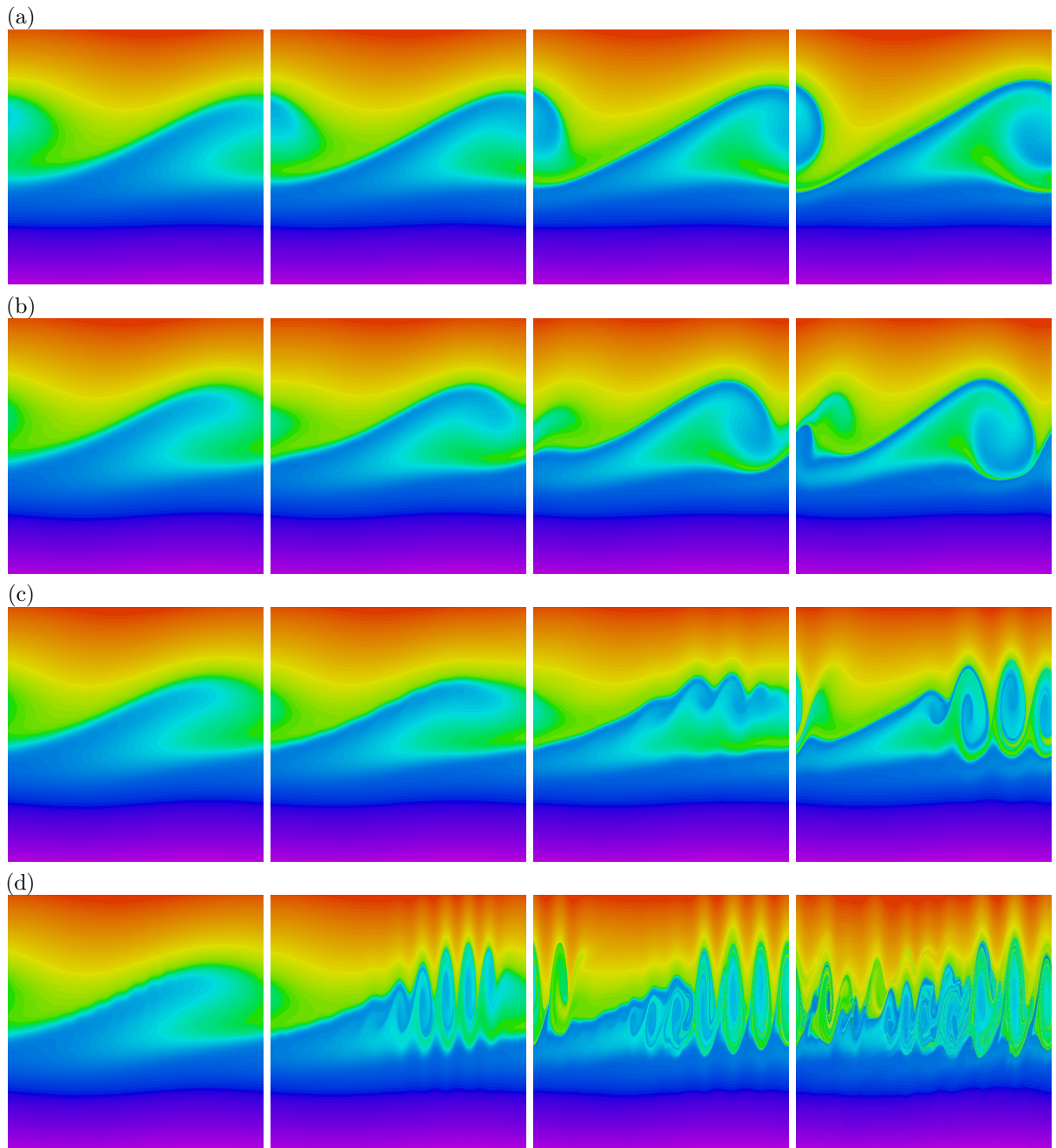


Figure 2.3: Snapshots of potential vorticity at $t = 1.2, 1.4, 1.6, 1.8$ for the case (a) $\Lambda = \frac{1}{2}$, (b) $\Lambda = \frac{1}{4}$, (c) $\Lambda = \frac{1}{8}$ and (d) $\Lambda = \frac{1}{16}$. Note: only the middle half of the domain is shown.

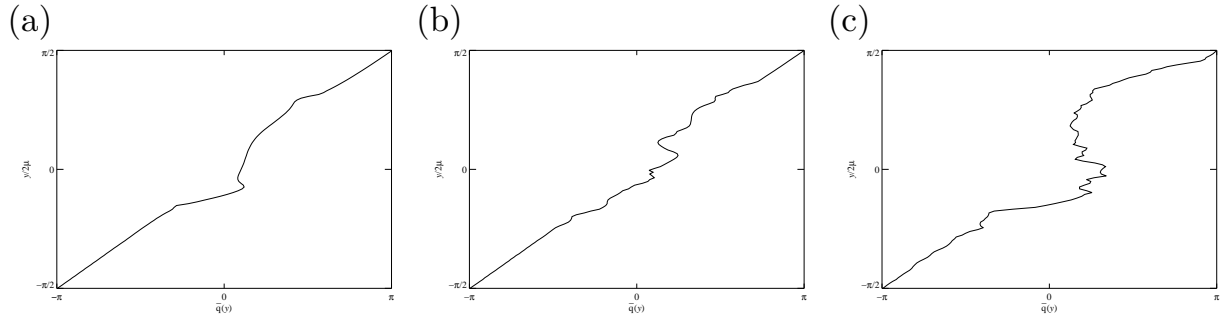


Figure 2.4: Zonal mean potential vorticity ($\bar{q}(y)$) at (a) $t = 2$, (b) $t = 4$ and (c) $t = 8$ for the case $\Lambda = \frac{1}{2}$. Note: only the middle half of the domain is shown.

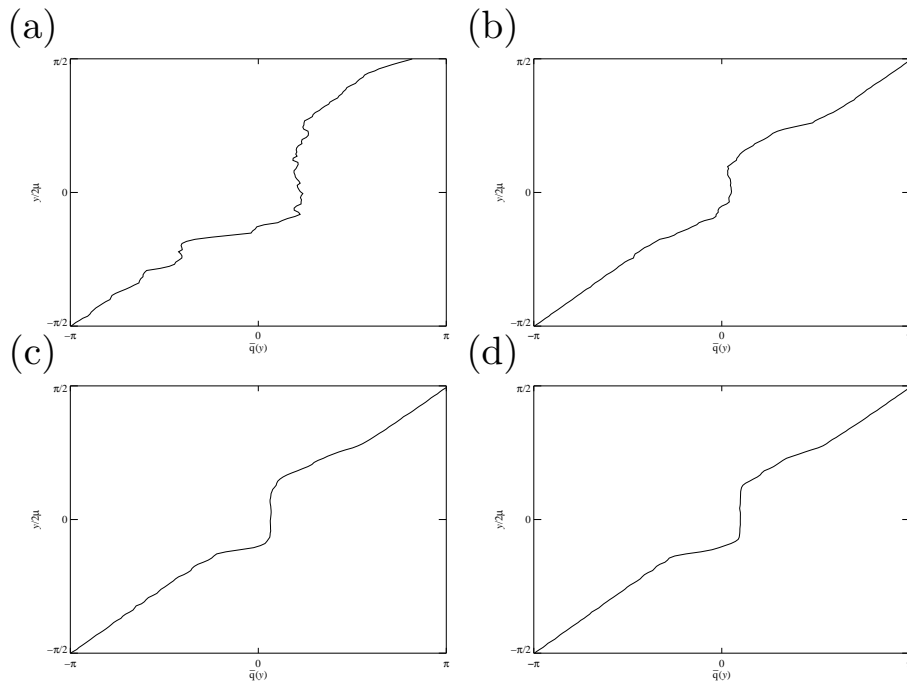


Figure 2.5: Zonal mean potential vorticity ($\bar{q}(y)$) at $t = 10$ for the case (a) $\Lambda = \frac{1}{2}$, (b) $\Lambda = \frac{1}{4}$, (c) $\Lambda = \frac{1}{8}$ and (d) $\Lambda = \frac{1}{16}$. Note: only the middle half of the domain is shown.

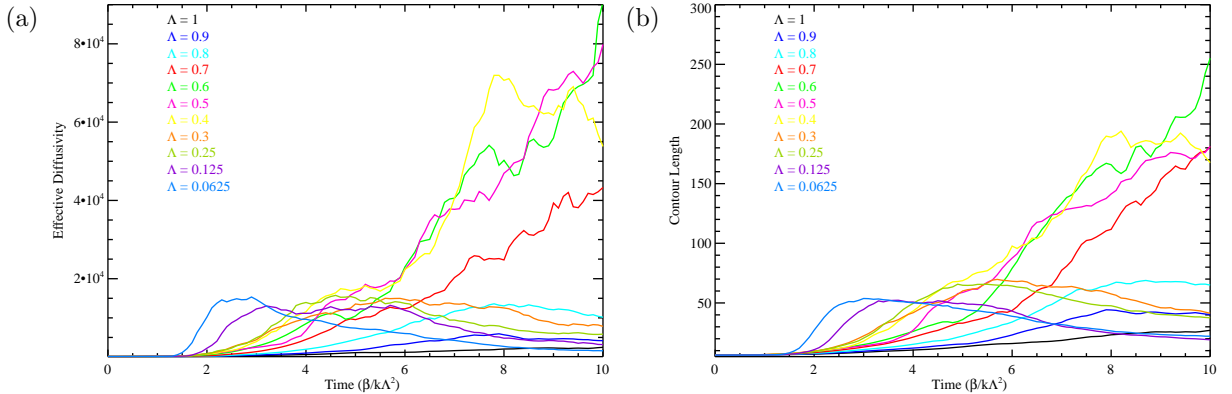


Figure 2.6: Time evolution of channel integrated effective diffusivity (a) and average contour length (b) for $\frac{1}{16} \leq \Lambda \leq 1$.

in Figure 2.5. The potential vorticity is almost perfectly mixed in the critical layer region (around $y = 0$) in each case resembling a potential vorticity staircase profile (McIntyre, 1982). The stratospheric surf zone is a Rossby wave critical layer and therefore the mixing region indicated by the zonal mean potential vorticity plots in Figure 2.5 can be thought of as the stratospheric surf zone. A comparison of Figures 2.5 (a) and (b) with Figures 2.5 (c) and (d) indicates that the potential vorticity inside the critical layer is better mixed when barotropic instability occurs than when there is only potential vorticity wrap up (indicated by the smoother potential vorticity staircase profile). Potential vorticity staircases is an area of continued interest motivated by the desire to understand and explain the banded structures observed in our atmosphere and the atmosphere of Jupiter. Recent work in this area had focussed on the link between potential vorticity mixing and jet sharpening and also on the effects of angular momentum conservation (Dritschel & McIntyre, 2008; Dunkerton & Scott, 2008).

The potential vorticity staircase profiles shown in Figure 2.5 do not contain information on the timescales of the mixing. Therefore to demonstrate the timescales of potential vorticity wrap up and barotropic instability we examine the time evolution of effective diffusivity (integrated across the channel) and con-

tour length (averaged across the channel). Figure 2.6 (a) shows the time evolution of effective diffusivity integrated across the channel. For the shear cases where barotropic instability occurs ($\Lambda \leq 0.3$) the effective diffusivity increases exponentially from the onset of the instability and then decreases as the potential vorticity homogenises in the critical layer region. On the other hand the effective diffusivity for the shear cases where there is no barotropic instability increases linearly in time (linear growth due to potential vorticity wrap up). It is interesting to note here that the high values of effective diffusivity for $0.4 < \Lambda < 0.7$ are due to the occurrence of resonance at these shears. This figure demonstrates that the timescale of barotropic instability (exponential) is faster than that of potential vorticity wrap up (linear). Hence there is an increase in the mixing efficiency of the critical layer due to barotropic instability. A comparison of Figure 2.6 (a) and (b) demonstrates that the time evolution of effective diffusivity and contour lengths are very similar and therefore they provide consistent measures of mixing.

We have found that the shear across the critical layer affects the evolution of the critical layer itself. Barotropic instability occurs for $\Lambda \leq 0.3$ and the mixing efficiency of the critical layer is increased due to this instability. Another interesting result is that although barotropic instability enhances mixing in the critical layer at early times (for small shear), this enhancement is in fact much smaller than the enhancement of mixing due to the resonant growth of the critical layer around $\Lambda = \frac{1}{2}$.

2.4 Evolution at Finite Deformation Length

2.4.1 The Basic State

In an extension to previous work we investigate the effects of finite deformation length on barotropic instability in a critical layer. Initially we considered the same

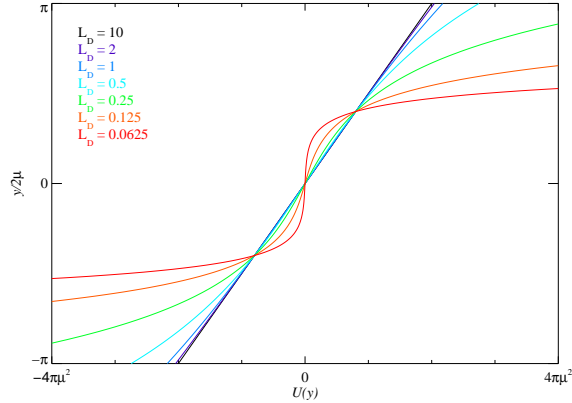


Figure 2.7: $U(y)$ for a given shear and $\frac{1}{16} \leq L_D \leq 10$.

background linear shear flow, $U(y) = \Lambda y$, from the infinite deformation length experiments. However the potential vorticity associated with the shear flow for finite L_D is

$$q = \beta y + \Lambda \left(\frac{1}{2} L_D^{-2} y^2 - 1 \right) \quad (2.9)$$

which is a quadratic in y . As $L_D \rightarrow 0$ the quadratic in (2.9) is dominated by the L_D term and becomes non-monotonic, *i.e.* unstable. Therefore a uniform shear flow has non-monotonic potential vorticity and this is undesirable because the evolution of the critical layer will be obscured by the possible instability of the background flow itself.

As a possible alternative, we consider the shear arising from a uniform potential vorticity basic state $q = \nabla^2 \Psi - L_D^{-2} \Psi = 0$. This along with the condition of no net momentum in any direction:

$$\int_{-2\pi\Lambda}^{2\pi\Lambda} \bar{u} dy = 0 \quad (2.10)$$

gives rise to a family of curves of the form

$$U(y) = \frac{A}{L_D} \sinh\left(\frac{y}{L_D}\right) \quad (2.11)$$

where A is a constant. Subsequently we examined two different conditions to find the constant A . The first condition was to define the shear at the center of the channel ($y = 0$) to be the same as the shear profiles investigated in the infinite deformation length experiments. This resulted in $A = \Lambda L_D^2$ where $u_y|_{y=0} = \Lambda$. The other condition considered was that the velocity difference across the channel was the same as in the $L_D^{-1} = 0$ cases. This gave

$$A = \frac{\Lambda 2\pi\Lambda L_D}{\sinh\left(\frac{2\pi\Lambda}{L_D}\right)} \quad (2.12)$$

where $y = \pm 2\pi\Lambda$ represents the channel walls. However neither of these conditions were suitable for our investigation. In the case of the first condition the velocities at the channel walls were too large at small L_D for the numerical calculation due to the hyperbolic sine term in (2.11). For the second condition the width of the critical layer equalled the width of the channel at small L_D due to the small velocities across the channel. This then caused uncertainties over the effects of the boundaries on the evolution.

Ultimately we decided that the average shear over the width of the critical layer should be comparable to the shear over the critical layer in the infinite Rossby deformation length experiments. We defined a top hat weighting

$$g(y) = \begin{cases} \frac{1}{2y_c} & \text{if } |y| < y_c \\ 0 & \text{otherwise.} \end{cases} \quad (2.13)$$

where $y_c = \frac{2}{5}(2\pi\Lambda)$ denotes the edge of the critical layer (critical layer is $\frac{2}{5}$ of the channel width), such that the average shear over the critical layer is equal to Λ as follows

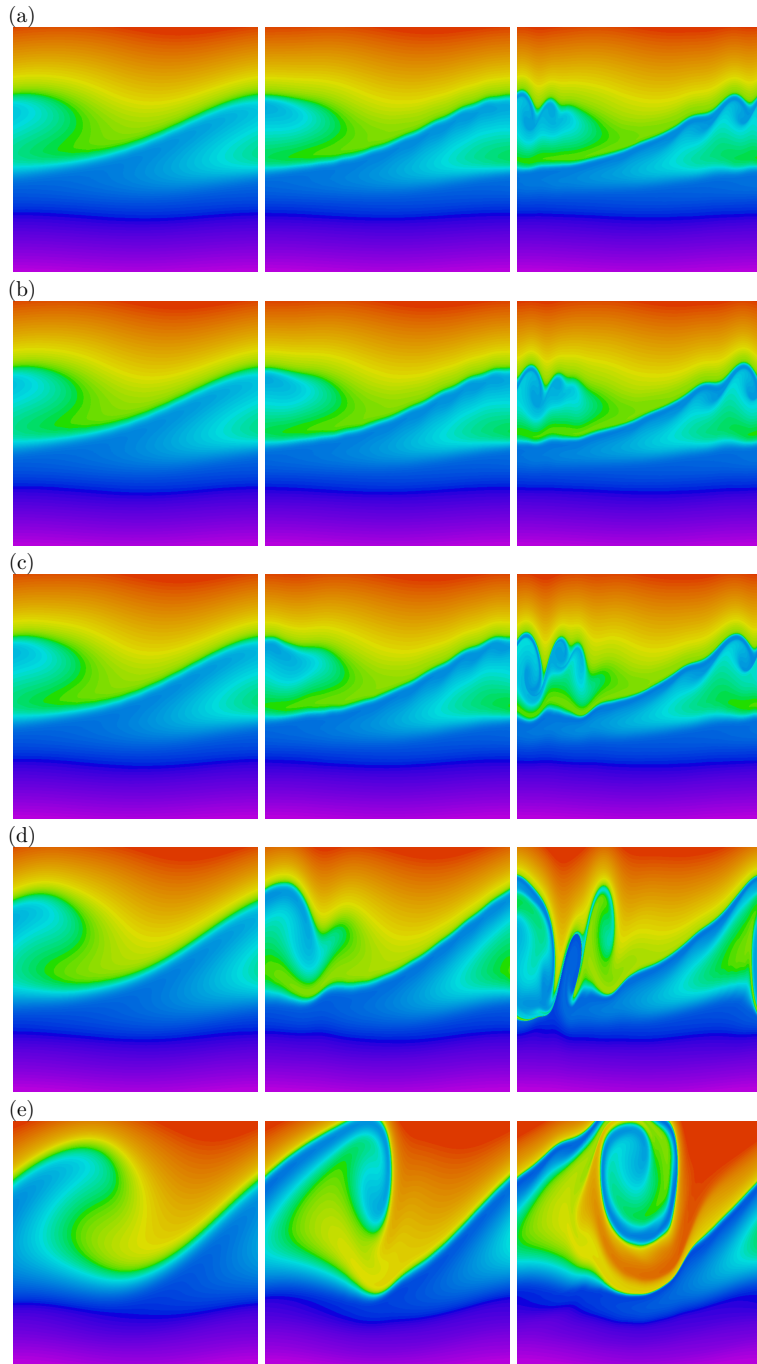


Figure 2.8: Snapshots of potential vorticity for the case $\Lambda = \frac{1}{8}$ at $t = 1.2, 1.4, 1.6$ for (a) $L_D = 10$, (b) $L_D = 2$ and (c) $L_D = 1$, at $t = 1, 1.2, 1.4$ for (d) $L_D = \frac{1}{2}$ and at $t = 0.8, 1, 1.2$ for (e) $L_D = \frac{1}{4}$. Note: only the middle half of the domain is shown.

$$\int_{-l}^l g(y)u_y dy = \Lambda \quad (2.14)$$

$$\int_{-y_c}^{y_c} u_y \frac{1}{2y_c} dy = \Lambda \quad (2.15)$$

$$\frac{1}{2y_c} (u(y_c) - u(-y_c)) = \Lambda \quad (2.16)$$

The constant Λ in (2.11) is then defined from (2.14) to be

$$A = \frac{2y_c L_D \Lambda}{[\sinh(\frac{y_c}{L_D}) - \sinh(\frac{-y_c}{L_D})]} \quad (2.17)$$

The background flow, $U(y)$ (2.11), with Λ as defined above is shown in Figure 2.7 for a given shear and $\frac{1}{16} \leq L_D \leq 10$. The average shear in the critical layer (*i.e.* between $y = \pm \frac{2}{5}(2\pi\mu)$) is equal to the shear Λ ($= \mu$).

In the infinite Rossby deformation length experiments we defined a topographic streamfunction (ψ_{topo} , (2.8)) that coincided with the perturbation streamfunction of the SWW solution (1978). In these experiments where L_D is finite we specify a topographic forcing q_{topo} such that ψ_{topo} is the same as the infinite L_D cases. This yields

$$q_{\text{topo}} = \nabla^2 \psi_{\text{topo}} - L_D^{-2} \psi_{\text{topo}} \quad (2.18)$$

$$= -\epsilon\mu \cos(kx) \left[1 + L_D^{-2} \left(1 - \frac{\cosh y}{\cosh(2\pi\mu)} \right) \right] \quad (2.19)$$

It is important here that the streamline pattern of the background flow and the topography is the same closed streamline pattern of the infinite L_D experiments. The reason for this is that the streamline pattern shows the relative importance of $\bar{u}(0)$ and the topographic forcing and we want this to be constant across all Λ and L_D .

Figure 2.8 shows snapshots of the critical layer potential vorticity for $\Lambda = \frac{1}{8}$ at different times for different values of L_D . Figure 2.8 demonstrates that when L_D is small ($L_D < 1$) the width of the critical layer increases. This is an interesting result because we have set the problem up so that as far as possible everything is the same as the infinite L_D cases (topographic forcing, average shear in the critical layer region) and despite this we have found that the critical layer width increases at small L_D . The increase in critical layer width is due to the decrease in L_D and its consequent affect on the Rossby wave elasticity. When L_D is relatively large (Figure 2.8 (a), (b) and (c)) and we perturb the potential vorticity contours, the contours resist the motion due to Rossby wave elasticity and are therefore difficult to deform. In contrast at smaller L_D (Figure 2.8 (d) and (e)) the Rossby wave elasticity is weakened and hence there is less resistance to the deformation of potential vorticity contours resulting in a wider critical layer. Note that the increase in critical layer width is not due to a resonance with the topography (as occurred in the infinite deformation length cases). Other experiments at smaller L_D showed further increases in the critical layer width indicating that this is a trend (not resonance). Also the time evolution of the critical layers in these cases does not show linear growth in the critical layer width.

2.4.2 Scaling of the Critical Layer Width

To estimate the growth of the critical layer width at small L_D we adjust the forcing. This adjusted forcing takes into account that the potential vorticity contours are more deformable at small L_D . We require the amplitude of the topographic forcing in the critical layer to decrease as L_D decreases. The amplitude of the original topographic forcing was $\epsilon\mu$ where $\epsilon \ll 1$ (see (2.18)) and this is adjusted to

$$\epsilon\mu\frac{1}{1+L_D^{-2}} \quad (2.20)$$

The scaling factor $\frac{1}{1+L_D^{-2}}$ comes from the dispersion relation

$$\omega = \frac{\beta k}{k^2 + l^2 + L_D^{-2}} \quad (2.21)$$

where ω represents the frequency, $\beta = k = 1$ and we assume $k \gg l$. The dispersion relation demonstrates how the frequency depends on L_D , for example as L_D decreases the frequency decreases. We can think of this as the timescale over which potential vorticity contours will deform. This scaling factor enables a comparison of the critical layer evolution to be made across small L_D . Figure 2.9 displays snapshots of the potential vorticity for $\mu = \Lambda = \frac{1}{8}$ and $\frac{1}{16} \leq L_D \leq \frac{1}{2}$ where the topographic forcing amplitude has been rescaled (see (2.20)). This figure shows that the scaling factor chosen (to estimate the growth of the critical layer width with decreasing L_D) is close but is in fact a slight overcompensation as the critical layer width is now decreasing slightly at small L_D . One factor that makes it difficult to establish a suitable scaling is that the shear is not exactly the same between the finite deformation length cases. It is the average shear over the critical layer region that is the same across all L_D . Therefore the changing shape of the background shear could have a modifying influence on the effect of the scaling (2.20).

The effect of the finite deformation length on barotropic instability is shown in Figure 2.9. This figure demonstrates that the along-channel wavelength (x-wavelength) of the barotropic instability decreases at small L_D . More specifically this reduced wavelength occurs when L_D falls below the natural wavelength of the instability ($L_D < \Lambda$). Note that the time of the snapshots in Figure 2.9 increases as L_D decreases. The reason for this is the reduction in topographic forcing amplitude with L_D . It therefore takes a longer time for the forcing to

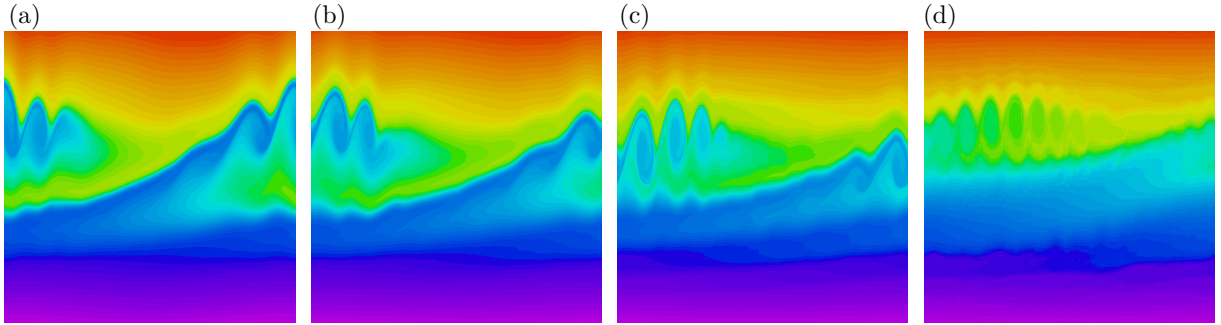


Figure 2.9: Snapshots of potential vorticity after rescaling the topography by $(1 + L_D^{-2})^{-1}$ for $\Lambda = \frac{1}{8}$ and (a) $L_D = \frac{1}{2}$, (b) $L_D = \frac{1}{4}$, (c) $L_D = \frac{1}{8}$ and (d) $L_D = \frac{1}{16}$ ($t = 1.8, 2.2, 4, 10$ respectively). Note: only the middle third of the domain is shown.

have an effect.

2.5 Conclusions

In this chapter we have investigated the evolution of barotropic instability within a critical layer. Our work differs from that of SWW (1978) and Haynes (1989) in that we force the streamfunction in the critical layer directly (rather than force laterally) using the SWW solution as a model for the critical layer. Another difference is that our numerical model is a dimensional model rather than a non-dimensional model used in Haynes (1989).

We examined the effect of the shear across the critical layer on the critical layer evolution, and more specifically on the development of barotropic instability in the critical layer. We found (consistent with Haynes (1989)) that barotropic instability occurred when the shear was suitably small, $\Lambda \leq 0.3$. As the shear across the critical layer decreased the along-channel wavelength of the instability decreased (wavenumber increased). The mixing efficiency of the critical layer increased due to barotropic instability. We also found that barotropic instability

enhances mixing in the critical layer at early times when the shear is small. However this enhancement is much smaller than the enhancement of mixing due to the resonant growth of the critical layer around $\Lambda = \frac{1}{2}$.

In an extension to previous work we carried out a systematic investigation of the critical layer evolution at finite Rossby deformation length. We set up this investigation so that as far as possible everything was the same as the infinite Rossby deformation length investigation, *i.e.* topographic forcing and average shear in the critical layer region (same closed streamline pattern). We found that regardless of this the critical layer width increased at small L_D . This was due to the effect of L_D on the Rossby wave elasticity. We therefore chose to estimate the growth of the critical layer width with decreasing L_D . We adjusted the topographic forcing amplitude using a scaling factor from the Rossby wave dispersion relation. The scaling factor chosen was close but overcompensated for the increase in the critical layer width. The scaling factor allowed a study of the effect of decreasing L_D on the barotropic instability. We discovered that at small L_D , L_D less than the natural wavelength of the instability, the wavelength of the instability reduces.

Chapter 3

The Influence of Stratospheric Potential Vorticity on Baroclinic Instability

3.1 Introduction

Wavebreaking in the stratosphere drives the Brewer-Dobson circulation and affects the mixing and transport of chemicals out of the tropical pipe (see chapter 5 for more details). In this chapter we discuss how this stratospheric wavebreaking affects the troposphere and mixing at the tropopause and the Earth's surface.

In recent years there has been much interest in the idea of dynamical coupling between the stratosphere and the troposphere. It is widely known that wave motions in the troposphere affect the stratospheric circulation, for example, planetary waves which propagate up into the stratosphere and lead to stratospheric

* This chapter is based on: Smy, L. A. and Scott, R. K. 2009. The influence of stratospheric potential vorticity on baroclinic instability. *Q. J. R. Meteorol. Soc.*, 135, 1673-1683

sudden warmings. However recent observations now suggest that the stratosphere may have an important influence on tropospheric weather and climate.

Observations of correlations between zonally symmetric anomalies of zonal wind and geopotential height in the stratosphere and troposphere (e.g. Kodera *et al.*, 1990; Thompson & Wallace, 1998, 2000; Baldwin & Dunkerton, 1999) have prompted this recent research into the dynamical coupling between these two regions of the atmosphere. These correlations are time-lagged and show tropospheric anomalies that persist on sub-seasonal timescales, longer than the corresponding stratospheric anomalies. Consequently, it has been suggested that the stratosphere may have a dynamical influence on the tropospheric circulation, even to the extent that medium-range weather forecasts might be improved by improving the representation of the stratosphere in forecast models (e.g. Scaife & Knight, 2008).

Dynamical links between the stratosphere and troposphere have been suggested to exist on both sub-seasonal and longer, inter-annual timescales. In the latter case, for example, the stratosphere has been shown to influence tropospheric circulation patterns in comprehensive general circulation models. Hartmann *et al.* (2000) investigated stratospheric ozone depletion as a possible cause for the trends observed, since the 1970's, in the stratospheric and tropospheric annular modes. The effect of stratospheric ozone on solar cycle irradiance and its resulting affect on climate change is examined by Shindell *et al.* (1999, 2001). This influence of the stratosphere on the troposphere has also been shown in simplified primitive equation models (Polvani & Kushner, 2002; Kushner & Polvani, 2004), where thermal perturbations in the stratosphere were found to significantly affect the tropospheric circulation. This indicates the possible sensitivity of the tropospheric circulation to the details of the stratospheric evolution. The stratosphere is now widely believed to play an important role in climate variability (e.g. WMO, 2007), although the dynamical processes involved are not well

understood.

On shorter timescales, on the other hand, the strong lag-correlations between the strength of the winter stratospheric polar vortex and sea-level pressure distribution (Baldwin & Dunkerton, 1999, 2001; Thompson *et al.*, 2002; Charlton *et al.*, 2003) again point to a dynamical coupling that remains, however, far from well-understood. While descending zonal wind anomalies within the stratosphere can be explained in terms of descending critical layers (Matsuno, 1971), the persistence of tropospheric anomalies on longer timescales requires consideration of additional dynamical processes. For example, Song & Robinson (2004) have suggested that stratospheric sudden warmings might couple with the troposphere through an eddy-feedback mechanism. Another recent study by Thompson *et al.* (2006) suggested, on the other hand, that the purely balanced response of the troposphere to changes in stratospheric wave drag and thermal heating may be sufficient to explain longer tropospheric correlation timescales.

The main driver of surface weather systems in the troposphere is baroclinic instability. A dynamical link between the stratosphere and troposphere involving the modulation of baroclinic instability by stratospheric zonal wind anomalies has also been considered recently (Wittman *et al.*, 2004, 2007). In simple baroclinic lifecycle experiments using a general circulation model dynamical core, Wittman *et al.* (2004) found that the strength of the stratospheric zonal winds had an influence on the tropospheric evolution, both in terms of the synoptic scale development and in zonal mean quantities, such as surface geopotential. Building on this and earlier work by Muller (1991) that examined linear growth rates in a one-dimensional Eady-type model, Wittman *et al.* (2007) further examined the dependence of growth rates on stratospheric shear in a variety of simple and more comprehensive models. In particular, they found that increasing the vertical shear above the tropopause (a representation of a strong stratospheric vortex) increased growth rates across a range of zonal wavenumbers.

In this chapter, we again investigate the dynamical link between stratospheric anomalies and baroclinic instability, but here restrict attention to anomalies that consist purely of a change to the stratospheric potential vorticity. This approach is motivated by a recognition of potential vorticity as the principle dynamical quantity governing the slow, balanced motion of the stratosphere. A strong polar vortex is an approximately zonally symmetric distribution of high potential vorticity, while a weak polar vortex may be due either to a distribution of low potential vorticity, or, alternatively, to a zonally *asymmetric* distribution of potential vorticity. The latter scenario is what is typically observed during major stratospheric sudden warmings, when strong planetary wave breaking redistributes the stratospheric potential vorticity, either through a strong displacement of the vortex (in the case of a wave-1 warming) or through a vortex split (in the case of a wave-2 warming; e.g. Charlton & Polvani, 2007). The location of the polar vortex affects the horizontal shear around the tropopause and at the surface (see figure 3.1). Therefore we expect changes to the location of the polar vortex to change the critical layer dynamics at the tropopause and at the surface. The approach adopted here allows us to examine in detail how such a redistribution of the stratospheric potential vorticity may effect the tropospheric evolution. Note also that we are interested in resultant changes to the nonlinear tropospheric evolution during the course of a baroclinic lifecycle rather than in changes to the tropospheric circulation resulting from an instantaneous potential vorticity inversion. The effects of zonal mean perturbations to the stratospheric potential vorticity on the tropospheric circulation as a direct result of potential vorticity inversion were considered by Ambaum & Hoskins (2002); Black (2002), but not their influence on baroclinic instability.

For simplicity, and to avoid the difficulties involved in balancing an asymmetric potential vorticity distribution, we use a quasigeostrophic model on an f -plane. The model configuration is described fully in section 3.2. Baroclinic

instability is arranged in the troposphere through an Eady-type distribution of potential temperature at the surface and tropopause. The case in which the stratospheric potential vorticity is exactly zero is treated as a control (discussed in section 3.3.1). Following this we consider the effect on the instability of zonally symmetric perturbations to the stratospheric potential vorticity (as a representation of a strong vortex, section 3.3.2) and asymmetric perturbations (as a representation of the vortex following a sudden warming, section 3.3.3). Finally, we briefly consider the sensitivity of our results to details of the tropospheric mean state (section 3.3.4)

3.2 Model description

The numerical model used is the contour advective semi-Lagrangian (CASL) model developed originally by Dritschel & Ambaum (1997) and extended to cylindrical geometry by Macaskill *et al.* (2003) which solves the quasigeostrophic equations on an f plane in a cylindrical domain in uniform rotation about the central axis. A quasigeostrophic framework is used since it captures the dominant balance in the atmosphere, namely large-scale low frequency motions and filters out small scales, for example gravity waves. In the model contours of constant quasigeostrophic potential vorticity are advected layerwise by the associated geostrophic velocity field. One advantage of this model is that it allows easy initialisation of both zonal and non-zonal potential vorticity anomalies and a relatively straightforward interpretation of dynamical processes.

In cylindrical coordinates (r, θ, z) the equations take the form

$$\frac{Dq}{Dt} = \frac{\partial q}{\partial t} + \mathbf{u} \cdot \nabla q = 0 \quad (3.1)$$

$$q = \frac{1}{r} \frac{\partial}{\partial r} \left(r \frac{\partial \psi}{\partial r} \right) + \frac{1}{r^2} \frac{\partial^2 \psi}{\partial \theta^2} + \frac{1}{\rho_0} \frac{\partial}{\partial z} \left(\rho_0 \frac{f_0^2}{N^2} \frac{\partial \psi}{\partial z} \right) \quad (3.2)$$

$$\mathbf{u} = \left(-\frac{1}{r} \frac{\partial \psi}{\partial \theta}, \frac{\partial \psi}{\partial r} \right) \quad (3.3)$$

together with an isothermal lower boundary condition $\psi_z = 0$ at $z = 0$.

Here q is the (anomalous) quasigeostrophic potential vorticity, ψ is the geostrophic streamfunction, and $\mathbf{u} = (u, v)$ is the horizontal geostrophic velocity. The physical parameters are the background density $\rho_0 = \rho_s \exp(-z/H)$, where H is a vertical scale height and ρ_s is a surface reference density, the ‘‘midlatitude’’ Coriolis parameter $f_0 = 2\Omega \sin 45^\circ$, where $\Omega = 2\pi \text{ day}^{-1}$ is the (planetary) rotation rate, and the constant buoyancy frequency N . Numerically, we have chosen $N \approx 0.018 \text{ s}^{-1}$ and $H \approx 8800 \text{ m}$ as being representative of the troposphere, giving a Rossby deformation radius $L_R = NH/f_0$ of approximately 1525 km.

We use an Eady type approximation in which the interior tropospheric potential vorticity is uniform and potential vorticity anomalies are concentrated in thin layers near the surface and the tropopause. The standard Eady model has a basic state consisting of a uniform vertical shear $U = \Lambda z$ corresponding to a uniform latitudinal potential temperature gradient $\Theta = -\Lambda y$, together with lower and upper boundary conditions $\psi_z = \theta$ at $z = 0$ and $z = H$. Following Bretherton (1966) this can be recast in terms of the evolution of upper and lower potential vorticity sheets with basic state

$$Q = \Theta \delta(z) - \Theta \delta(z - H) \quad (3.4)$$

together with isothermal boundary conditions at $z = 0$ and $z = H$. As discussed in Jukes (1994), replacing the upper boundary at $z = H$ with a tropopause separating regions with static stability N_{trop} (tropospheric) and N_{strat} (stratospheric) leads to the same expression but with a factor proportional to $(N_{\text{trop}} - N_{\text{strat}})/N_{\text{trop}}N_{\text{strat}}$ multiplying the sheet at $z = H$ (see Eq. 3.11 in Jukes, 1994). Since here we are interested in the dynamics of a jet localised in latitude, we generalise the Eady basic state to a nonuniform function of latitude. This motivates

the following definition for the total basic state potential vorticity

$$q = \theta_s(r)\delta(z) - \theta_t(r)\delta(z - H) + q_{\text{strat}} \quad (3.5)$$

with θ_s and θ_t corresponding to Θ in (3.4) and where q_{strat} is a basic state stratospheric potential vorticity to be specified below.

The jump in N^2 in the atmosphere will lead to tropopause dynamics (Jukes, 1994) in which potential vorticity is essentially a delta function at the tropopause. Surface temperature, θ_s , can also be considered as a sheet distribution of potential vorticity (see Hoskins *et al.*, 1985). Sheet dynamics are similar to two dimensional dynamics at large scales ($L \gg L_R$), however the equations of a sheet are more local and therefore more small scales ($L \ll L_R$) develop than in two dimensions.

The initial surface and tropopause potential temperature distributions are specified by a simple latitudinal profile of the form

$$\theta_{s,t}(r) = \Delta\theta_{s,t} \tanh((r_j - r)/w) \quad (3.6)$$

of width $2w = L_R$ and centred at $r_j = 4L_R$ (approximately 30° latitude). A hyperbolic tangent profile was chosen to represent the potential temperature jump as a compromise between $\bar{q} = H(y)$, where H is the Heaviside function ($H(y) = 0$ if $y < 0$ and $H(y) = 1$ if $y > 0$), and $\bar{q} = \beta y$. The former is singular in this model while the latter tends not to be observed since wave breaking and mixing steepen potential vorticity gradients. Furthermore we can vary the width of the profile in (3.6) with a single parameter, w . In practice we want a width of the order of a Rossby deformation radius. This is similar to the size of typical eddies developing in a baroclinic flow and therefore the zonal average potential vorticity is smooth over a distance of a Rossby deformation radius. The choice $2w = L_R$ is again a compromise between extremes. The sensitivity of our results to this parameter (w) is described briefly in section 3.3.4.

Analogously to (3.4), $\Delta\theta_{s,t}$ correspond to the pole–equator potential temperature differences at the surface and tropopause, with $\Delta\theta_s, \Delta\theta_t < 0$. The values

of $\Delta\theta_s$ and $\Delta\theta_t$ were chosen to give our model realistic shear in the troposphere (50 ms^{-1}). If there is a single jump in potential temperature then the jet associated with that jump depends linearly on the potential temperature jump (two-dimensional barotropic case). It therefore seems reasonable that \bar{u} increases linearly with the total jump in potential temperature,

$$\bar{u} = \alpha(-\Delta\theta_t + \sigma\Delta\theta_s) \quad (3.7)$$

where α and σ are constants. Note that this is an approximate equation. We deduced the velocity \bar{u} at the tropospheric jet (\bar{u}_t) and at the surface (\bar{u}_s) by setting $\Delta\theta_t = 0$ and estimating the velocity (either \bar{u}_t or \bar{u}_s) from the initial wind plots produced and then repeating this but with $\Delta\theta_s = 0$. We then set $\bar{u}_s = 0$ and $\Delta\bar{u} = \bar{u}_t - \bar{u}_s = 50$, consistent with NCEP Statistical and Climatological Analyses (http://acdb-ext.gsfc.nasa.gov/Data_services/met/mzm.html) and solved for $\Delta\theta_s$ and $\Delta\theta_t$. Choosing values $\Delta\theta_s = -0.2$ and $\Delta\theta_t = -0.6$ gives a basic state comprising a subtropical jet with a maximum \bar{u} of about 35 ms^{-1} and a vertical shear amounting to a difference of about 50 ms^{-1} between the surface and tropopause, as shown in Figure 3.1(a).

The distribution of potential vorticity in the winter stratosphere is dominated almost entirely by the polar vortex, and may be approximated most simply as a region of high potential vorticity over the pole and low potential vorticity in midlatitudes. In our model we therefore define q_{strat} by

$$q_{\text{strat}}(r, z) = \begin{cases} \Delta Q & \text{if } r < r_v, z \geq 1.5H \\ 0 & \text{otherwise} \end{cases} \quad (3.8)$$

where r_v is the vortex radius at a given height and ΔQ is the jump in potential vorticity at the vortex edge. Here the lowermost vortex is situated at a distance of $0.5H$ above the tropopause, as a crude representation of the weaker “subvortex region” and to reduce the direct effect of the stratospheric potential vorticity on

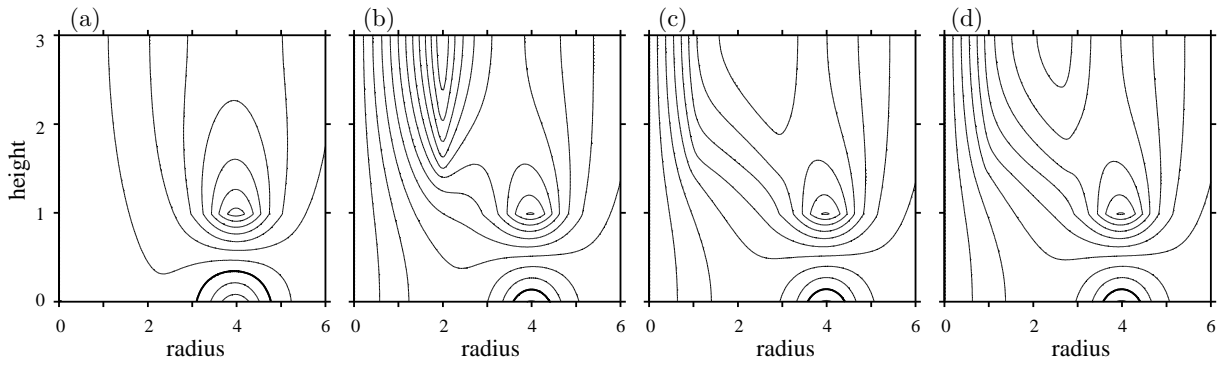


Figure 3.1: Initial zonal wind profiles of the four main cases (a) zero stratospheric potential vorticity (the control case), (b) zonally symmetric polar vortex, (c) asymmetric polar vortex (displaced) and (d) asymmetric polar vortex (split). The stratospheric potential vorticity jump in (b-d) is $\Delta Q = 0.4f_0$. The contour interval is 5 ms^{-1} .

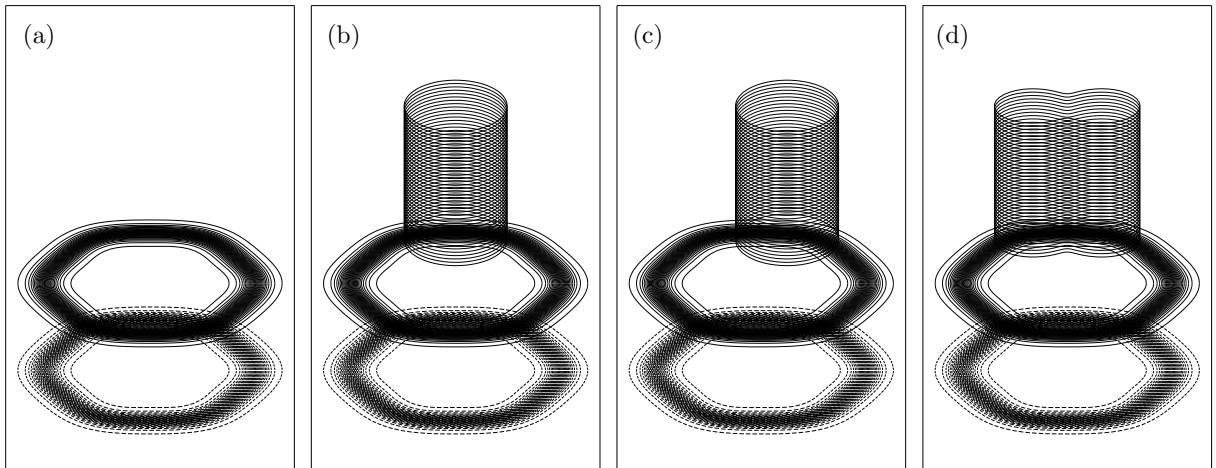


Figure 3.2: Perspective view of the potential vorticity contours in the four main cases: (a-d) as in Figure 3.1.

the tropospheric winds. It was found that the effect of the polar vortex on the tropospheric evolution is most pronounced when there is no subvortex region and decreases slightly as the region increases in depth. However, the sense of the stratospheric influence is unaffected by the depth of the subvortex region, and even the more detailed aspects of the results show very little sensitivity to the depth of the region. Here, the sub-vortex region is included to illustrate that the influence of the polar vortex on the instability is a remote influence, and not due to local interactions in the direct vicinity of the tropopause.

We consider three different forms of r_v to represent typical polar vortex regimes. The simplest form corresponds to a zonally symmetric columnar vortex with $r_v = a$ independent of height. Choosing $a = 2L_R$ gives a polar vortex edge situated near 60° latitude.

The other two forms correspond to a simple horizontal rearrangement of this profile, or deformation of the vortex edge, into a zonally asymmetric state. The first of these takes the form of a simple horizontal displacement of the vortex from over the pole, similar to a zonal wavenumber one perturbation. The amplitude of the displacement used for the experiments reported in section 3.3.3 is such that the vortex is displaced a distance L_R ; the dependence of the results on this displacement is also considered. The second asymmetric state is given by a zonal wavenumber two perturbation of amplitude η to the zonally symmetric state. In polar coordinates, the vortex boundary is displaced from $r_v = a$ (constant) to $r_v = r_v(\theta)$ where

$$r_v(\theta) = \alpha[a + \eta \cos(2\theta)] \quad (3.9)$$

where the normalisation factor $\alpha^2 = a^2/(a^2 + \eta^2/2)$ is included to ensure that the cross-sectional area of the perturbed vortex is the same as that of the zonally symmetric vortex, regardless of η . A disturbance amplitude $\eta = 2$ gives a vortex that is exactly split in a figure-eight pattern, while smaller values give a less perturbed vortex. For the results reported in section 3.3.3 we settled for $\eta = 1$.

The complete tropospheric and stratospheric vorticity distributions are shown in a perspective view in Figure 3.2. Note that we have added a weak (maximum displacement of $0.1L_D$) zonal wavenumber 6 perturbation to the surface and tropopause potential temperature fields to seed the baroclinic instability. This is the fastest growing mode, and a single wavenumber perturbation was chosen to allow direct comparison of surface potential temperature fields among different cases during the nonlinear stages of the evolution. The control case, with $q_{\text{strat}} = 0$ is shown in Figure 3.2(a) and the cases with stratospheric perturbation—zonally symmetric, displaced vortex, and split vortex—in Figure 3.2(b-d), respectively. The corresponding initial zonal velocity profiles for each case are shown in Figure 3.1

The model equations are discretized using 80 layers in the vertical between $z = 0$ and $z = 3H$. This gives a vertical domain extending from the ground to approximately the middle stratosphere. In this problem, the upper stratospheric potential vorticity has practically no impact on details of the tropospheric winds and the evolution of the baroclinic lifecycle, so this truncation seems justified. In the horizontal directions, the streamfunction and velocity fields are calculated on a stretched grid of 128 radial and 264 azimuthal points, although the potential vorticity itself is first interpolated onto a grid four times finer for more accurate inversion. The lateral boundary is located at a distance of $8L_R$ from the pole and has been verified to have practically no effect on the tropospheric evolution.

Finally, a few words are needed concerning the issue of numerical convergence. In the Eady model, the surface and tropopause dynamics exhibit a logarithmic singularity in the tangential velocity field as potential temperature fronts develop (Juckes, 1994). Further, steep potential temperature gradients are a natural feature of the nonlinear evolution during the instability. The logarithmic singularity is here regularized by the fact that the vertical discretization is finite, but increasing vertical resolution results in increasingly energetic flow at the smallest

horizontal scales. It was found by successively doubling both horizontal and vertical resolution together that, although the smallest-scale features of the model continue to exhibit differences at the highest resolution performed, large and synoptic-scale features are essentially convergent. Further, bulk quantities like the eddy kinetic energy are convergent below the resolution used for the main experiments reported below.

3.3 Results

3.3.1 Control

We first briefly describe the control case in which the stratospheric potential vorticity is exactly zero. The initial zonal wind profile for this case is shown in Figure 3.1(a) and, as described above, comprises a baroclinically unstable subtropical jet with peak wind speed of approximately 35 ms^{-1} and a vertical shear amounting to a difference of about 50 ms^{-1} between the surface and tropopause.

The growth of the instability is such that significant nonlinearity develops by around days 6–8 of the evolution, with eddy kinetic energy peaking near day 10 and then decreasing again in a decay stage, the classic baroclinic lifecycle paradigm. The synoptic surface potential temperature distribution for the control case at days 10, 12 and 14 of the lifecycle evolution is shown in Figure 3.3(a-c). Significant nonlinearity has developed by day 10 with the usual wave breaking, irreversible mixing of potential vorticity, and intensification of potential temperature gradients. Because of the simplicity of our model only a very qualitative comparison of this evolution with that observed in more sophisticated models is possible. However, the evolution can be regarded as broadly similar to the LC1 lifecycle of Thorncroft et al. (1993) with predominantly anticyclonic equatorward wave breaking during the saturation phase. Examination of the zonal mean zonal

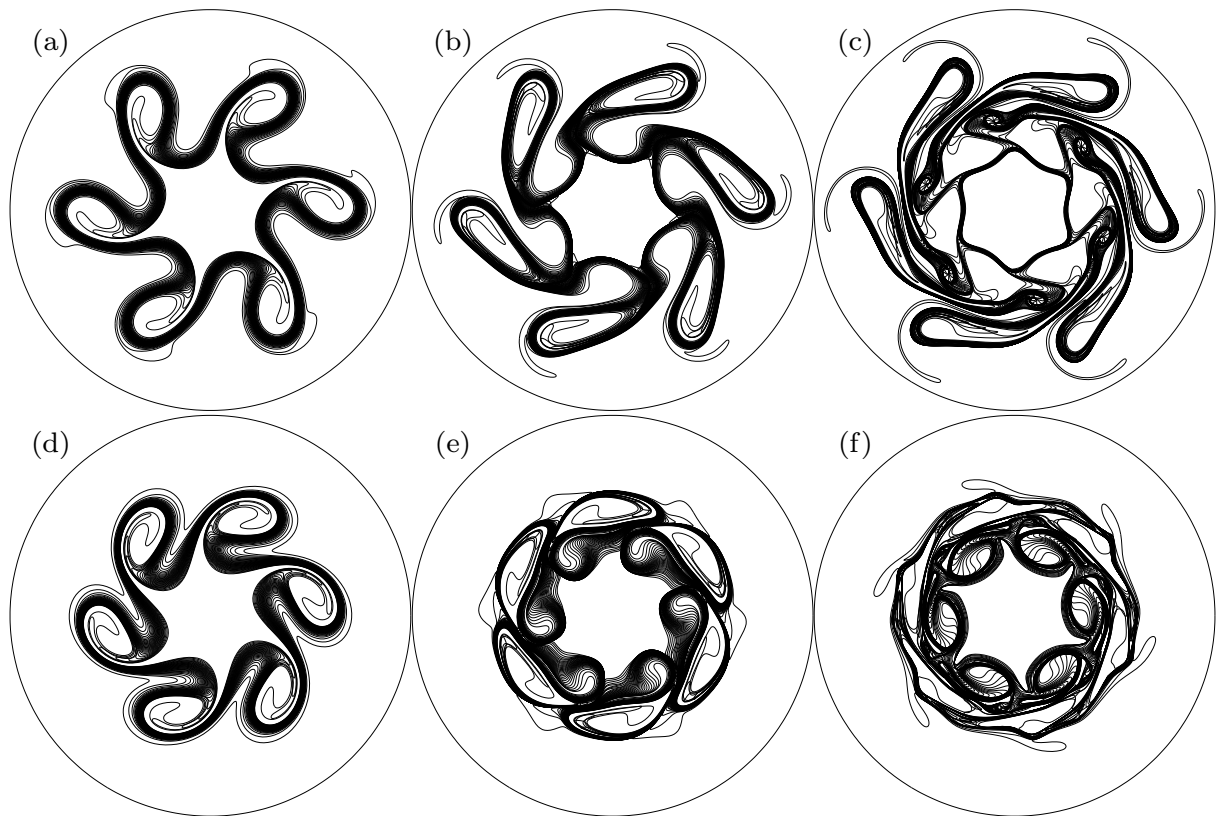


Figure 3.3: Surface potential temperature at days 10, 12 and 14: (a-c) the control case $\Delta Q = 0$; (d-f) with a zonally symmetric stratospheric anomaly of $\Delta Q = 0.4f_0$.

velocity and wave fluxes (not shown) indicate a transfer of energy into a deeper barotropic jet and an upward wave flux from the surface to the tropopause.

3.3.2 Zonally Symmetric Perturbation

To examine the effect of stratospheric potential vorticity on the tropospheric evolution we next consider cases with nonzero q_{strat} . We first consider the case of a zonally symmetric perturbation to the stratospheric potential vorticity. More realistic perturbations will follow in section 3.3.3, but we note for now that a zonally symmetric perturbation can be regarded as a crude representation of a strong polar vortex, and can therefore be contrasted with the control case discussed above (which can be regarded as an extreme example of a weak vortex). Our comparison here is similar to the situation considered by Wittman *et al.* (2004), who restricted attention to purely zonally symmetric initial conditions, with or without a stratospheric polar vortex.

The zonally symmetric perturbation to the stratospheric potential vorticity is defined by (3.8) with $r_v = a = 2L_R$. Here we focus on the case $\Delta Q = 0.4f_0$, which gives rise to a relatively strong polar vortex (in terms of \bar{u} near the vortex edge), but the intermediate case of $\Delta Q = 0.2f_0$ is also discussed briefly. As can be seen in Figure 3.1, the addition of the polar vortex in the stratosphere has a direct effect on the initial state tropospheric zonal wind due to potential vorticity inversion. Note, however, that although the tropospheric jet has increased to a maximum of 45 ms^{-1} (compared with 35 ms^{-1} in the control), the vertical shear between the surface and tropopause is largely unchanged. In contrast, the addition of the polar vortex results in a more significant change to the horizontal shear throughout the troposphere, which has a subsequent effect on the tropospheric evolution.

Figure 3.3(d-f) shows the synoptic surface potential temperature evolution for the zonally symmetric perturbation with $\Delta Q = 0.4f_0$ at days 10, 12 and 14.

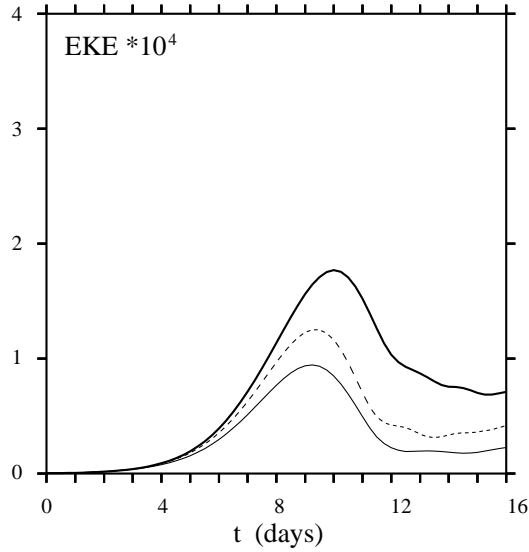


Figure 3.4: Eddy kinetic energy as a function of time for the cases with a zonally symmetric polar vortex with $\Delta Q = 0$ (bold solid), $\Delta Q = 0.2f_0$ (dashed), and $\Delta Q = 0.4f_0$ (thin solid).

Again, the baroclinic instability results in wave breaking and irreversible mixing across the jet. However, in the perturbed case increased horizontal shear throughout the troposphere results in a change in the critical dynamics and an eddy growth that is now more confined in latitude than before. This interpretation is consistent with the results of Thorncroft *et al.* (1993) where the addition of barotropic shear to the initial mean zonal flow of an LC1 lifecycle resulted in significantly different nonlinear dynamics (the LC2 lifecycle). While interpretation of the evolution shown in Figure 3.3 in terms of LC1 and LC2 lifecycles is difficult owing to the simplicity of our model, there are nevertheless clear differences between the two cases. For example, both the strong equatorward wave breaking of the control case and the weaker, poleward wavebreaking are attenuated in the case with $\Delta Q = 0.4f_0$. At later times, days 12–14, the poleward breaking in the control case results in strong transport of low-latitude air into high latitudes, which is much weaker in the perturbation case.

To quantify the change in eddy growth with changes to the stratospheric potential vorticity we show in Figure 3.4 the eddy kinetic energy as a function of time for the case of exactly zero stratospheric potential vorticity (the control, for which $\Delta Q = 0$) and two cases with increasing strength of stratospheric potential vortex anomalies, $\Delta Q = 0.2f_0$ and $\Delta Q = 0.4f_0$. At early times there is a decrease in the growth rate of eddy kinetic energy with increasing ΔQ , and, consequently, a reduction in the maximum value obtained around day 10. At first sight, this dependence might appear contrary to the results of Wittman *et al.* (2007) who found using a primitive equation model that the growth rate of eddy kinetic energy increased monotonically (at wavenumbers less than 7) with increasing vertical shear in the stratosphere, their proxy for the polar vortex. In fact, the two sets of results appear to be consistent when we take into account the details of the changes to the initial shear caused by the stratospheric perturbations in each case. In Wittman *et al.*, the addition of vertical shear in the stratosphere appears to enhance the eddy growth rate in a similar way as increasing the vertical shear in the troposphere in the traditional Eady model. In our model, on the other hand, the addition of the stratospheric potential vorticity anomaly has practically no effect on the vertical shear in the troposphere or anywhere near the subtropical jet (Figure 3.1(a) and (b)). As discussed above, however, it does increase the horizontal shear throughout the troposphere with a resultant change in the character of the lifecycle, consistent with Thorncroft *et al.* (1993). Of course, other differences between the two modelling frameworks (e.g. cylindrical versus spherical geometry, quasigeostrophic versus primitive equations, latitudinal offset between the polar vortex and the subtropical jet) may also alter details of the evolution. However, the dependence of the growth rates on the tropospheric shear would appear to be consistent.

Another useful measure of eddy growth, particularly suited to the contour

representation used here, is the wave activity A defined as

$$A(z, t) = \frac{1}{4} \rho_0(z) \sum_k q_k \oint_{\Gamma_k(z)} (r^2 - r_e^2)^2 d\theta \quad (3.10)$$

where the sum is over all contours Γ_k in a given vertical level, where r_e is the radius of the undisturbed circular contour enclosing the same area as Γ_k , and where q_k is the vorticity jump on the k th contour. This is a nonlinear pseudo-momentum based wave activity, second order in disturbance amplitude, satisfying an exact conservation relation (see Dritschel, 1988; Dritschel & Saravanan, 1994, for more details). The evolution of total wave activity contained in the surface and tropopause potential temperature fields is shown in Figure 3.5 for the three cases $\Delta Q = 0, 0.2f_0, 0.4f_0$. Like the eddy kinetic energy, the wave activity increases due to the instability, and again with weaker growth at higher values of ΔQ . At late times the difference between the cases is even more marked, with continued increase in the wave activity in the case $\Delta Q = 0$ but not in the other cases. We note incidentally that these differences in the tropospheric wave activity are entirely due to the evolution of the basic instability: the amount of wave activity “leaking” from the troposphere into the polar vortex is negligible, with values of the stratospheric wave activity remaining around five orders of magnitude less than tropospheric values throughout the evolution.

As in Wittman *et al.* (2004) it is also possible to consider the surface geopotential height difference as a crude measure of the extent to which the instability projects onto the Arctic Oscillation. Figure 3.6 shows the difference between the surface geopotential height anomaly at day 12 and day 0. The magnitude of the dipole structure resulting from the instability becomes weaker for larger values of ΔQ , consistent with the reduction of eddy growth rates discussed above. Again the different dependence on ΔQ from the dependence found in Wittman *et al.* (2004) can be understood in terms of changes to the tropospheric shear induced by the stratospheric perturbation.

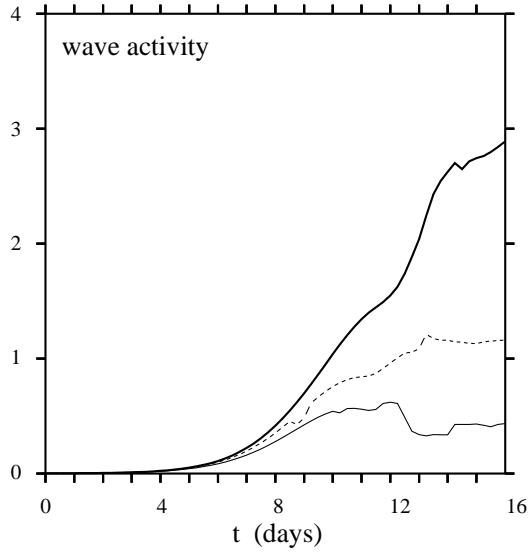


Figure 3.5: Combined surface and tropopause wave activity as a function of time for the cases $\Delta Q = 0$ (bold solid), $\Delta Q = 0.2f_0$ (dashed), and $\Delta Q = 0.4f_0$ (thin solid). Values have been normalized by the initial angular impulse of the case $\Delta Q = 0$.

Finally we examine the effect of the stratospheric perturbation on the growth rate of other wavenumber disturbances to the surface and tropopause basic state. Here we consider the difference between the two cases $\Delta Q = 0$ and $\Delta Q = 0.4f_0$ and calculate the linear growth rates of different wavenumbers by integrating the model at early times only. One reason for doing so is to verify that the addition of a polar vortex indeed reduces the growth rate at all wavenumbers rather than simply shifting the wavenumber of the fastest growing mode. As seen in Figure 3.7 this is indeed the case, with a modest reduction in growth rate across all wavenumbers.

3.3.3 Asymmetric Perturbations

We now consider the effect of asymmetric perturbations to the stratospheric potential vorticity on the tropospheric evolution. Again, these perturbations are

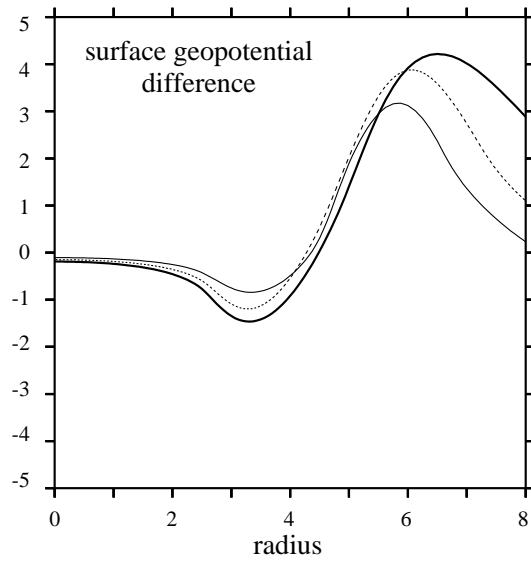


Figure 3.6: Difference between the surface geopotential at day 12 and day 0 for the cases $\Delta Q = 0$ (bold solid), $\Delta Q = 0.2f_0$ (dashed), and $\Delta Q = 0.4f_0$ (thin solid).

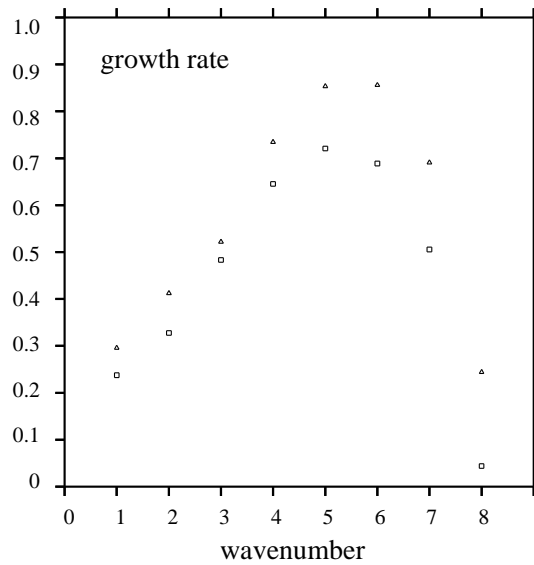


Figure 3.7: The linear growth rate of eddy kinetic energy with different initial wavenumber perturbations in the troposphere: Δ 's correspond to the control case, $\Delta Q = 0$, and \square 's correspond to a zonally symmetric stratospheric polar vortex with $\Delta Q = 0.4f_0$.

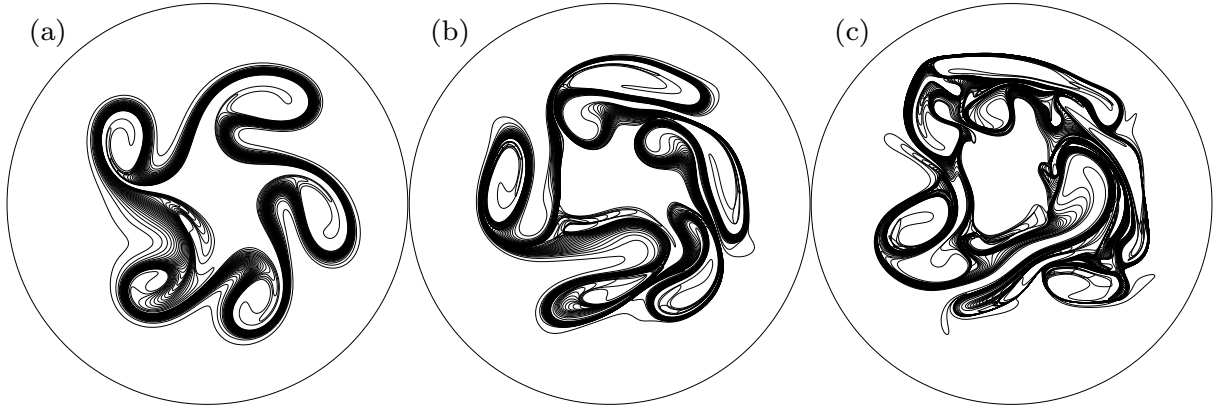


Figure 3.8: Surface potential temperature at days 10, 12 and 14 for the case of a displaced polar vortex (centred at $r = L_R$) with $\Delta Q = 0.4f_0$.

representative of the shape of the polar vortex following a stratospheric sudden warming. Here, we focus on the displaced vortex case (a wave-one warming) but note that very similar results were also obtained in the case of a split vortex.

As before, the stratospheric perturbation has an instantaneous effect through potential vorticity inversion on the tropospheric basic state, as shown in Figure 3.1(c,d) for the displaced and split vortex cases with $\Delta Q = 0.4f_0$. However, comparing with Figure 3.1(b), we see that the biggest differences in the winds between the symmetric and asymmetric vortex cases are in the stratosphere: because the asymmetric perturbation results in a latitudinally distributed zonal mean stratospheric potential vorticity, the stratospheric jet is also broader and weaker than in the case with a zonally symmetric vortex. In the troposphere, on the other hand, the winds are very similar in all cases (symmetric, displaced vortex and split vortex), in almost all respects, including the maximum of the subtropical jet and the vertical and horizontal shear. Thus the *instantaneous* effect of a rearrangement of the stratospheric potential vorticity on the tropospheric zonal flow is very small.

Figure 3.8 shows the synoptic surface potential temperature evolution at days

10, 12 and 14 for the case $\Delta Q = 0.4f_0$ and a vortex displacement of distance L_R . What is immediately apparent is the strong departure from six-fold symmetry, which results from the interaction of the fastest growing wave-six mode in the troposphere with the growth of wave-one initiated by the displaced polar vortex. Although the growth rate of wave one is much smaller than that of wave six (Figure 3.7), the wave-one perturbation induced by the displaced polar vortex is larger than the initial wave-six tropospheric perturbation, with the result that significant growth of wave one occurs. This growth is naturally smaller for smaller initial displacements of the polar vortex; however, it was found that even relatively small displacements (down to a distance of $0.2L_R$) were sufficient to cause significant development of tropospheric wave one by day 16 (with gradually later development at smaller displacement values). Thus a simple displacement of the polar vortex may have a significant effect on the tropospheric evolution.

The growth of eddy kinetic energy for the control case ($\Delta Q = 0$) and the two cases $\Delta Q = 0.2f_0$ and $\Delta Q = 0.4f_0$ (with a vortex displacement of L_R), is shown in Figure 3.9. The contribution of the initial stratospheric polar vortex displacement is evident in the eddy kinetic energy at $t = 0$. Despite these larger initial values, however, growth rates during the development of the instability are smaller at larger values of ΔQ , similar to the case of the zonally symmetric stratospheric perturbation. Essentially, the eddy growth at early times is again dominated by the fastest growing mode, despite the presence of the large wave one perturbation. This behaviour changes dramatically at later times, however, when the growth of the wave-one perturbation eventually overtakes that of the wave-six: whereas saturation of wave six occurs around day 10, saturation of wave one does not occur until around day 16 or later, at significantly higher values of eddy kinetic energy. The evolution for the case of the split vortex is qualitatively very similar to that of the displaced vortex, with large eddy growth due to the development of wave two dominating at late times. Eddy kinetic

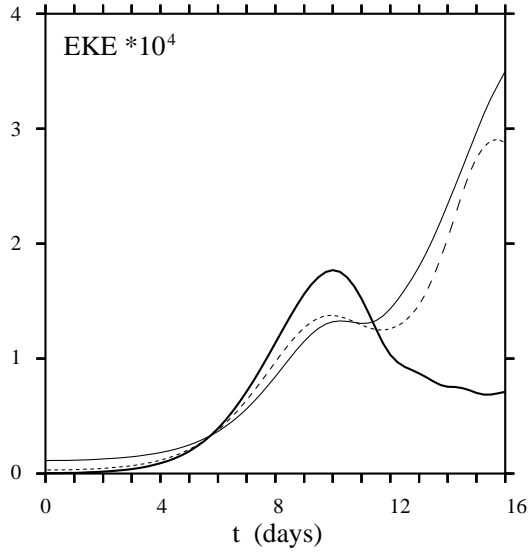


Figure 3.9: Eddy kinetic energy as a function of time for a displaced polar vortex (centred at $r = L_R$) with $\Delta Q = 0$ (bold solid, same as the control case), $\Delta Q = 0.2f_0$ (dashed), and $\Delta Q = 0.4f_0$ (thin solid).

energy plots for this case are similar to those shown in Figure 3.9, while the surface potential temperature fields show the late time development of wave four due to the interaction of the wave six and wave two initial perturbations.

Instead of comparing the tropospheric evolution at different ΔQ , it is perhaps more instructive to consider the differences between the zonally symmetric and displaced polar vortex cases, both with $\Delta Q = 0.4f_0$, the potential vorticity in the displaced vortex case being simply a redistribution of that in the symmetric case. The surface potential temperature fields (compare Figure 3.3(d-f) and Figure 3.8) are significantly different between the two cases already at day 10, but still more so at late times, when much more vigorous mixing is found across a wider latitudinal region in the displaced vortex case. Similarly, the eddy kinetic energy shows significant differences at late times (compare thin solid lines in Figure 3.4 and Figure 3.9), although growth rates at early times are similar.

The more vigorous mixing across latitude has an influence on the zonal mean

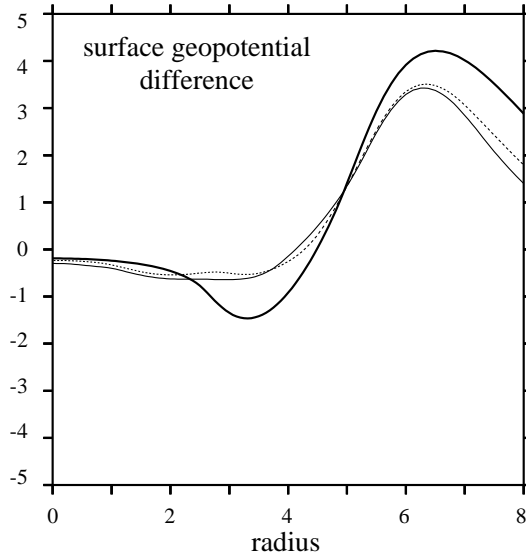


Figure 3.10: Difference between the surface geopotential height at day 12 and day 0 for the displaced polar vortex (centred at $r = L_R$) with $\Delta Q = 0$ (bold solid), $\Delta Q = 0.2f_0$ (dashed), and $\Delta Q = 0.4f_0$ (thin solid).

surface geopotential height anomalies considered above. Figure 3.10 again shows the difference between the surface geopotential height anomaly at day 12 and day 0, for $\Delta Q = 0, 0.2f_0, 0.4f_0$ but for the displaced vortex cases. As in the case of the zonally symmetric vortex, large ΔQ again results in a less pronounced dipolar structure in midlatitudes. Comparing the thin solid line in this figure with that in Figure 3.6 indicates that the redistribution of potential vorticity in the stratosphere has also had an effect on the resulting surface geopotential height following the baroclinic development.

Finally, it is again useful to consider the evolution of wave activity in these cases. At $t = 0$, the stratospheric wave activity (not shown) due to the displaced vortex is around four times that due to the initial tropospheric wave-six perturbation. This stratospheric wave activity decreases until around day 8 due to downward wave propagation (Scott & Dritschel, 2005) and is the source for the subsequent growth of wave one in the troposphere. However, the initial

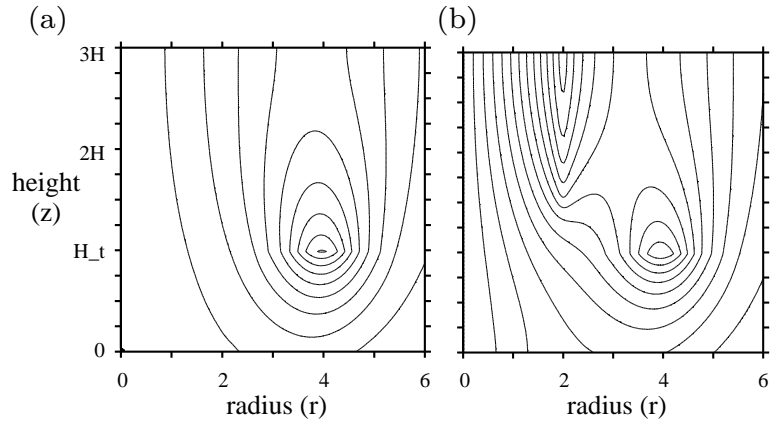


Figure 3.11: Initial zonal wind profiles for the case with broad surface temperature initial condition: (a) $\Delta Q = 0$ (the control); (b) a zonally symmetric vortex with $\Delta Q = 0.4f_0$. The contour interval is 5 ms^{-1} .

stratospheric wave activity is much smaller than the subsequent difference in the tropospheric wave activity between the zonally symmetric and displaced vortex cases, which can only be accounted for by the unstable growth of wave one, and not by simple downward propagation of waves from the stratosphere. Final (day 16) values of stratospheric wave activity are around four times larger than initially, indicating that some of the wave one development in the troposphere is able to later propagate out on the polar vortex edge (in contrast to wave six, which, as discussed above, is trapped in the troposphere).

3.3.4 Influence of the basic state

To verify that the above results are not sensitive to details of the tropospheric initial conditions we have performed a number of variations with different values for the surface and tropopause $\Delta\theta$ and different forms of the latitudinal profiles, as well as different relative positions of the polar vortex and subtropical jet. In all cases the results are broadly similar to those reported above, with increasing stratospheric potential vorticity perturbation resulting in weaker eddy growth in

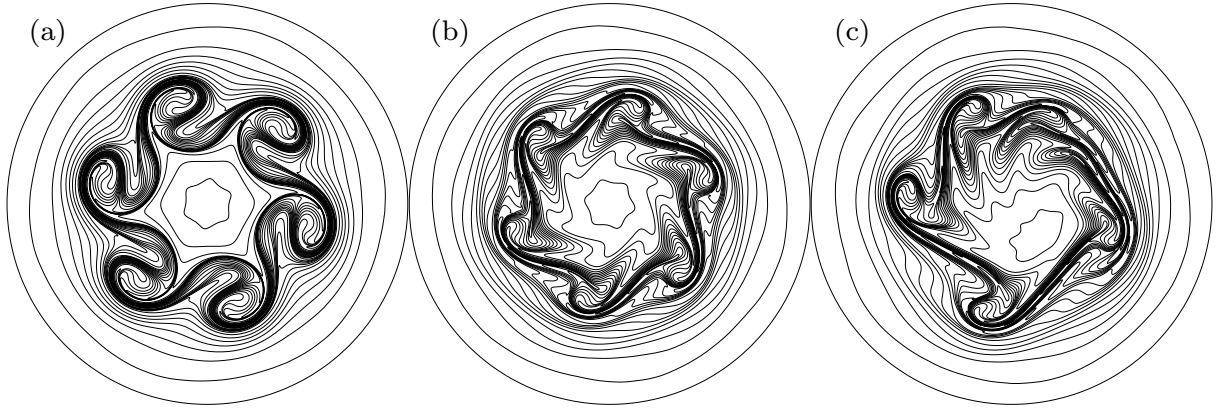


Figure 3.12: Surface potential temperature at day 14 for the case with broad surface temperature initial condition: (a) $\Delta Q = 0$ (the control); (b) a zonally symmetric vortex with $\Delta Q = 0.4f_0$ (c) a displaced polar vortex (centred at $r = L_R$) with $\Delta Q = 0.4f_0$.

the troposphere, related to changes in horizontal shear. In this section we briefly describe a few of these variations.

In one variation we consider a surface potential temperature distribution that has a broader latitudinal structure, with $2w = 4L_R$ for the surface distribution (and $2w = L_R$ at the tropopause as before). This gives a slightly more realistic zonal wind profile, as shown in Figure 3.11(a),(b) for the cases of no polar vortex and a zonally symmetric polar vortex with $\Delta Q = 0.4f_0$. The zonal winds are now increasing monotonically at all heights between the pole and the jet latitude, and decreasing equatorward of the jet, and, in particular, there is now a surface shear that is cyclonic poleward of the jet latitude, closer to the observed zonal wind profile (compare with Figure 3.1(a), where the shear just poleward of the jet location is anticyclonic). This could be important, for instance in determining the direction of synoptic wave breaking during the evolution of the lifecycle, where, for example, the poleward wave breaking in Figure 3.3 appears initially anticyclonic. We emphasize, however, that here we are less interested in the

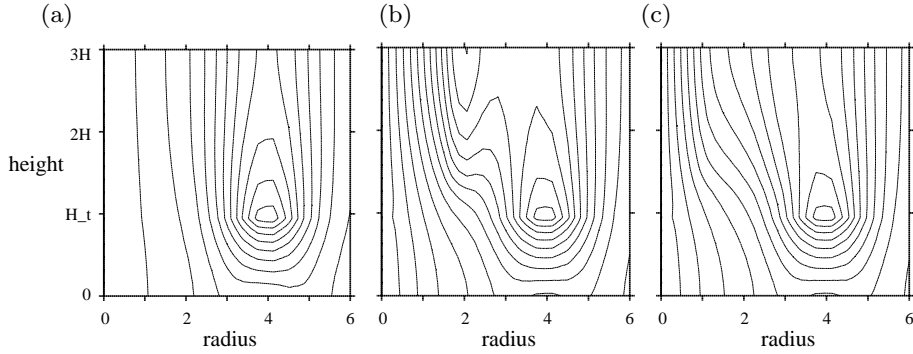


Figure 3.13: Initial zonal wind profiles for the case with barotropic shear : (a) $\Delta Q = 0$ (the control); (b) a zonally symmetric vortex with $\Delta Q = 0.4f_0$; (c) a displaced vortex (centred at $r = L_R$) with $\Delta Q = 0.4f_0$. The contour interval is 5 ms^{-1} .

details of the synoptic development as on the influence of the polar vortex on the overall growth rate of the instability.

Figure 3.12 shows the surface potential vorticity at day 14 for three cases: (a) with $\Delta Q = 0$, similar to the control case discussed above; (b) with $\Delta Q = 0.4f_0$ and a zonally symmetric vortex; and (c) with $\Delta Q = 0.4f_0$ and a vortex that has been displaced horizontally by a distance L_R . The corresponding figures from the previous cases are the right hand panels in Figures 3.3 and 3.8. The increase in cyclonic meridional shear poleward of the jet has resulted in slower growth of the instability across all cases, although the poleward breaking remains initially anticyclonic. However, and more importantly, the difference between cases remains much the same as before. The largest eddy growth is for the case $\Delta Q = 0$. In terms of both eddy kinetic energy and wave activity (not shown) the largest growth is again for the case $\Delta Q = 0$, while in the cases with $\Delta Q = 0.4f_0$ the case of the displaced vortex again exhibits larger eddy growth at late times than the case of the zonally symmetric vortex.

In a second variation we considered the effect of simply adding a r -dependent barotropic shear to the initial state, similar to the LC2 lifecycle case considered

in Thorncroft *et al.* (1993). This was done by adding a velocity profile $u(r)$ throughout the model.

$$u(r) = u_0 \cos^2 \left(\frac{r - r_j \pi}{w_s} \right) \quad (3.11)$$

where $u_0 = 0.02$, $w_s = 2L_R$ is the width of the velocity profile and the profile is centred at $r_j = 4L_R$. The resulting initial zonal wind profiles are shown in Figure 3.13 for three cases with (a) no polar vortex; (b) a zonally symmetric polar vortex with $\Delta Q = 0.4f_0$; and (c) with $\Delta Q = 0.4f_0$ and a vortex displaced in the horizontal by a distance L_R . These initial zonal wind profiles are broadly similar to those shown in Figure 3.11, as is the subsequent evolution (not shown). In particular, we again found a robust decrease in the growth rate of the instability when the polar vortex was added, and a late time increase in eddy kinetic energy in the displaced vortex case due to the growth of low wavenumbers.

Finally, we considered a basic state characterized by two surface temperature fronts located poleward and equatorward of jet latitude;

$$\theta_s(r) = \Delta\theta_s \left[\tanh \left(\frac{2L_R - r}{w} \right) + \tanh \left(\frac{6L_R - r}{w} \right) \right] \quad (3.12)$$

Such a distribution arises naturally as a result of eddy mixing of surface temperature due to baroclinic waves, and can be considered to represent the statistically stationary state of the atmosphere. This state would also be obtained by zonally averaging the final temperature distributions in the above calculations. For completeness, therefore, we repeated the main series of experiments using this tropospheric basic state, although it could be argued that such a state is not the most appropriate choice of initial conditions in the lifecycle approach since it is the equilibrium achieved after a lifecycle has occurred. We never know what the basic state of the atmosphere is because the dynamics of the instability are always taking place. In fact, we found that the details of this surface temperature basic state made very little difference to the influence of the polar vortex on the instability, with an increase in polar vortex strength again resulting in a decrease

in growth rate. Overall, it appears therefore that the influence of the polar vortex on the evolution is insensitive to details of the initial basic state, at least within the limitations of our restricted model.

3.4 Discussion

To summarise our results, changes to the stratospheric potential vorticity have a significant impact on the development of baroclinic instability in an Eady-like model. The dependence is such that increasing the strength of the polar vortex tends to decrease the eddy growth in the troposphere. This is found not just in the zonally symmetric cases, comparing zonally symmetric stratospheric perturbations of different potential vorticity magnitudes, but also in cases of zonally asymmetric disturbances to a polar vortex of given potential vorticity. The latter scenario extends previous work that has considered only zonally symmetric stratospheric perturbations. In particular, we found that there is a large difference in the tropospheric evolution between cases representing a strong vortex and cases representing the vortex following either a wave-one or wave-two sudden warming. Differences in the tropospheric evolution include the growth of eddy kinetic energy and wave activity, as well as synoptic scale details of the wave breaking and the latitudinal extent of mixing within the troposphere.

Our study differs fundamentally in philosophy from the related work of Wittman *et al.* (2004, 2007) in which perturbations were made to the stratospheric zonal winds. It is of course true that by perturbing the stratospheric potential vorticity, as is done here, one is also perturbing the tropospheric zonal flow. However, because of the fundamental nature of the potential vorticity (e.g. Hoskins *et al.*, 1985) it is perhaps justified to consider such stratospheric potential vorticity perturbations as dynamical perturbations to the stratosphere only. In our case, these perturbations have been carefully isolated from the troposphere by includ-

ing a “subvortex” region between the troposphere and lowermost polar vortex in which the potential vorticity is unperturbed. Moreover, actual differences in the initial tropospheric zonal winds between zonally symmetric and asymmetric perturbation cases are very slight (compare Figure 3.1(b-d)). Finally, this kind of perturbation is arguably closer to the situation resulting from a stratospheric sudden warming. One of the important results of the present work is that the potential vorticity perturbations made here result in significantly larger differences to the tropospheric evolution than obtained by perturbations to the stratospheric winds alone.

One significant difference between our results and those of Wittman et al. is the sense in which a stratospheric perturbation affects the growth of the instability. Wittman et al. found an increase in eddy growth rates with increasing stratospheric shear, whereas we find a decrease in growth rates with increasing stratospheric potential vorticity. The results are not inconsistent when full account is taken of changes to the tropospheric shear resulting from the stratospheric potential vorticity perturbation in our case, which tends to leave the vertical shear unchanged but increases the horizontal shear. The decrease in growth rates we observed may therefore be attributed to a change in the nature of the baroclinic development similar to that found by Thorncroft *et al.* (1993). One conclusion that may be drawn from both Wittman et al. and the present work is that the tropospheric evolution depends rather sensitively on the stratospheric state through details of the shear in the troposphere and near the subtropical jet.

Chapter 4

An Online Trajectory Model

Before proceeding further with a detailed analysis of mixing and transport in another context we introduce a tool which will be used to investigate the effect of the quasi-biennial oscillation on transport and mixing in the stratosphere. Examining lateral mixing and transport in the stratosphere requires us to be able to follow Lagrangian particles and thus motivates the use of a trajectory model.

The trajectory model we use is based on the “Offline” trajectory code written by John Methven at Reading University in 1997 (Methven, 1997). We have modified and developed this code to ensure compatibility and integration within the unified model (UM), the general circulation model that is developed and used at the UK Met Office. These developments allow trajectories to be calculated with greater accuracy.

4.1 Offline trajectory code

The “offline” trajectory code calculates trajectories from ECMWF data or data output from the University of Reading’s spectral model. The term “offline”

denotes that the input data, comprising the advecting wind fields, has been output from a model. The trajectory calculations involve solving the first order ordinary differential equation

$$\frac{d\mathbf{x}}{dt} = \mathbf{u}(\mathbf{x}, t) \quad (4.1)$$

where \mathbf{x} is a particles position in space, \mathbf{u} is the four dimensional wind field (space and time) and t denotes time. A brief outline of how the code works is displayed in Figure 4.1. The particles can be initialised in a variety of ways: on a specific model level or levels, on pressure surfaces, or on isentropic surfaces. The distribution of the particles in longitude and latitude can also be varied allowing them to be initialised in a region of particular interest.

Wind records from ECMWF are typically six hourly, twelve hourly or daily. The time interval between wind records is divided into N subintervals, where typically $N = 10$, to give a constant integrator timestep, δt . The four dimensional wind records, (x, y, z, t) , are interpolated to the current particle positions in space and time. Then a fourth order Runge-Kutta numerical integration method is used to advect the particles over the integrator timestep δt . This process is repeated until the particles have been advected to the time of the second wind record.

As well as advecting particles the “offline” trajectory code can assign the values of meteorological fields such as temperature, potential vorticity and water vapour as attributes to the particles. The values of these fields are interpolated to each particles position at each timestep. Being able to assign attributes to particles is a very useful tool which can be used to diagnose possible non-conservative forces, to diagnose the minimum temperature encountered along a trajectory (important for setting the water vapour concentrations) and also to trace a specific group of particles, for example those that started within the polar vortex.

These trajectory calculations are all particle trajectories rather than air par-

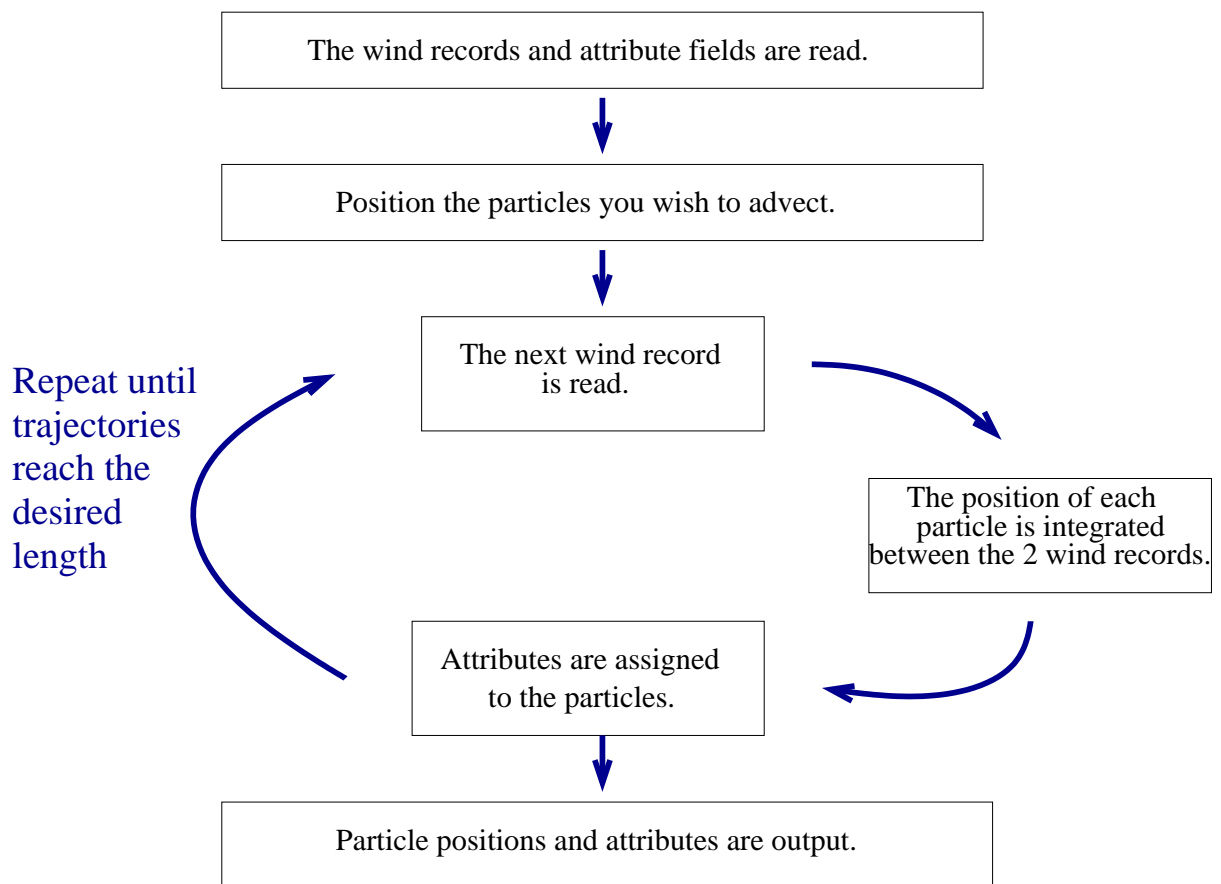


Figure 4.1: Flow chart outlining the "offline" trajectory code.

cel trajectories in the sense that we track the path of a point in the flow by integrating (4.1). An air parcel can be thought of as a finite volume of air with certain characteristics. In a chaotic flow, any volume no matter how small will be stretched and ultimately folded. Therefore in a chaotic flow an air parcel has a finite existence whereas a particle trajectory can exist indefinitely.

A limitation of the “offline” trajectory code is in calculating full Lagrangian means which are sensitive to the sampling frequency. The normal six hourly sampling frequency of the “offline” trajectory code results in small scale motions, such as the up and down wave motion within the tropical stratosphere, being missed leading to inaccurate vertical velocities.

4.2 Online trajectory code

This limitation of the “offline” trajectory code can be improved by adapting the code so that it can be implemented within the unified model, thus creating an “online” trajectory code. The code will use only the model winds at each timestep (twenty minutes) to advect the particles. Therefore, in contrast to the “offline” trajectory code, the time interval between the model winds will not be divided into N subintervals, i.e. $N = 1$. The increased sampling frequency of the “online” trajectory code (every twenty minutes), compared to the “offline” trajectory code (six hourly), leads to more accurate trajectory calculations and hence more accurate Lagrangian mean vertical velocities.

Modifications to the “offline” trajectory code involved changing the vertical coordinate in the trajectory calculations from an eta coordinate (η) to a hybrid height coordinate (UM vertical coordinate). The eta coordinate is defined as a pressure coordinate at the upper levels of the model, a hybrid sigma-pressure coordinate at middle levels and finally as a sigma coordinate near the model surface. In the eta coordinate pressure is defined by

$$p_k = A_k + B_k p_{\text{surf}} \quad (4.2)$$

where k is a vertical level index, p_k is the pressure at the level k , p_{surf} is the surface pressure and A and B are constants that vary with height. The UM hybrid height coordinate is defined as

$$z(i, j, k) = a(k) + b(k) * \text{orog}(i, j) \quad (4.3)$$

where a has dimensions of height and b is non-dimensional. However, we chose to adapt the vertical coordinate in the trajectory calculations to pressure coordinates rather than hybrid height coordinates. This was because it significantly reduces the computational expense (31 pressure levels compared with 60 model levels) and volumes of air are better represented in a pressure coordinate system. Although not ideal our main focus is on the science and therefore we have taken this pragmatic approach.

Once the “offline” trajectory code could calculate particle trajectories using output from the unified model it had to be implemented within the unified model and called from a suitable routine at each timestep, making it “online”. In order to do this the trajectory code no longer had to read data from an output file. Instead the required global fields to calculate particle trajectories needed to be passed into the trajectory code. To keep data output files to a reasonable size trajectory positions and attributes are output every six hours. Note that there is no loss of accuracy here since the trajectories are still calculated every twenty minutes.

The “online” trajectory model can currently be run as part of a version 7.3 unified model run. The trajectory model has 31 layers in the vertical between $p = 1000\text{hPa}$ and $p = 0.1\text{hPa}$. This results in a vertical domain extending from the ground to the middle mesosphere. The global fields required for the trajectory calculation are U and V components of the velocity on pressure levels, the vertical

pressure velocity omega $\left(\omega = \frac{dp}{dt}\right)$ on pressure levels and surface pressure. If any meteorological fields are desired as attributes to the particles then they must also be retrieved and passed into the trajectory code. Currently the code is set up to have temperature, potential vorticity and water vapour as attributes to the particles. In the horizontal the global velocity fields (also temperature, potential vorticity and water vapour) are calculated on a grid of 192 longitudinal and 144 latitudinal points. The surface pressure field is on a different horizontal grid with 192 longitudinal and 145 latitudinal points. The particles to be advected in the trajectory calculation can be initialised on the model pressure levels or on any pressure level inbetween them. On each pressure level the particles can be spaced regularly in latitude and longitude or so that they are distributed approximately equally in area. At the moment the maximum length of the trajectory calculation is around forty days for 35,200 particles initialised over two pressure levels. This is due to an increase in memory with the number of particles advected. In the future it may be possible to create another model run which will take the particles positions at $T = 40$ days and advect them forward for another 40 days, using the velocity fields at $T = 40$ days. More details on where to find the “online” trajectory code and specific parameter information can be found in chapter 7.

4.3 Error Analysis

This section examines the accuracy of the trajectory calculations of the “online” trajectory code compared to those of the “offline” trajectory code. This is achieved by comparing the results of seven “online” trajectory calculations (the term “online” indicates that the wind fields are passed into the trajectory code during the model run) with varying temporal resolution of the wind records (we subsample the “online” winds in time). All of these calculations begin on the 1st of January 1983 and are forty days long. The particles are initialised on the

50hPa level and are distributed every 1° in longitude and latitude from 30°N to 30°S . The differences between these trajectory calculations are summarised in Table 4.1. The control case is that which we refer to as the “online” trajectory code where the trajectories are calculated every twenty minutes (Unified Model timestep). Case 6 in Table 4.1 is equivalent to the “offline” trajectory code since trajectories are calculated every six hours (i.e. the time interval between wind records is six hours). Another difference between these calculations is the number of Runge-Kutta integrator timesteps (N in Table 4.1) used to advect the particles between the two wind records. For these calculations the Runge-Kutta integrator timestep, δt , is twenty minutes and therefore in the control case the particles are advected once to the current wind record. When N is greater than one then the time interval between the two wind records is broken down into N integrator timesteps. The four dimensional winds are interpolated to the current particle positions in space and time and then the particles are advected over the integrator timestep (4th order Runge-Kutta numerical integration method). This is repeated $N-1$ times until the particles have been advected to the time of the current wind record. In case six (equivalent to the “offline” trajectory code) the number of integrator timesteps is $N = 18$. However in the original “offline” trajectory model N is typically ten.

In order to assess the accuracy of the trajectories from the subsampled winds we examine several properties of the trajectories. Firstly, we consider the horizontal and vertical advection errors in the trajectory calculations. These errors are normalised by typical horizontal and vertical length scales (the ratio of horizontal to vertical length scales is appropriate for motion in the atmosphere) which allows a comparison between the horizontal and vertical advection errors. The vertical advection error is averaged over all the particles and is defined as

$$\bar{E}_v = \frac{1}{n} \sum_{i=1}^n \frac{1}{H} \sqrt{(z_i - z_i^*)^2} \quad (4.4)$$

Table 4.1: Error Analysis Cases

Case	Temporal Resolution of Winds	N	Frequency of Trajectory Output
control	20 mins	1	6 hrs
1	1 hr	3	6 hrs
2	2 hrs	6	6 hrs
3	3 hrs	9	6 hrs
4	4 hrs	12	12 hrs
5	5 hrs	15	30 hrs
6	6 hrs	18	6 hrs

where n is the total number of particles ($n = 21960$), z is the particles height (km), * denotes the control case (“online” trajectory code where the trajectories are calculated every twenty minutes, i.e. each model timestep), and $H = 7\text{km}$ is a typical middle atmosphere scale height.

The horizontal advection error (averaged over all the particles) is specified as follows

$$\bar{E}_h = \frac{1}{n} \sum_{i=1}^n \frac{1}{L} \sqrt{(dx_i)^2 + (dy_i)^2} \quad (4.5)$$

where

$$dx_i = x_i - x_i^* = a \cos \phi_i \lambda_i - a \cos \phi_i^* \lambda_i^* \quad (4.6)$$

and

$$dy_i = y_i - y_i^* = a d\phi = a(\phi_i - \phi_i^*) \quad (4.7)$$

Here n is the total number of particles, * denotes the control case, ϕ represents latitude, λ represents longitude, $a = 6371\text{km}$ is the radius of the Earth and

$L = NH/f \approx 2147\text{km}$ is a typical horizontal length scale where $N^2 = 5 \times 10^{-4}\text{s}^{-2}$ is the stratospheric buoyancy frequency squared, $H = 7\text{km}$ and f is the Coriolis parameter ($f = 2\Omega \sin \phi$, where $\Omega = 2\pi(\text{day})^{-1} = 7.292 \times 10^{-5}\text{s}^{-1}$) defined at $\phi = 30^\circ$ (edge of the tropical pipe). Note that both the horizontal and the vertical advection errors are non-dimensional.

Figure 4.2(a) displays the vertical advection error for different temporal resolutions of the winds at four different times since initialisation. It is clear that as the temporal resolution of the winds decreases the vertical advection error increases. Also the vertical advection error increases as the trajectory length increases (i.e. increasing time since initialisation). Figure 4.2(b) is the same as Figure 4.2(a) except that it shows the horizontal advection error. This error behaves in the same way as the vertical advection error. However the horizontal advection errors are significantly larger than the vertical advection errors and therefore it dominates over the vertical advection error. Note that there are many different sources of error, for example, the model winds are incorrect etc. However it is only the numerical errors in the trajectory calculation due to the temporal resolution of the winds which we are interested in here. It is important to note that in Figures 4.2(a) and (b) the “online” trajectories are significantly more accurate than the other trajectories with lower temporal resolution of the winds.

In addition to the horizontal and vertical advection errors we also examine the ensemble mean particle height at different times since initialisation. The ensemble mean particle height is defined as

$$\bar{z} = \frac{1}{n} \sum_{i=1}^n z_i \quad (4.8)$$

where n is the total number of particles and z is the particle’s height (km). Figure 4.3 displays the ensemble mean particle height (in meters) for different

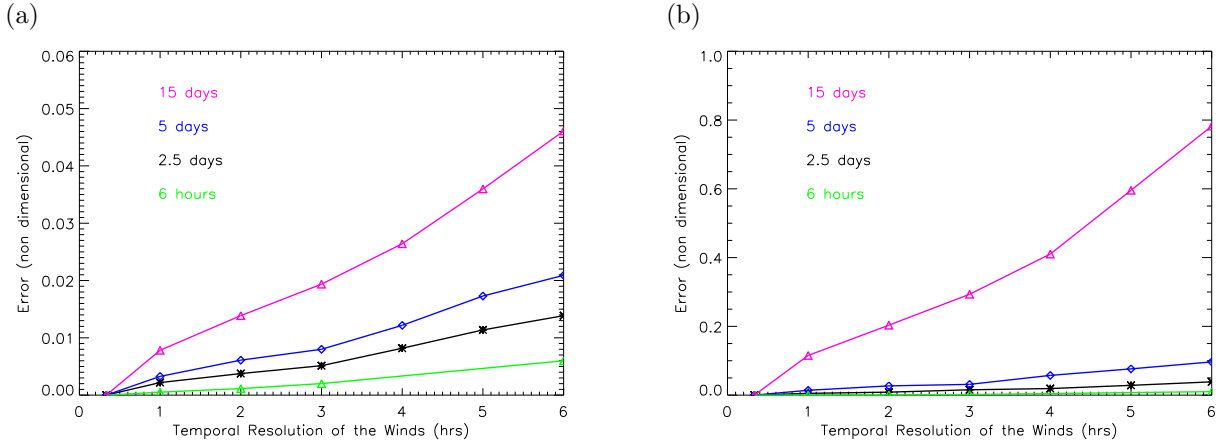


Figure 4.2: (a) Vertical advection error and (b) horizontal advection error for different temporal resolutions of the winds.

temporal resolutions of the winds at six different times since initialisation. As time increases the ensemble mean particle height is greater, at a given time, in the cases where the temporal resolution of the winds is high (\bar{z} highest for the “online” trajectory code) than when the temporal resolution of the winds is low. This demonstrates that the upward velocity is decreasing as the temporal resolution of the winds decreases. Therefore Figure 4.3 indicates that there is a systematic bias caused by the sampling frequency of the model winds (temporal resolution). One possibility is that when the temporal resolution of the winds is low errors in the horizontal advection could mean that more particles have moved out of the tropics, and begin to descend, compared with the trajectories with higher temporal resolution of the winds. If this is the case the ensemble mean particle height will not increase as much as in the cases with high temporal resolution of the winds (i.e. control case). However a comparison of trajectories from the control case (“online” trajectory code) and case 6 (equivalent to the “offline” trajectory code) indicate that the percentage of particles outside of 30°N to 30°S at different times since initialisation were almost identical (1% maximum difference). Therefore the difference in the ensemble mean height between the

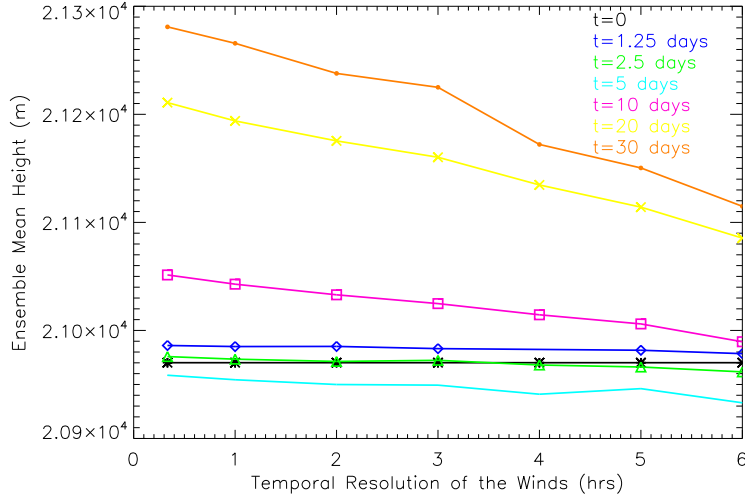


Figure 4.3: Ensemble mean particle height at different times after initialisation for different temporal resolutions of the winds.

“online” trajectory code and the “offline” trajectory code is not due to errors in the horizontal advection. It is evident that the subsampling is having an effect on the vertical motion as it stands. This could be due to the errors in the vertical advection (as shown in Figure 4.2(a)). It could also be due to the up and down wave motion in the tropical stratosphere being missed at low temporal resolution resulting in inaccurate vertical velocities which therefore cause the particles to drift upwards more slowly. Note that we also investigated the ensemble variance to determine how much the ensemble spread, however in all seven cases the variance was too large to be able to draw any sensible conclusions.

In this chapter we have described a new tool which is the “online” trajectory code. This “online” trajectory code with its high temporal resolution of the winds is significantly more accurate than the “offline” trajectory code, particularly in the horizontal. In the following chapter this more accurate trajectory model will be used to investigate the affect of the quasi-biennial oscillation phase on lateral mixing and transport in the stratosphere.

Chapter 5

The Effect of the Quasi-Biennial Oscillation on Transport and Mixing in the Stratosphere

5.1 Introduction

The Brewer-Dobson circulation (Brewer, 1949; Dobson, 1956) is a large-scale middle atmosphere circulation responsible for the long-time persistent transport of air and chemical constituents from the troposphere into the stratosphere. This circulation is named after the pioneering work of Alan Brewer and Gordon Dobson in the middle of the 20th century. Dobson *et al.* (1929) and later Dobson (1956) deduced, from measurements of ozone, that there must be some form of lateral transport from the equator to the pole in the stratosphere. Independently, Brewer (1949) examined the distribution of water vapour in the stratosphere and inferred that air had to enter the stratosphere from the tropical troposphere. Although they did not discuss dynamics (forcing of the circulation), the inferences drawn about this circulation were broadly correct.

More specifically, the Brewer-Dobson circulation can be regarded as a mean meridional circulation describing the long-time persistent mean motion in the height-latitude plane (averaging out wave motions on short time scales). It consists of upwelling in the tropics, poleward lateral transport in the lower and middle stratosphere (both hemispheres) and, consistent with mass conservation, downwelling in middle to high latitudes. At higher altitudes the circulation is more asymmetric with lateral transport from the tropics to the winter pole (see Figure 2(a) Solomon *et al.* (1986)). Note that the Brewer-Dobson circulation is a weak motion compared with the dominant motions in the stratosphere which are quasi-horizontal. The strong stable stratification of the stratosphere inhibits vertical motions. Therefore to drive motion across stratified surfaces there must be thermal forcing (heating will cause air parcels to cross isentropic surfaces) and mechanical forcing from breaking Rossby waves in the extratropical stratosphere (this drives the Brewer-Dobson circulation and is explained in more depth later).

The Brewer-Dobson circulation is important for transporting chemicals from the troposphere into the stratosphere. The distributions of water vapour (H_2O), carbon dioxide (CO_2) and ozone (O_3) are responsible for the thermal structure of the stratosphere by direct heating. For example, the absorption of solar ultraviolet radiation by the ozone layer results in an increase of temperature with height in the stratosphere. The circulation itself has a direct thermal effect. Air in the tropical troposphere is drawn upwards by the circulation, it expands due to the reduced pressure and this expansion results in the temperature of the air decreasing. Where this reduction in temperature due to ascent is strongest is known as the thermal tropical tropopause or cold trap. On the other hand, over the poles air is descending which causes its temperature to increase. When the air that is rising in the tropics passes through the thermal tropical tropopause it is dehydrated by condensation of water vapour: moisture in the air condenses into water or ice which is more dense than air and so falls back into the tro-

posphere. This dehydration of air entering the stratosphere will have an effect on the stratospheric distribution of water vapour (low H_2O). It therefore affects the thermal structure. Another important consequence of the Brewer-Dobson circulation is that ozone depleting substances (CFCs) are transported into the stratosphere where they are responsible for the destruction of ozone.

The winter polar stratosphere is dominated by the polar vortex. Due to cooling over the winter pole (the winter pole is tilted away from the sun) there is a strong eastward flow around the pole in the stratosphere which is the polar vortex (cyclonic vortex). This situation allows the propagation of planetary scale Rossby waves from the troposphere into the stratosphere since they can only propagate into the stratosphere when the stratospheric winds are eastward and not too strong (Charney & Drazin, 1961)(In either hemisphere in summer the stratospheric winds are westward and therefore Rossby waves are unable to propagate). Also more planetary scale Rossby waves are excited in the northern hemisphere since there is more longitudinal variation in topography and land-sea temperature contrasts than in the southern hemisphere. This stronger planetary wave forcing leads to more Rossby wave breaking in the northern hemisphere which gives rise to a stronger Brewer-Dobson circulation and a colder tropical tropopause during the northern hemisphere winter. There is therefore an annual cycle in the tropical tropopause temperatures (Yulaeva *et al.*, 1994) and air passing through the tropical tropopause at the time when the lowest tropical tropopause temperatures occur is dehydrated the most. This along with the upwelling in the tropical lower stratosphere produces a vertically propagating signal in water vapour known as the tropical tape recorder (Mote *et al.*, 1996). Ascent rates in the tropical lower stratosphere have been estimated from the tropical tape recorder signal to be about 0.2mms^{-1} .

These large amplitude planetary scale Rossby waves propagate up from the troposphere and then break in a region of the stratosphere known as the surf zone

(McIntyre, 1982; McIntyre & Palmer, 1983, 1984). The surf zone is a large Rossby wave critical layer. Due to the stable stratification of the stratosphere, wave oscillations are predominantly quasi-horizontal, along isentropic surfaces. When Rossby wave breaking occurs it mixes air isentropically over large latitude bands of the stratosphere. In particular Rossby wave breaking rapidly and irreversibly deforms material contours (such as potential vorticity) along isentropic surfaces. This is a very nonlinear process. McIntyre & Palmer (1983) and McIntyre & Palmer (1984) examined coarse-grain maps of potential vorticity on isentropic surfaces in the northern winter hemisphere stratosphere. These maps made the large-scale wave breaking in the surf zone visible for the first time.

The large-scale mixing of the stratospheric surf zone draws air from the polar vortex equatorward and tropical air poleward. It therefore brings together masses of air from different regions of the stratosphere. This mixing of air, due to Rossby wave breaking, homogenises potential vorticity and chemical concentrations within the surf zone, thus destroying the background potential vorticity gradient there. As a result the potential vorticity gradient steepens at the edges of the mixing region inhibiting further mixing. The surf zone is bounded by these sharp gradients of potential vorticity which correspond to the edge of the polar vortex and the subtropical barrier.

The Brewer-Dobson circulation and the surf zone are related because they are both a result of planetary wave breaking. The Rossby wave breaking in the surf zone provides a force against the flow (westward force, eastward flow) which produces a deceleration of the mean flow. This force is commonly known as wave drag. Considering a long time average of the atmosphere (*i.e.* steady state, $\frac{\partial}{\partial t} = 0$) the angular momentum contours are vertical with an equatorward gradient. The absolute zonal angular momentum per unit mass is

$$\bar{m} = a^2\Omega\cos^2\phi + au\cos\phi \quad (5.1)$$

where a is the radius of the Earth, ϕ is latitude, Ω is the Earth's rotation rate (i.e. $2\pi(\text{day})^{-1} = 7.292 \times 10^{-5}\text{s}^{-1}$) and u is the longitudinal component of velocity. Note that the first term in (5.1) is much larger than the second term. In order for particles to cross these surfaces of constant angular momentum they require a force. The quasi-geostrophic Transformed Eulerian Mean (TEM) equation for the zonal mean longitudinal component of the velocity field is

$$\frac{\partial \bar{u}}{\partial t} - f_0 \bar{v}^* = \frac{1}{\rho_0} \nabla \cdot \mathbf{F} \quad (5.2)$$

where \bar{u} is the zonal mean longitudinal component of velocity, f_0 is the Coriolis parameter, \bar{v}^* is the latitudinal component of the residual mean meridional circulation, ρ_0 is a reference density and \mathbf{F} denotes the Eliassen-Palm flux which represent the flux of wave activity (eddy terms) (Andrews *et al.*, 1987). For a time mean the negative wave forcing (westward) from the breaking planetary scale Rossby waves must be balanced by the latitudinal component of the residual mean meridional circulation. Therefore from (5.2) \bar{v}^* must be positive (if f_0 is positive). Hence air is driven poleward (towards the Earth's axis of rotation), crossing angular momentum contours and thus reducing the angular momentum of the zonal flow. This poleward mass transport results in upwelling in the tropics and downwelling at the poles due to mass continuity. Therefore the Brewer-Dobson circulation is a wave driven circulation (Haynes *et al.*, 1991).

A tropical pipe model of stratospheric transport was presented by Plumb (1996). In this model the assumption is that there is a tropical region bounded by the subtropical edges of the northern and southern hemisphere wintertime surf zones (i.e. the surf zones do not overlap) which is isolated from the vigorous isentropic mixing of the midlatitude surf zones. In reality the edge of the tropical pipe will only be well defined in one hemisphere at a time. This is because in summer there is no stratospheric surf zone as there is little or no mixing taking place (Waugh, 1996) and therefore there is no tropical pipe edge in the summer

subtropics. The edge of the tropical pipe is formed when mixing in the surf zone steepens potential vorticity gradients in the subtropics. It is these strong potential vorticity gradients that are barriers to mixing. The mean vertical motion inside the tropical pipe is upward and the edges of the pipe (typically around 20° latitude) act as barriers to transport. From examining observed tracer-tracer relationships in the tropics Plumb (1996) and Volk *et al.* (1996) found that they were different to relationships observed in the surf zone. From this they inferred that the edges of the tropical pipe act as barriers to transport. However, these are not perfect barriers to transport but are somewhat leaky (Plumb, 1996) especially in the lower stratosphere where turbulence in the surf zone can entrain material from the tropical pipe into the northern and southern hemisphere wintertime surf zones, leading to quasi-horizontal mixing.

Neu & Plumb (1999) extended the tropical pipe model (Plumb, 1996) to a leaky pipe model of the stratosphere. Their model differs from the original tropical pipe model in that it allows extratropical air to be mixed into the tropics as well as tropical air to be mixed into the surf zone (only the latter was part of the original tropical pipe model). The reason the leaky pipe model includes mixing into the tropics (also referred to as in-mixing) is that several studies, such as Volk *et al.* (1996), demonstrated that a certain amount of air in the tropics (approximately 45%) had come from the extratropics. Mixing into the tropical pipe has significant implications for tracer concentrations within the stratosphere. Air that is mixed out of the pipe does not change the tracer concentrations within the pipe; air that is mixed in from the surf zone on the other hand will have a different chemical composition and will therefore alter the tracer concentrations in the tropical pipe. This in-mixing will affect the transport of ozone and water vapour into the stratosphere, with subsequent consequences for the chemical processes they are involved in. This leaky pipe model has recently been used by Ray *et al.* (2010) to investigate variability in the strength of the Brewer-Dobson

circulation and in-mixing into the tropics in order to try to explain the decrease in stratospheric age of air observed over the past few decades. Ray *et al.* (2010) found that the tropical tape recorder signal of water vapour (Mote *et al.*, 1996) is significantly influenced by lateral mixing into the tropics and that this in-mixing plays a key role in the observations of stratospheric age of air and ozone. They presented evidence that an increase in in-mixing will either entirely or partly counteract the decreases in the mean age of air due to a strengthened mean circulation.

In this chapter we investigate mixing and lateral transport in the stratosphere. We examine the vertical structure of potential vorticity, a fundamental dynamical quantity, since strong potential vorticity gradients are barriers to mixing. The hypothesis is that the potential vorticity structure associated with a particular phase of the quasi-biennial oscillation (hereafter QBO) may affect mixing and transport in the stratosphere. To quantify mixing and transport we analyse Lagrangian trajectories of particles advected by winds in different meteorological conditions. The model used is an online trajectory model and is described in chapter 4. The main features of the QBO are described in section 5.2.1 followed by an examination of the effect of the QBO phase on the potential vorticity structure and a discussion of how we expect the potential vorticity structure to influence horizontal transport in section 5.2.2. The experiment design is presented in section 5.2.3. In section 5.3 we analyse the results of the trajectory calculations focusing on the difference between QBO phases. A brief discussion is given in section 5.4.

5.2 The Effect of the Phase of the QBO on the Potential Vorticity Structure

5.2.1 The QBO

The QBO is an oscillation in the mean zonal winds of the equatorial stratosphere between easterly (westward) and westerly (eastward) (Baldwin *et al.*, 2001). This alternating mean zonal wind pattern has an average period of about 28 months. A notable feature of this oscillation is that the eastward shear zones (where eastward winds increase with height) propagate downward more regularly and rapidly than the westward shear zones. Also this oscillation descends from 10 to 40hPa without loss of amplitude. Another feature of the QBO is that zonally symmetric eastward winds occur at the equator.

The QBO is thought to be driven by various vertically propagating equatorial waves (such as Rossby-gravity waves and Kelvin waves) (Lindzen, 1968; Holton & Lindzen, 1972). The oscillation then arises from a mechanism described by Lindzen (1968) as involving a two-way feedback between the waves and the background flow (momentum transport). Experimental models of the QBO by Plumb & McEwan (1978) support the wave driven theory of the QBO. Their laboratory experiment consisted of an annulus of salt-stratified fluid with an oscillating lower boundary that forced vertically propagating gravity waves. Plumb & McEwan (1978) found, for a sufficiently large forcing amplitude, a mean flow that exhibited the main characteristics described by the theoretical models of the QBO.

Mixing within the surf zone can be regarded as mixing within a Rossby wave critical layer. Planetary scale Rossby waves are approximately stationary, *i.e.* zero phase speed (whole spectrum of Rossby waves: the dominant power is the stationary waves) and therefore their critical layers occur when the zonal flow is stationary, *i.e.* a zero wind line. The phase of the QBO affects the location of

the extratropical surf zone by moving the zero wind line. The QBO is therefore expected to have a strong influence on mixing and transport. Holton & Tan (1980) demonstrated the influence of the QBO on the stratospheric circulation at 50 hPa. They understood that the dependence of the location of the zero wind line on the QBO phase would change the latitude where the momentum forcing due to Rossby wave breaking occurs and allow lateral motion across angular momentum surfaces. Dunkerton & O’Sullivan (1996) observed a region of lateral mixing (critical layer) in the tropical stratosphere above 10hPa, equatorward of the subtropical jet. This tropical mixing zone is separated from the vigorous mixing of the extratropical surf zone by the subtropical jet at most longitudes except east Asia and the west Pacific. They demonstrated that whether or not this tropical mixing occurs is dependent on the phase of the QBO. More recently, Shuckburgh *et al.* (2001) used an equivalent length diagnostic to quantify transport and mixing in the lower and middle stratosphere. They found that when the QBO phase was easterly that there was weak mixing in the tropics and subtropics. During a westerly QBO phase they found that the strong mixing of the surf zone extended to very low latitudes in the northern hemisphere subjecting tropical air to vigorous mixing. Therefore understanding the QBO is essential for studying tracer transport within the stratosphere.

5.2.2 Potential Vorticity Structure

The work of Shuckburgh *et al.* (2001) applies a kinematic description of the flow (based on the winds) to an investigation of the influence of the QBO on mixing and transport in the tropical and subtropical stratosphere. Here we adopt a more dynamical approach based on potential vorticity which evolves with the flow.

To investigate the effect of the QBO phase on the potential vorticity structure

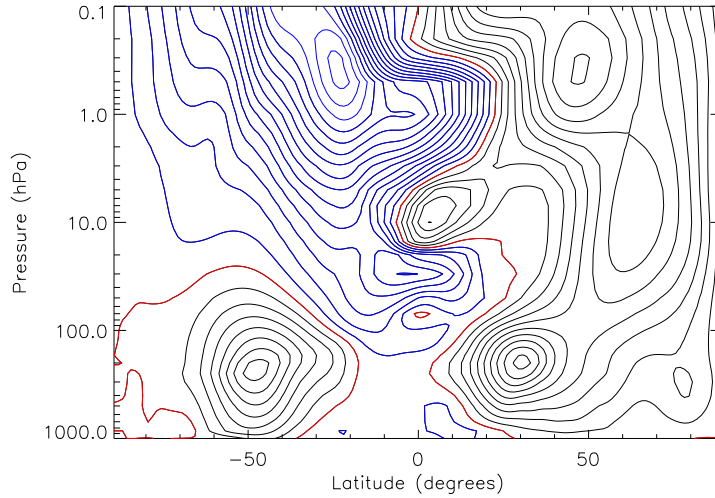


Figure 5.1: Zonal mean of the longitudinal component of velocity on the 1st January 1997. The red line represents the zero wind line, black contours represent positive winds (i.e. Westerlies) and blue contours represent negative winds (i.e. Easterlies). Contour interval is 5ms^{-1} .

in the stratosphere we firstly had to define the QBO phase. The QBO phase was defined as the predominant zonal mean longitudinal component of velocity at the equator between 70 and 20hPa (lower stratosphere). The zonal mean longitudinal component of velocity on the 1st of January 1997 is shown in Figure 5.1. The winds are predominantly easterly between 70 and 20hPa and therefore we define January 1997 as being in an easterly phase of the QBO. In comparison, Figure 5.2 shows the zonal wind profile on the 1st of January 1998 in which the winds are predominantly westerly in the lower stratosphere. Thus we define January 1998 as being in a westerly QBO phase.

We first consider the influence of the QBO phase on the height-latitude structure of potential vorticity. Following Lait (1994) we calculate the modified potential vorticity (Π) from Ertel's potential vorticity (EPV, see (1.5))

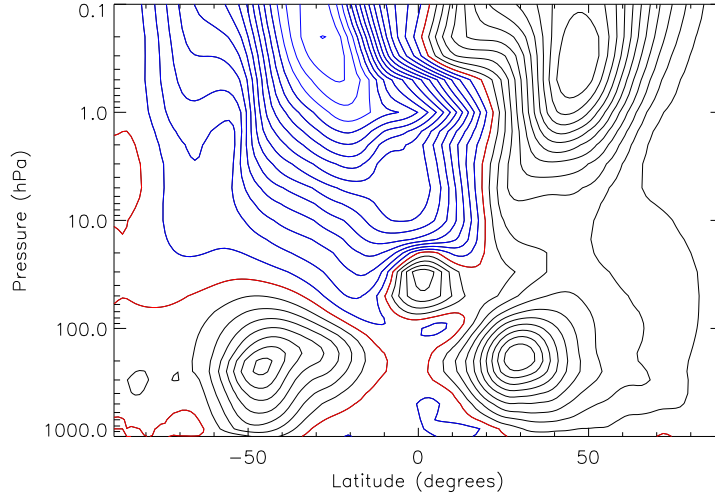


Figure 5.2: Zonal mean of the longitudinal component of velocity on the 1st January 1998. The red line represents the zero wind line, black contours represent positive winds (i.e. Westerlies) and blue contours represent negative winds (i.e. Easterlies). Contour interval is 5ms^{-1} .

$$\Pi = EPV \left(\frac{\theta}{\theta_0} \right)^{-\frac{9}{2}} \quad (5.3)$$

where θ is the potential temperature and $\theta_0 = 420\text{K}$ is a reference potential temperature. This removes the exponential vertical dependence of the potential vorticity enabling us to view its structure in the vertical. The meridional potential vorticity field (compare Figure 5.3 and Figure 5.4) is significantly different between the two phases of the QBO. For the years defined as being in an easterly phase of the QBO there are sharp potential vorticity gradients at the equator around 70hPa and 10hPa with strong gradients at 20°N and 20°S between these two pressure levels. In contrast a westerly QBO phase has very sharp potential vorticity gradients at the equator up to about 20hPa. Above 20hPa there are strong potential vorticity gradients in the northern hemisphere subtropics. These potential vorticity gradients are consistent with the zonal wind fields described

above (through potential vorticity inversion: $q \sim \mathbf{k} \cdot \nabla \times \mathbf{u}$).

In order to better understand these differences in the vertical structure of the potential vorticity we investigate its structure on several isentropic surfaces. We non dimensionalise the potential vorticity following Polvani & Saravanan (2000). This allows us to use an objective contour interval so that on all isentropic surfaces we capture the predominant features of the potential vorticity structure. The modified potential vorticity on each isentropic surface is non dimensionalised by dividing it by

$$\frac{g\kappa f}{p_0 T_0^{1/\kappa}} \theta_0^{\kappa+1/\kappa} \quad (5.4)$$

where $\kappa = 2/7$, $g = 9.80665$, $p_0 = 1000\text{hPa}$, $T_0 = 240\text{K}$, $\theta_0 = 420\text{K}$ and $f = 2\Omega$ which is the polar Coriolis parameter where Ω is the Earth's rotation rate. The expression in (5.4) has dimensions of potential vorticity ($\text{Km}^2\text{s}^{-1}\text{kg}^{-1}$). The structure of the potential vorticity on the isentropic surface $\theta = 580\text{K}$ is shown in Figure 5.5(a) for the 1st of January 1997 (at the equator $\theta = 580\text{K}$ corresponds approximately to 30hPa). Note that these figures seem to be typical for January (main feature of the potential vorticity structure did not change significantly over the month). Thermal forcing is fairly constant over winter and therefore we expect there to be little change in the large-scale potential vorticity structure over January. Of course if a stratospheric sudden warming occurs there may be more significant changes to the large-scale potential vorticity structure. We would also expect differences to occur with changes in season. At $\theta = 580\text{K}$ (30hPa) the zonal winds at the equator are easterly and Figure 5.5(a) shows that there are two regions of strong potential vorticity gradients, one around 20°N and 20°S corresponding to the edge of the tropical pipe, the other around 60°N at the edge of the polar vortex.

A useful way of summarising this structure is to define the equivalent latitude

of the potential vorticity field (Butchart & Remsberg, 1986). The equivalent latitude is defined as

$$\phi_e = \sin^{-1} \left(1 - \frac{A}{2\pi a^2} \right) \quad (5.5)$$

where A is the area in which the potential vorticity is greater than or equal to q (a particular potential vorticity value) on a given isentropic surface, and a is the radius of the Earth. The equivalent latitude is the latitude circle (centered at the pole) that encloses the same area, A . The fact that potential vorticity is monotonic from pole to pole allows it to be used to define ϕ_e . Figure 5.5(b) displays the potential vorticity on the surface $\theta = 580\text{K}$ as a function of equivalent latitude. There are regions of strong potential vorticity gradients around 20°N and 20°S indicating the presence of barriers to mixing. These strong potential vorticity gradients represent the edges of the tropical pipe as discussed earlier. At higher altitudes on the isentropic surface $\theta = 860\text{K}$ (at the equator $\theta = 860\text{K}$ corresponds approximately to 10hPa) the zonal winds at the equator are westerly and the potential vorticity structure on this isentropic surface is significantly different to that on $\theta = 580\text{K}$ (see Figure 5.6(a)). Instead of strong potential vorticity gradients in the subtropics there are strong potential vorticity gradients at the equator (corresponding to a westerly jet). A cat's eye structure can be seen in the extratropics indicating critical layer mixing. The strong potential vorticity gradients at the equator are demonstrated further by the potential vorticity staircase in Figure 5.6(b) where there is a steep gradient in potential vorticity at the equator.

Figures 5.7 and 5.8 show the same isentropic surfaces as Figures 5.5 and 5.6 respectively but for January 1998. The difference here is that the zonal winds at the equator are westerly at $\theta = 580\text{K}$ and easterly at $\theta = 860\text{K}$ (i.e. the opposite of January 1997). There is a clear correlation between the sign of the zonal winds at the equator on a given level and the structure of the potential

vorticity on that same level. At levels where the equatorial winds are easterly there are strong potential vorticity gradients in the subtropics. At levels where the equatorial winds are westerly there are strong potential vorticity gradients at the equator. As explained in section 5.1 strong gradients of potential vorticity act as barriers to mixing and transport and they form at the edges of critical layers. We therefore conjecture that when the equatorial winds are easterly the majority of particles will remain in the tropics and there will be little mixing from midlatitudes into the tropics. This suggests that the subtropical barrier is limiting mixing in the northern hemisphere. However when the equatorial winds are westerly we expect the strong potential vorticity gradients at the equator to isolate the southern hemisphere from mixing. We also hypothesise that the strong equatorial potential vorticity gradients will enable particles to mix to the equator and that particles in the tropics will be mixed out across the northern hemisphere creating a wide critical layer (see Figures 5.9 and 5.10 for schematics of our hypothesis). These assumptions are consistent with the work of Shuckburgh *et al.* (2001) who found that in a westerly phase of the QBO mixing is enhanced in the subtropics (we conjecture that mixing is enhanced to the equator) and in an easterly phase mixing is inhibited in the tropics. It is important to note that the edge of the tropical pipe is only well defined in terms of potential vorticity gradients on levels where the zonal winds are easterly. On levels where the zonal winds are westerly there are no strong potential vorticity gradients in the subtropics. Therefore the edge of the tropical pipe may not be well defined there. Finally the potential vorticity gradients are stronger in the northern hemisphere, consistent with vigorous mixing occurring in the surf zone.

5.2.3 Experiment Design

To test our hypothesis we examine mixing and lateral transport in the winter stratosphere. More specifically we begin with Januarys in either an easterly or

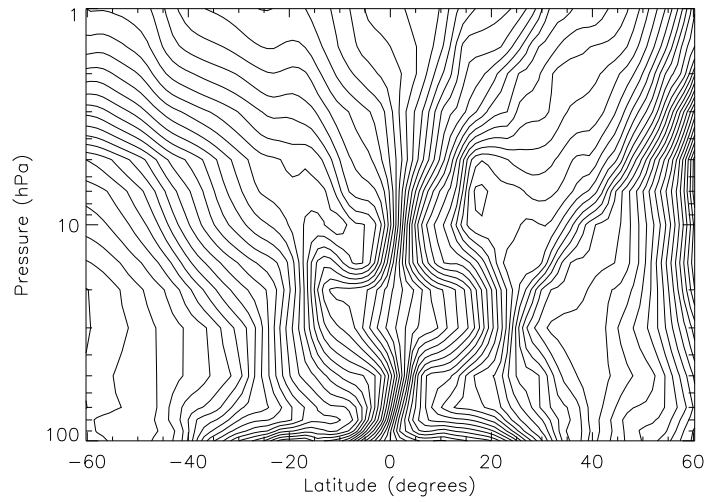


Figure 5.3: Zonal mean potential vorticity, with the vertical dependence removed, on the 1st January 1997. Contour interval is $5 \times 10^{-7} \text{K m}^2 \text{s}^{-1} \text{kg}^{-1}$. Easterly QBO.

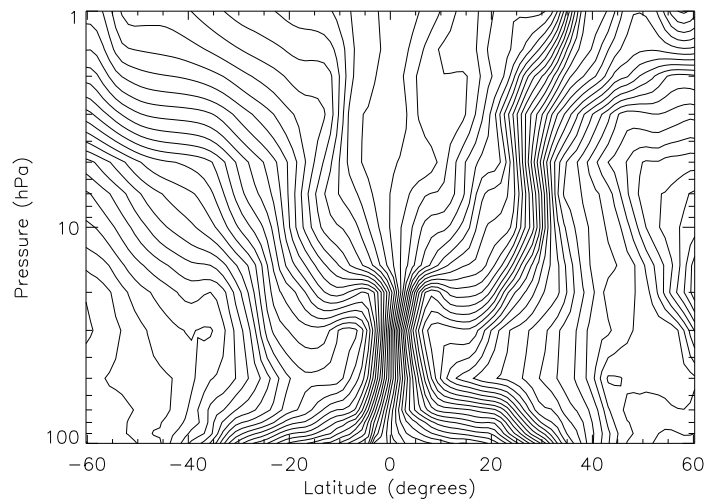


Figure 5.4: Zonal mean potential vorticity, with the vertical dependence removed, on the 1st of January 1998. Contour interval is $5 \times 10^{-7} \text{K m}^2 \text{s}^{-1} \text{kg}^{-1}$. Westerly QBO.

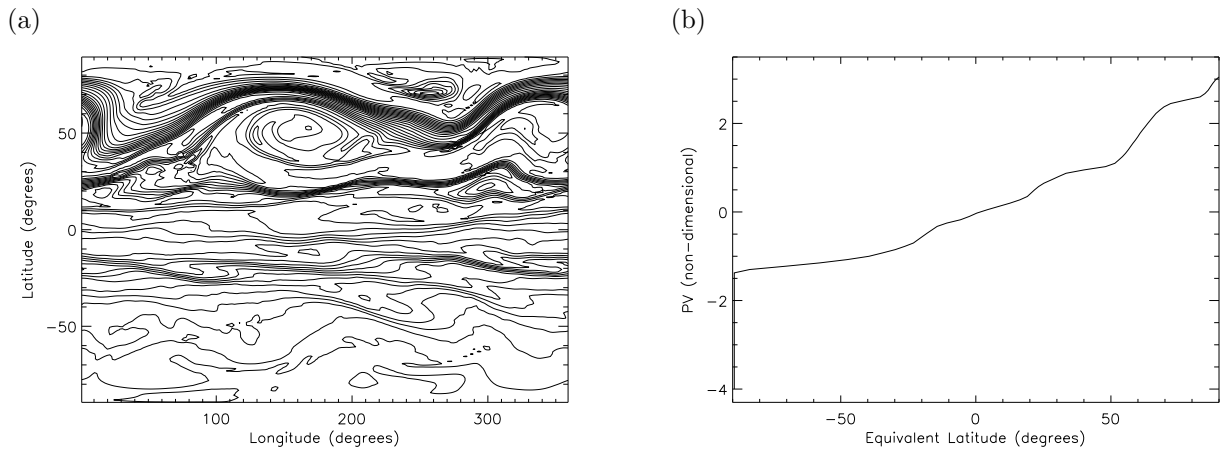


Figure 5.5: (a) Potential vorticity on $\theta=580\text{K}$ surface on the 1st of January 1997. Contour interval is 0.075 (non dimensional PV). (b) Potential vorticity on $\theta=580\text{K}$ surface on the 1st of January 1997 as a function of equivalent latitude.

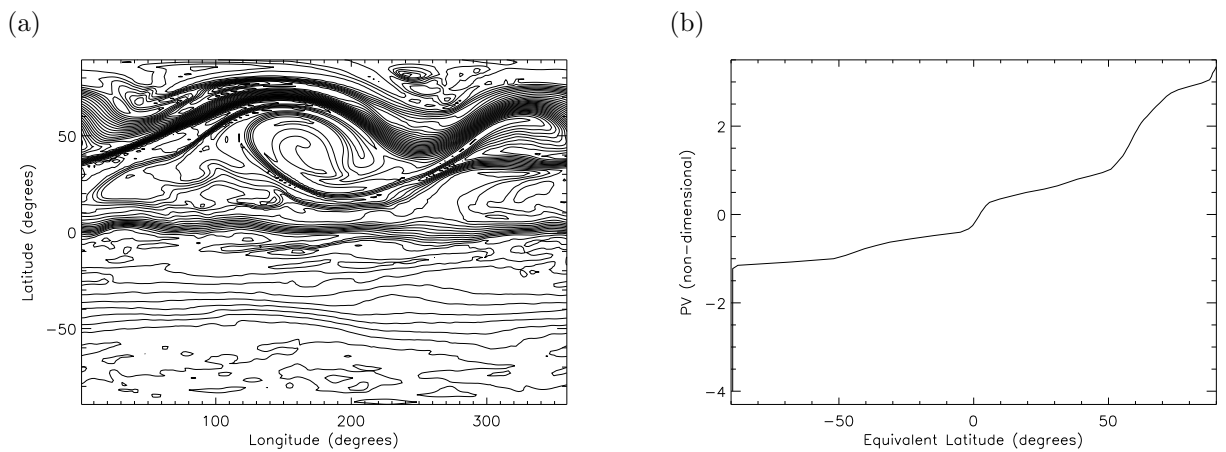


Figure 5.6: (a) Potential vorticity on $\theta=860\text{K}$ surface on the 1st of January 1997. Contour interval is 0.075 (non dimensional PV). (b) Potential vorticity on $\theta=860\text{K}$ surface on the 1st of January 1997 as a function of equivalent latitude.

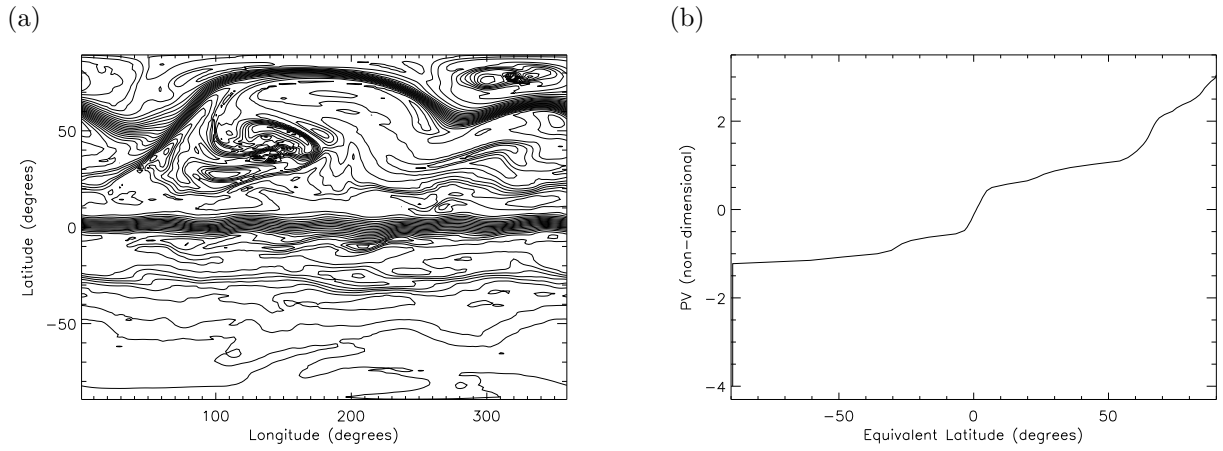


Figure 5.7: (a) Potential vorticity on $\theta=580\text{K}$ surface on the 1st of January 1998. Contour interval is 0.075 (non dimensional PV). (b) Potential vorticity on $\theta=580\text{K}$ surface on the 1st of January 1998 as a function of equivalent latitude.

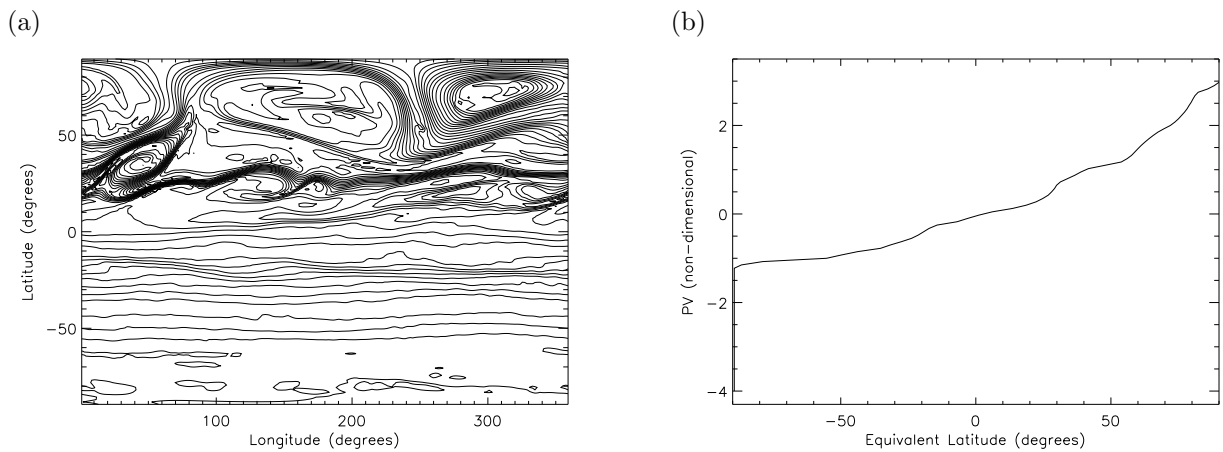


Figure 5.8: (a) Potential vorticity on $\theta=860\text{K}$ surface on the 1st of January 1998. Contour interval is 0.075 (non dimensional PV). (b) Potential vorticity on $\theta=860\text{K}$ surface on the 1st of January 1998 as a function of equivalent latitude.

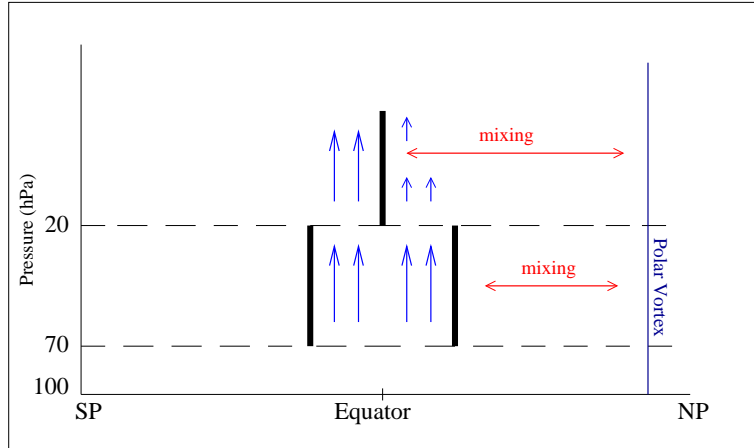


Figure 5.9: Schematic of our hypothesis for our definition of Easterly QBO January's.

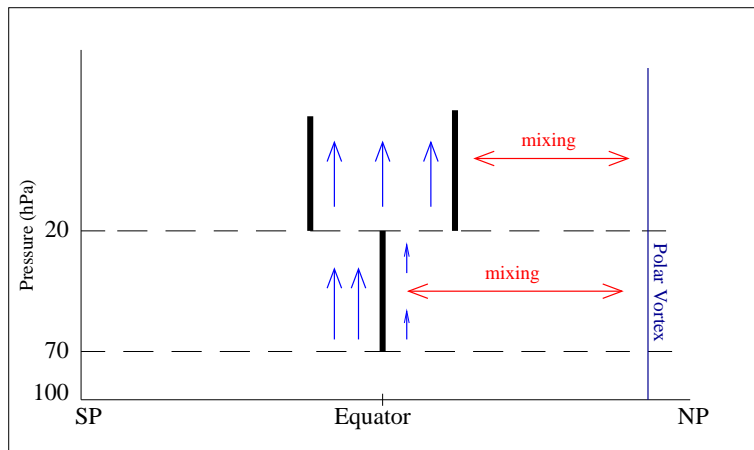


Figure 5.10: Schematic of our hypothesis for our definition of Westerly QBO January's.

westerly phase of the QBO. To reduce the effects of large interannual variability the three most extreme Januarys in each QBO phase between the years 1979 and 1998 were selected. This gave January 1983, 1989 and 1997 as the three easterly QBO winters and January 1984, 1995 and 1998 as the three westerly QBO winters. Strong easterly or westerly QBO phases represent extreme conditions within the tropics.

The model used is the “online” trajectory model described in chapter 4. The Lagrangian particles are initialised on ten vertical levels in the stratosphere, namely 150, 100, 70, 50, 30, 20, 15, 10, 7 and 5 hPa. On each vertical level the particles are initially distributed so that the area between two adjacent particles on one latitude and the two adjacent particles on the adjacent latitude is approximately equal. The particles are spaced every 1.25° in latitude from 88.75°N to 88.75°S . At the equator particles are spaced every 1.875° in longitude. The number of particles on each latitude circle then decreases towards the poles in order to conserve the area between them. This results in 17,600 particles on each vertical level and therefore there are 176,000 particles in total. The particles are initialised on the 1st of January for each of the six January’s studied. They are advected until the 10th of February and, as section 5.3 will demonstrate, forty days is sufficient to capture significant mixing and transport in the wintertime stratosphere. Temperature, water vapour and potential vorticity are assigned as attributes to the particles (see chapter 4). Potential vorticity as an attribute is particularly important as it will allow us to know where particles are in relation to the potential vorticity field of the flow at any given time. Since potential vorticity is materially conserved for a conservative flow, changes in the trajectory potential vorticity represent the effects of non-conservative processes (e.g. dissipation from small-scale mixing).

5.3 Analysis of Trajectories

In this section we analyse the trajectories of Lagrangian particles with a specific focus on the differences between QBO phases. We follow particles that are initially on levels where the equatorial zonal winds are easterly or westerly. Figure 5.11 displays the levels of particular focus in this analysis which are 30hPa and 10hPa. In the easterly QBO winters the equatorial zonal winds are easterly at 30hPa and westerly at 10hPa. The opposite is true for the westerly QBO winters. Note that at the equator 30hPa corresponds closely to the $\theta = 580K$ isentropic surface (see Figures 5.5 and 5.7 for the potential vorticity structure on this surface) and 10hPa corresponds closely to the $\theta = 860K$ isentropic surface (see Figures 5.6 and 5.8). To examine mixing and transport out of the tropics (and thus test our hypothesis) we chose to divide the tropics into equivalent latitude intervals that were fractions of a subtropical equivalent latitude, denoted by ϕ_p . At levels where the equatorial zonal winds are easterly ϕ_p is taken to be the equivalent latitude of the strongest potential vorticity gradient in the subtropics (ϕ_p varies from 19.4° to 29.1°). However at levels where the equatorial zonal winds are westerly there are no strong potential vorticity gradients in the subtropics and therefore $\phi_p = 23^\circ$ is chosen as a suitable subtropical latitude. We then follow particles that initially have an equivalent latitude, ϕ_e , within intervals of $\frac{1}{4}\phi_p$ (e.g. $\frac{3}{4}\phi_p \leq \phi_e \leq \phi_p$, $\frac{1}{2}\phi_p \leq \phi_e \leq \frac{3}{4}\phi_p$ etc.) and then count how many of those particles have an equivalent latitude greater than ϕ_p at some later time T. To determine the equivalent latitude of the particles at time, T, we compare the potential vorticity of the particle (potential vorticity attribute) with the potential vorticity of the flow. In order to make this comparison we must compare the same form of potential vorticity. In terms of the flow we know the non-dimensional potential vorticity on isentropic surfaces (see section 5.2.2) and can therefore determine the non-dimensional potential vorticity associated with each equivalent latitude of interest, for example ϕ_p , $\frac{3}{4}\phi_p$, $\frac{1}{2}\phi_p$ etc. (see Figures 5.5

to 5.8). Using the expression in (5.4) we calculate the modified potential vorticity associated with each equivalent latitude. We also convert the potential vorticity attributed to each particle into modified potential vorticity (5.3) and therefore we know where the particle is in relation to a given equivalent latitude. Note that the modified potential vorticity removes the exponential vertical dependence of potential vorticity allowing us to determine the particles positions with respect to specific equivalent latitudes independent of their movement in the vertical.

The percentage of particles that have moved outside the tropics by day 5, 10, 20 and 40 of the trajectory calculation (averaged over the three winters in that QBO phase) are displayed in Tables 5.1 to 5.4. Each table contains the values for particles initially on a given pressure level (either 30hPa or 10hPa) and for a given winter defined to be in an easterly or westerly QBO phase (January 1997 & 1998). Comparing Tables 5.1 and 5.2 for the easterly QBO winters demonstrates that there is greater mixing out of the tropics at higher altitudes (10hPa), where the equatorial zonal winds are westerly, than at lower altitudes (30hPa), where the winds are easterly. This agrees with our hypothesis (Figure 5.9) as the strong subtropical gradients of potential vorticity at 30hPa apparently inhibit transport out of the tropics. Table 5.1 suggests that particles have to be well within the tropics, say $\frac{1}{4}\phi_p \leq \phi_e \leq \frac{1}{2}\phi_p$, on levels where the equatorial zonal winds are easterly before transport is reduced significantly by the strong potential vorticity gradients in the subtropics. This may be because particles initially with an equivalent latitude greater than $\frac{1}{2}\phi_p$ are within the band of strong potential vorticity gradients in the subtropics and are therefore not equatorward of the barrier to mixing and transport. Hence they are more easily mixed out of the tropics.

Figure 5.12(a) shows the particles initially on 30hPa at $\frac{1}{4}\phi_p \leq \phi_e \leq \frac{1}{2}\phi_p$ on the 1st January 1997 and then their positions at $T = 40$ days are shown in Figure 5.12(b). Note that the black contour in these figures and the subsequent trajectory figures is the modified potential vorticity contour with an equivalent

latitude ϕ_p at time T . At $T = 40$ days it is clear that some particles have been mixed out of the tropics and have started to descend. Also the particles that have remained in the tropics have mixed across tropical latitudes. This is more evident in Figure 5.13 which is the same as Figure 5.12 except that the particles are initially between the equator and $\frac{1}{4}\phi_p$. Contrasting Figures 5.13(a) and (b) it is evident that in this case particles are being mixed across the tropics with some being transported southward of the equator.

In contrast to Figure 5.12, Figure 5.14 shows particles initially between $\frac{1}{4}\phi_p$ and $\frac{1}{2}\phi_p$ on 10hPa where the equatorial zonal winds are westerly rather than on 30hPa (easterly QBO phase). In Figure 5.14(b) particles that have been transported out of the tropics have been mixed right across the northern hemisphere. The movement of particles initially between the equator and $\frac{1}{4}\phi_p$ on 10hPa is shown in Figure 5.15. In this case the majority of particles remain at the equator (Figure 5.15(b)). On 10hPa, where the equatorial zonal winds are westerly, there are strong potential vorticity gradients at the equator which trap particles there. This implies that there is a barrier to mixing and transport at the equator on levels where the equatorial zonal winds are westerly. Also a comparison between pressure levels in Figures 5.13 and 5.15 shows a noticeable difference in the particles positions at $T = 40$ days which demonstrates the difference in transport between QBO phases.

A comparison of Tables 5.3 and 5.4 for the westerly QBO winters does not show a clear decrease in mixing between 30hPa and 10hPa as we would have expected from our hypothesis. There is a slight decrease in the percentage of particles transported to latitudes greater than ϕ_p at $T = 20$ days (from 39.6% on 30hPa to 32.2% on 10hPa) for particles initially between $\frac{1}{2}\phi_p$ and $\frac{3}{4}\phi_p$. However by $T = 40$ days the percentage of escaped particles is greater on 10hPa than on 30hPa for all initial positions of particles. Comparing Figures 5.16 and 5.18 at $T = 40$ days does not show a clear decrease in the amount of particles that

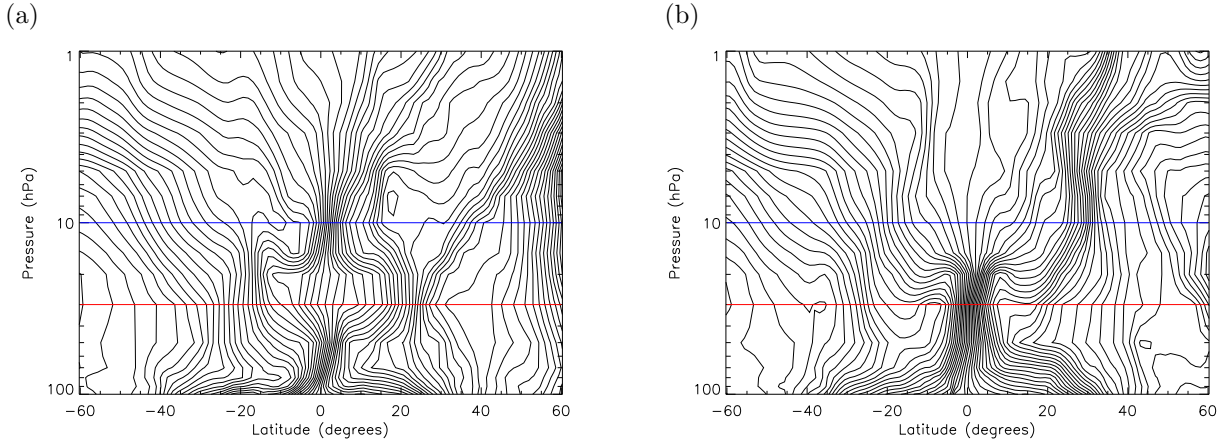


Figure 5.11: Zonal mean potential vorticity, with the vertical dependence removed, on the 1st of January (a) 1997 (Easterly QBO) and (b) 1998 (Westerly QBO). The blue line is at 10hPa and the red line is at 30hPa. Contour interval is $5 \times 10^{-7} \text{Km}^2 \text{s}^{-1} \text{kg}^{-1}$.

have been mixed out of the tropics between particles initially on 30hPa (westerly QBO winds) and on 10hPa (easterly QBO winds). It is interesting to note that in Figure 5.16(b) the particles have not reached the pole. Comparing this figure with Figure 5.7(a) the strong potential vorticity gradients which denote the edge of the polar vortex correspond to the most northerly edge of the particles in Figure 5.16(b). Although there is no clear decrease in mixing between 30hPa and 10hPa Figure 5.17 supports our hypothesis (and the results from the easterly QBO years) that particles on a level where the equatorial zonal winds are westerly are trapped by the strong potential vorticity gradients at the equator. On levels where the equatorial zonal winds are easterly there are no strong potential vorticity gradients at the equator and therefore there is mixing across the tropics as shown in Figure 5.19.

In the westerly QBO years the lack of a decrease in mixing between 30hPa (westerly winds) and 10hPa (easterly winds) could be due to a general increase in mixing with altitude. Averaging the percentage of particles that have mixed

Table 5.1: The Average Percentage of Particles with $\phi_e > \phi_p$ at Several Times for the Easterly QBO Years; particles initially at 30hPa (easterly equatorial winds).

Day	Particles Initial Positions				
	$\frac{3}{4}\phi_p \leq \phi_e \leq \phi_p$	$\frac{1}{2}\phi_p \leq \phi_e \leq \frac{3}{4}\phi_p$	$\frac{1}{4}\phi_p \leq \phi_e \leq \frac{1}{2}\phi_p$	$0^\circ \leq \phi_e \leq \frac{1}{4}\phi_p$	$-\frac{1}{4}\phi_p \leq \phi_e \leq 0^\circ$
5	19.8	4.4	0.2	0.0	0.0
10	30.8	10.6	0.4	0.0	0.0
20	40.4	19.6	2.1	1.1	0.3
40	62.4	39.4	22.3	11.7	2.3

Table 5.2: The Average Percentage of Particles with $\phi_e > \phi_p$ at Several Times for the Easterly QBO Years; particles initially at 10hPa (westerly equatorial winds).

Day	Particles Initial Positions				
	$\frac{3}{4}\phi_p \leq \phi_e \leq \phi_p$	$\frac{1}{2}\phi_p \leq \phi_e \leq \frac{3}{4}\phi_p$	$\frac{1}{4}\phi_p \leq \phi_e \leq \frac{1}{2}\phi_p$	$0^\circ \leq \phi_e \leq \frac{1}{4}\phi_p$	$-\frac{1}{4}\phi_p \leq \phi_e \leq 0^\circ$
5	28.9	6.4	1.4	0.0	0.0
10	41.7	18.7	4.2	0.1	0.0
20	57.9	39.6	16.9	0.9	0.0
40	73.3	49.4	26.3	1.0	0.0

out of the tropics for a given initial pressure level over all six years (not shown) demonstrates that there is indeed a weak increase in mixing with altitude. Therefore although in the westerly QBO years the QBO phase may inhibit mixing at high altitudes, this is apparently offset by the increase in mixing with altitude. In the easterly QBO years the increase in mixing with altitude from a level where the winds are easterly to a level where the winds are westerly will be accentuated by the QBO structure which will inhibit mixing at lower altitudes. Furthermore, although there is variability in the six years examined all the years demonstrate a weak dependence on mixing with altitude (possibly due to larger amplitude Rossby wave breaking at higher altitudes). In addition to a general increase in

Table 5.3: The Average Percentage of Particles with $\phi_e > \phi_p$ at Several Times for the Westerly QBO Years; particles at 30hPa (westerly equatorial winds).

Day	Particles Initial Positions				
	$\frac{3}{4}\phi_p \leq \phi_e \leq \phi_p$	$\frac{1}{2}\phi_p \leq \phi_e \leq \frac{3}{4}\phi_p$	$\frac{1}{4}\phi_p \leq \phi_e \leq \frac{1}{2}\phi_p$	$0^\circ \leq \phi_e \leq \frac{1}{4}\phi_p$	$-\frac{1}{4}\phi_p \leq \phi_e \leq 0^\circ$
5	31.6	7.8	2.0	0.0	0.0
10	40.8	19.2	5.4	0.0	0.0
20	50.9	39.6	9.6	0.0	0.0
40	62.4	55.0	25.3	1.2	0.0

Table 5.4: The Average Percentage of Particles with $\phi_e > \phi_p$ at Several Times for the Westerly QBO Years; particles initially at 10hPa (easterly equatorial winds).

Day	Particles Initial Positions				
	$\frac{3}{4}\phi_p \leq \phi_e \leq \phi_p$	$\frac{1}{2}\phi_p \leq \phi_e \leq \frac{3}{4}\phi_p$	$\frac{1}{4}\phi_p \leq \phi_e \leq \frac{1}{2}\phi_p$	$0^\circ \leq \phi_e \leq \frac{1}{4}\phi_p$	$-\frac{1}{4}\phi_p \leq \phi_e \leq 0^\circ$
5	25.4	6.3	2.4	0.8	0.0
10	40.5	15.4	5.2	1.9	0.0
20	52.1	32.2	15.7	10.5	1.0
40	68.2	57.1	34.3	18.6	2.8

mixing with altitude there is a dependence of the out-mixing on the time integration of the trajectory code. This is to be expected due to the chaotic nature of trajectories since in general particles will experience more mixing and transport over longer trajectories. Also as particles are initialised closer to the equator the percentage of particles escaping to latitudes greater than ϕ_p generally decreases and drops significantly between different bands of initial particles depending on whether the equatorial zonal winds are easterly or westerly.

Finally we compare the mixing and transport at 30hPa when the equatorial zonal winds are easterly (Table 5.1) and when they are westerly (Table 5.3). This comparison shows that up to $T = 20$ days the percentage of particles that

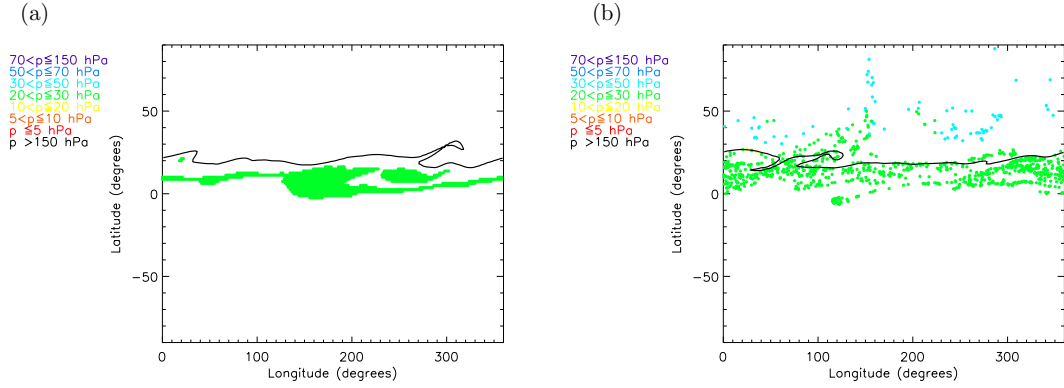


Figure 5.12: Particle positions at (a) $t = 0$ and (b) $t = 40$ days. Particles are initially on 30hPa at $\frac{1}{4}\phi_p \leq \phi_e \leq \frac{1}{2}\phi_p$ on the 1st January 1997. Note: Zonal winds at the equator are easterly on 30hPa.

are mixed out of the tropics when the winds are westerly is approximately double the percentage mixed out of the tropics when the winds are easterly. Making a similar comparison for particles initially on 10hPa (Tables 5.2 and 5.4) indicates a slight increase in mixing out of the tropics (at $T = 40$ days) when the equatorial zonal winds are easterly. This is counter to our expectations from our hypothesis which states that when the equatorial zonal winds are easterly the strong potential vorticity gradients in the subtropics limit mixing in the northern hemisphere. Is it possible that the fact that mixing increases with altitude is causing a comparison at this altitude to become less well defined? Considering only the levels where the equatorial zonal winds are easterly (Tables 5.1 and 5.4) reveals a significant increase in mixing out of the tropics at 10hPa over that at 30hPa. This suggests that the increase in mixing at higher altitudes may break or weaken the subtropical barrier by $T = 20$ days leading to a marked increase in mixing and transport out of the tropics. This therefore makes it difficult to compare mixing and transport between easterly and westerly QBO phases at high altitudes.

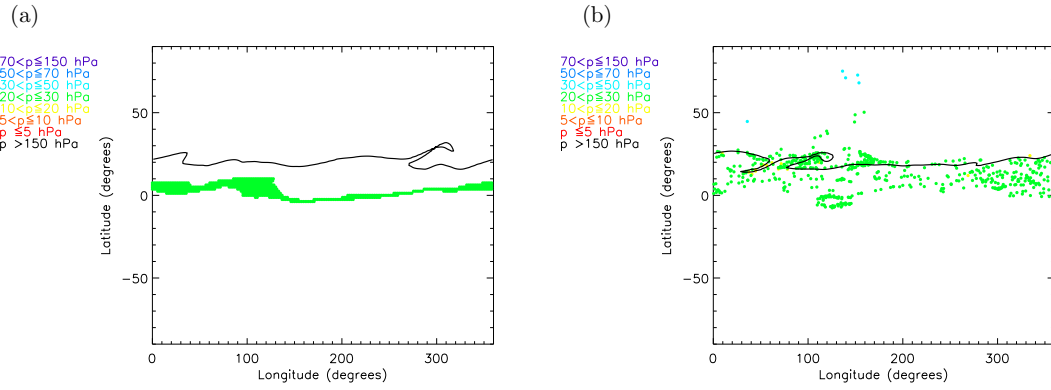


Figure 5.13: Particle positions at (a) $t = 0$ and (b) $t = 40$ days. Particles are initially on 30hPa at $0^\circ \leq \phi_e \leq \frac{1}{4}\phi_p$ on the 1st January 1997. Note: Zonal winds at the equator are easterly on 30hPa.

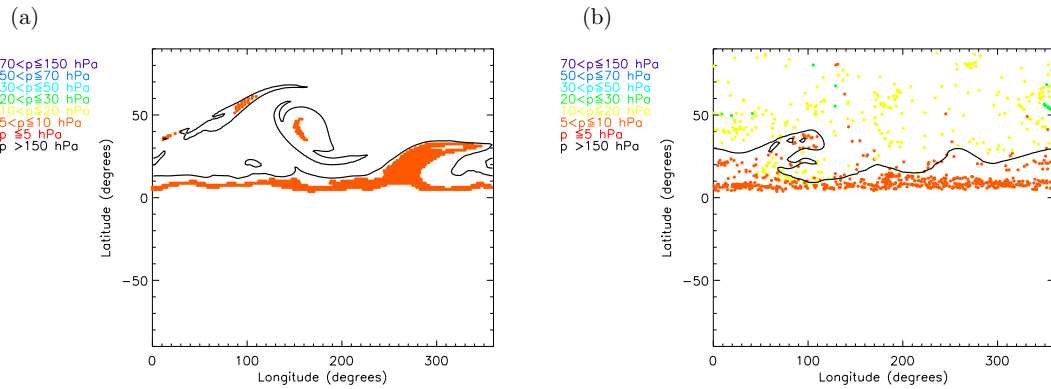


Figure 5.14: Particle positions at (a) $t = 0$ and (b) $t = 40$ days. Particles are initially on 10hPa at $\frac{1}{4}\phi_p \leq \phi_e \leq \frac{1}{2}\phi_p$ on the 1st January 1997. Note: Zonal winds at the equator are westerly on 10hPa.

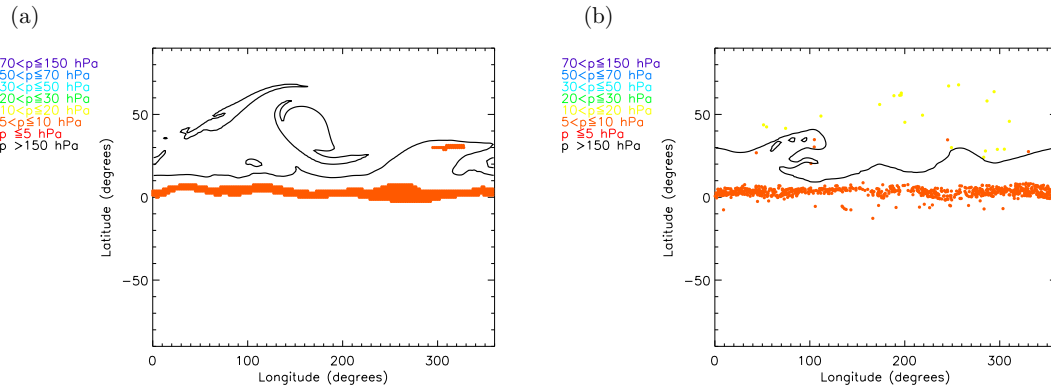


Figure 5.15: Particle positions at (a) $t = 0$ and (b) $t = 40$ days. Particles are initially on 10hPa at $0^\circ \leq \phi_e \leq \frac{1}{4}\phi_p$ on the 1st January 1997. Note: Zonal winds at the equator are westerly on 10hPa.

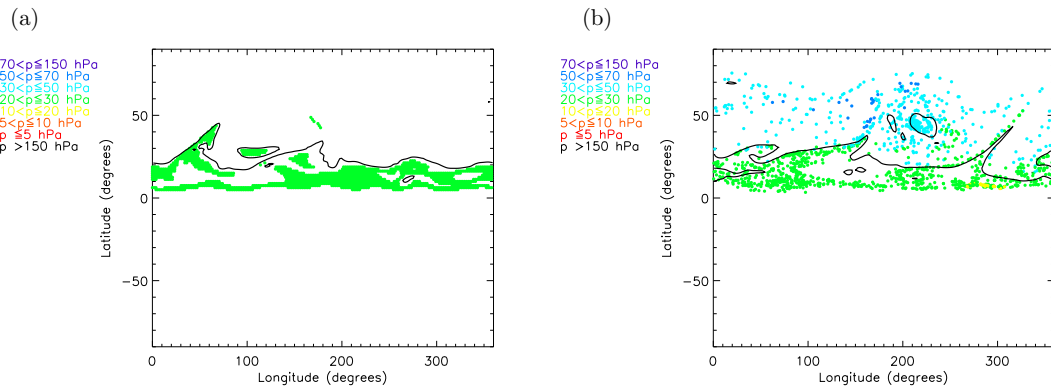


Figure 5.16: Particle positions at (a) $t = 0$ and (b) $t = 40$ days. Particles are initially on 30hPa at $\frac{1}{4}\phi_p \leq \phi_e \leq \frac{1}{2}\phi_p$ on the 1st January 1998. Note: Zonal winds at the equator are westerly on 30hPa.

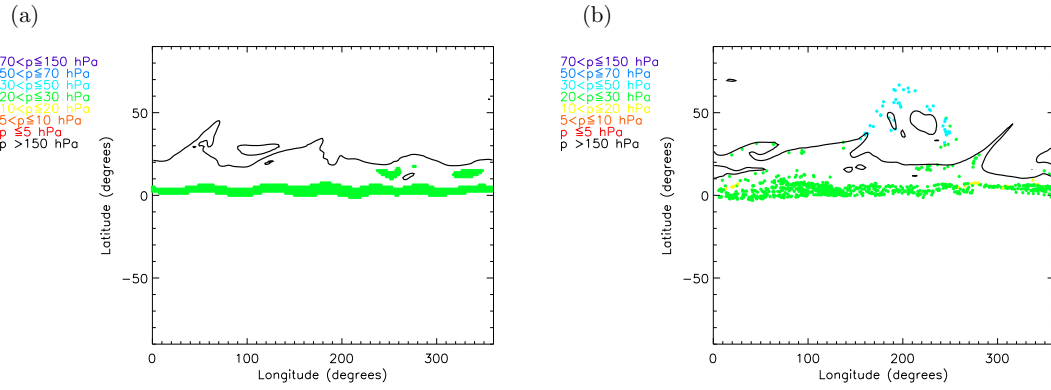


Figure 5.17: Particle positions at (a) $t = 0$ and (b) $t = 40$ days. Particles are initially on 30hPa at $0^\circ \leq \phi_e \leq \frac{1}{4}\phi_p$ on the 1st January 1998. Note: Zonal winds at the equator are westerly on 30hPa.

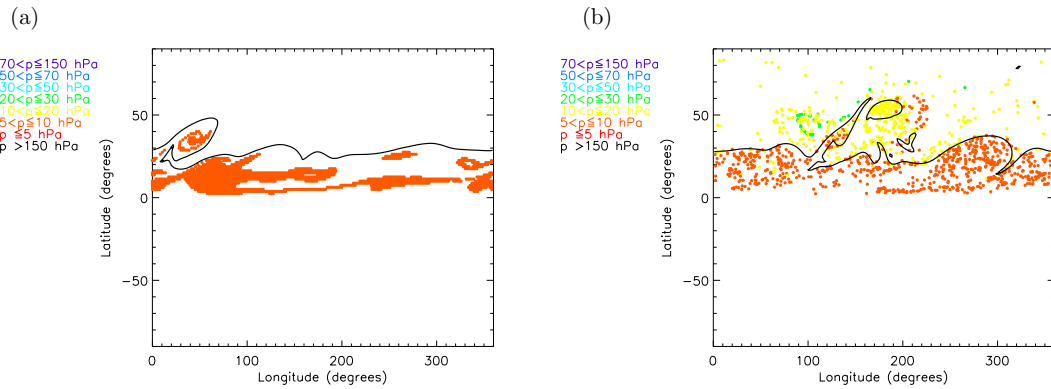


Figure 5.18: Particle positions at (a) $t = 0$ and (b) $t = 40$ days. Particles are initially on 10hPa at $\frac{1}{4}\phi_p \leq \phi_e \leq \frac{1}{2}\phi_p$ on the 1st January 1998. Note: Zonal winds at the equator are easterly at 10hPa.

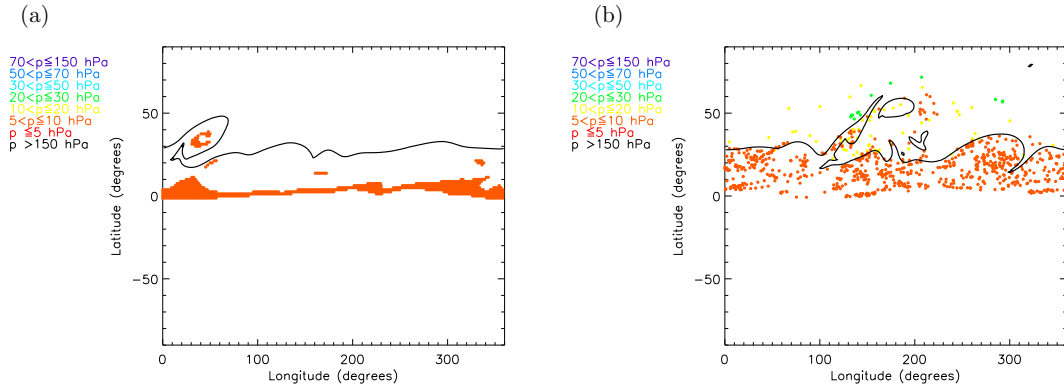


Figure 5.19: Particle positions at (a) $t = 0$ and (b) $t = 40$ days. Particles are initially on 10hPa at $0^\circ \leq \phi_e \leq \frac{1}{4}\phi_p$ on the 1st January 1998. Note: Zonal winds at the equator are easterly at 10hPa.

5.3.1 In-Mixing

The focus of this chapter has been on the effect of the QBO phase on lateral mixing and transport out of the tropics. However mixing from the surf zone into the tropics is also important as this changes tracer concentrations within the tropical pipe. Note that no such change in tracer concentrations occurs with out-mixing. It therefore has implications for the transport of chemicals such as ozone and water vapour in the stratosphere. To determine whether there is a difference in in-mixing with QBO phase we examine the movement of particles initially on 30hPa with an equivalent latitude greater than ϕ_p . This was carried out for both January 1997 (where the equatorial zonal winds are easterly) and January 1998 (where the equatorial zonal winds are westerly) (Figures 5.20 and 5.21). Note that the particles are initialised so that the area between them is conserved and hence there are less particles at the poles than at the equator and this is the reason for the pattern observed in Figures 5.20(a) and 5.21(a). The percentage of particles initially north of the tropics that are mixed into the tropics (for both January 1997 and 1998) are displayed in Table 5.5. In the case where the QBO phase is easterly there is not much difference in the percentage

of in-mixing over time and the percentage value is very small. This suggests that the strong potential vorticity gradients in the subtropics are stronger barriers to in-mixing than to mixing out of the tropics. Another contributor to this could be the vigorous mixing of the extratropical surf zone which entrains particles from the tropics. On the other hand when the QBO phase is westerly the percentage of particles mixed into the tropics increases with time to a maximum of 17.7% at $T = 40$ days. This again supports our hypothesis that the strong potential vorticity gradients at the equator on levels where the equatorial zonal winds are westerly enables mixing to occur from the equator to the polar vortex.

This analysis is simply an example of the effect of the QBO phase on mixing into the tropics. We leave further consideration of this topic for future work.

Table 5.5: The Percentage of Particles Initially Outside the Tropics on 30hPa that move into the Tropics after time t .

Day	January 1997 (Easterly)	January 1998 (Westerly)
5	3.0	5.3
10	3.2	6.8
20	4.4	11.1
40	2.7	17.7

5.4 Discussion

In this chapter we have investigated the effect of the QBO on transport and mixing in the stratosphere. We have shown that the phase of the QBO affects the structure of potential vorticity in the stratosphere. At levels where the QBO phase is westerly there are strong potential vorticity gradients at the equator which trap particles there, implying an equatorial barrier. Also these strong gradients enable mixing from between just north of the equator to the polar

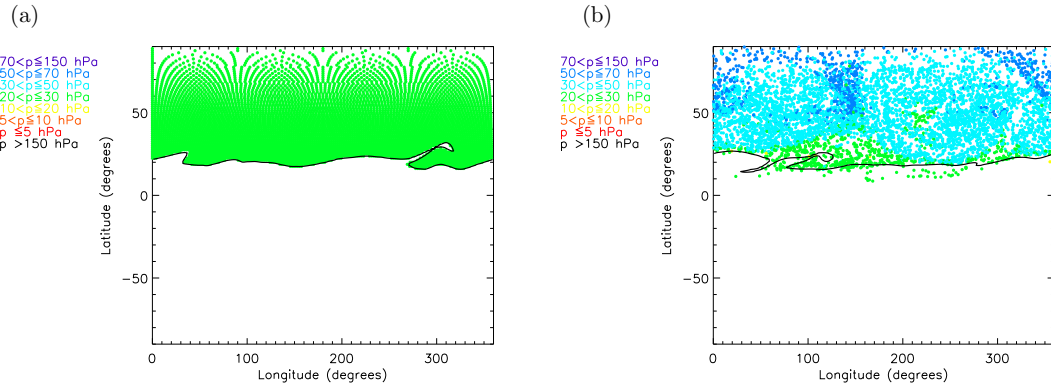


Figure 5.20: Particle positions at (a) $t = 0$ and (b) $t = 40$ days. Particles are initially on 30hPa at $\phi_e > \phi_p$ on the 1st January 1997. Note: Zonal winds at the equator are easterly at 30hPa.

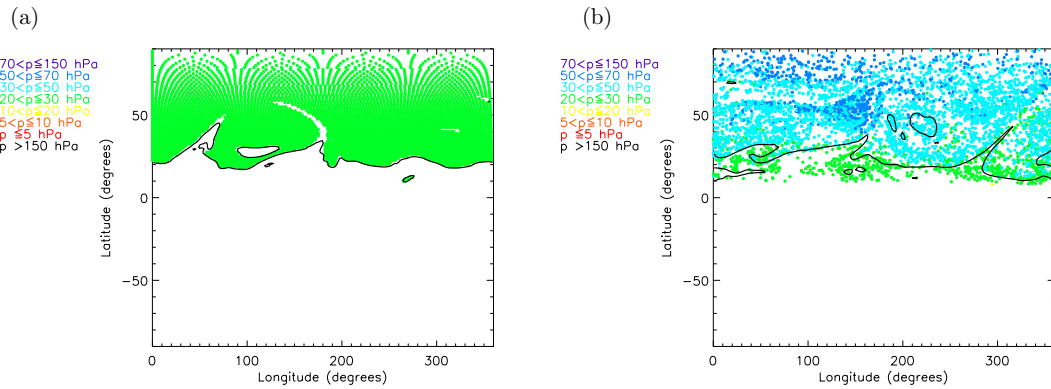


Figure 5.21: Particle positions at (a) $t = 0$ and (b) $t = 40$ days. Particles are initially on 30hPa at $\phi_e > \phi_p$ on the 1st January 1998. Note: Zonal winds at the equator are westerly at 30hPa.

vortex allowing particles from the extratropics to mix into the tropics. Conversely at levels where the QBO phase is easterly there are strong potential vorticity gradients in the subtropics. These potential vorticity gradients act as barriers to mixing, albeit weaker barriers than the potential vorticity gradients at the equator in the westerly QBO phase levels. These subtropical gradients limit the mixing region in the northern hemisphere to between the subtropics and the polar vortex. Also there is mixing across the tropics at the levels where the QBO phase is easterly. These results are consistent to those of Shuckburgh *et al.* (2001) who found that mixing is inhibited in the tropics during an easterly phase of the QBO and that during a westerly phase mixing is enhanced in the subtropics.

Following the work of Plumb (1996) the region above the tropical tropopause is referred to as the tropical pipe with the edges of the tropical pipe acting as barriers to mixing. From this investigation it appears that it may be more of a broken pipe. At the levels where the QBO phase is easterly the strong potential vorticity gradients in the subtropics can be regarded as the edges of the tropical pipe. However on levels where the equatorial zonal winds are westerly the strong potential vorticity gradients at the equator enable mixing from the equator to the pole and therefore the tropical pipe terminology is perhaps less applicable in this case.

In this chapter we have also considered the effect of the QBO phase on mixing and lateral transport into the tropics. We have demonstrated that significantly more in-mixing occurs when the equatorial zonal winds are westerly due to the strong potential vorticity gradients at the equator enabling mixing to occur from the equator to the polar vortex. When the QBO phase is easterly we found very little in-mixing into the tropics. This suggests that the strong potential vorticity gradients in the subtropics are strong barriers to in-mixing.

This analysis has allowed us to conjecture how the different QBO phases affect where the particles go in terms of ascent. In a westerly QBO year we expect more

particles to be mixed out towards the pole, where they begin to descend, than to ascend in the tropics to higher altitudes (weak upwelling). On the other hand in an easterly QBO year we expect more particles to remain in the tropics reaching higher altitudes (strong upwelling) at which point the winds are westerly and they will be transported towards the pole and begin to descend. The work of Punge *et al.* (2009), who considered the effect of the QBO on stratospheric transport at low latitudes using trajectory calculations from a general circulation model, supports this ascent conjecture. They found that upwelling in the tropics was enhanced when the equatorial winds were easterly and that this was reduced in a westerly QBO phase. This difference in ascent due to the dependence of lateral mixing on the QBO phase could have an influence on the ascent of chemicals such as ozone and water vapour and therefore affect the processes they are involved in in the stratosphere.

The phase of the QBO affects the lateral mixing and transport in the stratosphere. Understanding atmospheric transport and mixing is of particular importance to geoengineers who are considering injecting aerosols into the lower stratosphere to balance the effects of climate change. The affect of the QBO phase on mixing and transport in the stratosphere will play a vital role in this area of meteorology. This chapter has focused on mixing and transport out of the tropics. In future we could use this trajectory model to give further consideration to mixing into the tropics and the effect on chemical concentrations and transport in the stratosphere.

Chapter 6

Conclusions

The focus of this thesis has been an investigation of the transport and critical layer mixing in the troposphere and stratosphere. The understanding of this transport and mixing is important because it affects our weather and climate.

Chapter 1 summarised the structure of the atmosphere and the main dynamics that occur in the troposphere and stratosphere. Diagnostics to quantify mixing and transport were introduced such as Lyapunov exponents and effective diffusivity. A brief review of recent work involving effective diffusivity was given followed by an explanation of the calculation of this diagnostic.

In chapter 2 we investigated the evolution of a Rossby wave critical layer in an idealised model (channel model). Our work differed from that of SWW (1978) and Haynes (1989) in that we force the streamfunction in the critical layer directly. We examined the effect of the shear across the critical layer on the critical layer evolution, and more specifically on the development of barotropic instability in the critical layer. We found (consistent with Haynes (1989)) that barotropic instability occurred when the shear was suitably small, $\Lambda \leq 0.3$. We also considered how the mixing efficiency of the critical layer depended on the shear across the critical layer and used this dynamically consistent flow to compare different

measures of mixing (effective diffusivity and contour lengths). The mixing efficiency of the critical layer increased due to barotropic instability and effective diffusivity and contour lengths were found to be consistent measures of mixing. Barotropic instability was found to enhance mixing in the critical layer at early times when the shear was small. However this enhancement was much smaller than the enhancement of mixing due to the resonant growth of the critical layer around $\Lambda = \frac{1}{2}$.

In an extension to previous work a systematic investigation of the critical layer evolution at finite Rossby deformation length was carried out. This investigation was set up so that as far as possible everything was the same as the infinite Rossby deformation length investigation, *i.e.* topographic forcing and average shear in the critical layer region (same closed streamline pattern). We found that regardless of this the critical layer width increased at small L_D . This was due to the effect of L_D on the Rossby wave elasticity. We therefore chose to estimate the growth of the critical layer width with decreasing L_D . We discovered that at small L_D , L_D less than the natural wavelength of the instability, the wavelength of the instability reduces.

In chapter 3 we found that changes to the stratospheric potential vorticity have a significant impact on the development of baroclinic instability in an Eady-like model. The dependence is such that increasing the strength of the polar vortex tends to decrease the eddy growth in the troposphere. This is found not just in the zonally symmetric cases, comparing zonally symmetric stratospheric perturbations of different potential vorticity magnitudes, but also in cases of zonally asymmetric disturbances to a polar vortex of given potential vorticity. The latter scenario extends previous work that had considered only zonally symmetric stratospheric perturbations. In particular, we found that there is a large difference in the tropospheric evolution between cases representing a strong vortex and cases representing the vortex following either a wave-one or wave-two sud-

den warming. Differences in the tropospheric evolution include the growth of eddy kinetic energy and wave activity, as well as synoptic scale details of the wave breaking and the latitudinal extent of mixing within the troposphere. One of the important results of this work is that the potential vorticity perturbations made here result in significantly larger differences to the tropospheric evolution than obtained by perturbations to the stratospheric winds alone.

One significant difference between our results and those of Wittman *et al.* (2004, 2007) is the sense in which a stratospheric perturbation affects the growth of the instability. Wittman *et al.* found an increase in eddy growth rates with increasing stratospheric shear, whereas we find a decrease in growth rates with increasing stratospheric potential vorticity. The results are not inconsistent when full account is taken of changes to the tropospheric shear resulting from the stratospheric potential vorticity perturbation in our case, which tends to leave the vertical shear unchanged but increases the horizontal shear. The decrease in growth rates we observed may therefore be attributed to a change in the nature of the baroclinic development similar to that found by Thorncroft *et al.* (1993). One conclusion that may be drawn from both Wittman *et al.* and the present work is that the tropospheric evolution depends rather sensitively on the stratospheric state through details of the shear in the troposphere and near the subtropical jet.

Chapter 4 described a trajectory model, developed in conjunction with the UK Met Office, called the “online” trajectory code. This chapter gave a brief outline of the model followed by the results of some sensitivity experiments. This trajectory model is then used to study atmospheric transport and mixing in the stratosphere in more realistic situations.

In chapter 5 we investigated the effect of the QBO on transport and mixing in the stratosphere using the trajectory model described in chapter 4. We have shown that the phase of the QBO affects the structure of potential vorticity in the stratosphere. At levels where the QBO phase is westerly there are strong

potential vorticity gradients at the equator which trap particles there. Also these strong gradients enable mixing to occur from between just north of the equator to the polar vortex allowing particles from the extratropics to mix into the tropics. Conversely at levels where the QBO phase is easterly there are strong potential vorticity gradients in the subtropics. These potential vorticity gradients act as barriers to mixing, albeit weaker barriers than the potential vorticity gradients at the equator in the westerly QBO phase levels. These subtropical gradients limit the mixing region in the northern hemisphere to between the subtropics and the polar vortex.

We have considered everything in terms of potential vorticity and we have found that the phase of the QBO affects the potential vorticity structure. The waves that drive the QBO are predominantly Kelvin waves and don't have potential vorticity themselves. Consequently the effect on potential vorticity is not obvious. However they do have an effect on the mean flow and therefore the shear. In chapter 2 (using an idealised model) we examined the effect of the shear across a critical layer on the critical layer evolution. We found that the shear alters the efficiency of mixing in the critical layer and that as the shear reduces the critical layer width increases. Therefore if we consider the effect of the QBO on the horizontal shear the potential vorticity structure associated with a particular phase of the QBO could be the result of critical layer mixing where the critical layer width and the development of barotropic instability depend upon the shear. When the QBO phase is westerly the horizontal shear decreases (see Figure 5.2 - the shear at 20°N is weaker in the subtropics at the height of the westerlies than at the height of the easterlies) which results in an increase in the critical layer width and therefore allows transport to occur from the equator to the pole. This connection between these works highlights a link between the horizontal shear, the critical layer width and the extent of the particle mixing.

Following the work of Plumb (1996) the region above the tropical tropopause

is referred to as the tropical pipe with the edges of the tropical pipe acting as barrier to mixing. From this investigation it appears that it may be more of a broken pipe. At the levels where the QBO phase is easterly the strong potential vorticity gradients in the subtropics can be regarded as the edges of the tropical pipe. However on levels where the equatorial zonal winds are westerly the strong potential vorticity gradients at the equator enable mixing from the equator to the pole and therefore the tropical pipe terminology is perhaps less applicable in this case.

Finally we also considered the effect of the QBO phase on mixing and lateral transport into the tropics. We demonstrated that significantly more in-mixing occurs when the equatorial zonal winds are westerly due to the strong potential vorticity gradients at the equator enabling mixing to occur from the equator to the polar vortex. When the QBO phase is easterly we found very little in-mixing into the tropics. This suggests that the strong potential vorticity gradients in the subtropics are strong barriers to in-mixing. The affect of the QBO phase on lateral mixing and transport in the stratosphere is essential for understanding tracer transport in the atmosphere.

Chapter 7

Appendix: Online Trajectory Code

7.1 Where to Find the Online Code and How to Use It

The online trajectory code can be found at the UK Met Office in the directory `/project/strat_anl/traj_online`. The online trajectory code currently runs on version 7.3 of the Unified Model. To run the online trajectory code a branch of the Unified Model must be created and the following files committed to the branch (in the branches directory `/src/control/top_level`):

```
/project/strat_anl/traj_online/u_model.F90  
/project/strat_anl/traj_online/traj_mod.F90  
/project/strat_anl/traj_online/trajmain.F90  
/project/strat_anl/traj_online/traj_online.F90  
/project/strat_anl/traj_online/UMVARS.h  
/project/strat_anl/traj_online/TIMEV.h
```

/project/strat_anl/traj_online/RESPECTR.h
/project/strat_anl/traj_online/PATH.h
/project/strat_anl/traj_online/PARAM2.h
/project/strat_anl/traj_online/PARAM1.h
/project/strat_anl/traj_online/LEGAUGS.h
/project/strat_anl/traj_online/LEGAU.h
/project/strat_anl/traj_online/GRIDP.h
/project/strat_anl/traj_online/COMPSG.h
/project/strat_anl/traj_online/COMGRM.h
/project/strat_anl/traj_online/COMFFT.h
/project/strat_anl/traj_online/CLUSTERS.h
/project/strat_anl/traj_online/CHANS.h
/project/strat_anl/traj_online/BLANK.h

The online trajectory code currently requires the U and V components of the velocity on pressure levels, omega $\left(\frac{dp}{dt}\right)$ on pressure levels, surface pressure, temperature on pressure levels, potential vorticity on pressure levels and specific humidity on pressure levels.

7.2 Information on Parameters

The code “trajmain.F90” gets the required global fields (for the trajectory calculation) from the D1 array and then passes these global fields into the trajectory code, “traj_online.F90”, to calculate particle trajectories. A module “traj_mod.F90” is used by “trajmain.F90” to specify the total number of global fields required from the D1 array and whether they are prognostic fields or diagnostic fields. The parameters used in “traj_mod.F90” are listed in Table 7.1.

Note that if different vertical coordinates were used or different attributes

Table 7.1: Parameters used to specify the global fields required by the online trajectory code.

Name	Value	Description
Ntraj_D1items	7	Total number of global fields required
n_in_progs	0	Number of prognostic fields
n_in_diags0	1	Number of diagnostics from section 0 of the UM
n_in_diags15	1	Number of diagnostics from section 15 of the UM
n_in_diags30	5	Number of diagnostics from section 30 of the UM

to the particles were chosen then the parameters in Table 7.1 would need to be amended in “traj_mod.F90” so they were correct for the global fields required. Also any different required global fields need to be defined in “traj_mod.F90” in terms of their item number and their dimensions.

In “trajmain.F90” the number of vertical levels is hardwired into the code, `pressure_levels= 31`. Therefore any change to the number of levels in the vertical and this part of “trajmain.F90” will need to be addressed. Also in “trajmain.F90” the arrays of the global fields at the current timestep are called `U_global`, `V_global`, `temp_global`, `omega_global`, `pstar_global`, `PV_global` and `wvap_global` (Note that the global fields at the previous timestep are `U_global_last`, `V_global_last`, *etc.*). Consequently any additional meteorological fields attributed to the particles will need to be named in this way and passed into “traj_online.F90” with their item number specified in the subroutine `GETD1FLDS_GLOBAL`.

In “traj_online.F90” the 31 pressure levels are hardwired into an array called `plev` in the subroutine `INIUM`. This is not ideal but during this project our focus was on the science and therefore this was sufficient. In the future, of course, we will aim to make the code more general.

The header files contain important parameters such as the number of particles

(NPART) and the number of attributes (NATTR). It is essential to update the header file PARAM1.h to contain the correct number of particles and attributes. Also the parameters MG and JG are set in PARAM1.h and denote the number of longitudes and the number of latitudes (in one hemisphere) of the model grid respectively. Therefore any changes to the model grid must be updated in PARAM1.h.

7.2.1 Particles Initial Positions

The parameters that control the initial distribution of the particles are shown in Table 7.2.

Table 7.2: Parameters used to specify the initial distribution of particles.

Variable	Value	Description
IPOSN	8	Arrangement of particles: 8 \rightarrow particles spaced conserving area
XCLUSTER	0	Longitude of the 1st particle in degrees
YCLUSTER	88.75	Latitude of the most northern particle in degrees
ZCLUSTER	15000	Pressure level
XSPACE	1.0	Longitudinal spacing in degrees
YSPACE	1.25	Latitudinal spacing in degrees
NXACR	360	Number of particles at the equator
NYACR	143	Number of latitudes particles are initialised on
INISURF	1	Place particles on pressure surfaces

These are defined in the subroutine INITAL and used in the subroutine INI-POSN which sets up the particles initial positions using the parameters defined in INITAL. Also in INIPOSN the vertical level the particles are initialised on is divided by 100000 (*i.e.* the surface pressure). This is hardwired into the code and it is so that the vertical coordinate varies between 0 at the top of the domain

and one at the bottom of the domain.

Note that the online trajectory code is adapted from an offline trajectory code written by John Methven at Reading University in 1997 (Methven, 1997). For more details on any parameters used in the online code please refer to the user guide that accompanies Methven (1997).

7.3 Output

The trajectory output file from the Unified Model is called “trajpos.dat”. It is a binary file and therefore to view and analyse the trajectory output this file must be first converted to a .txt file using the following code:

```
~hadvh/trajposfiles/rwbin.F90
```

The trajectory output, trajpos.dat, contains the particles positions (x,y,z) and their attributes at six hourly time intervals including the initial time. An example of part of the output .txt file is shown below:

```
88.75000000000000  
0.0000000000000000E+000  
3000.000000000000  
212.396654210612  
1.151223190896775E-004  
3.180316617678445E-006  
88.75000000000000  
90.00000000000000  
3000.000000000000
```

215.013426984614
1.148288172503897E-004
3.130772868737320E-006
88.75000000000000
180.00000000000000
3000.000000000000
216.184659200593
1.189594993804640E-004
3.149330456285315E-006

In this case there are six pieces of data for each particle: latitude, longitude, pressure level, temperature, potential vorticity and water vapour. This example is taken from the start of the .txt file and therefore it shows (in this order) the latitude, longitude, pressure level, temperature, potential vorticity and water vapour of particle 1 at the initial time followed by the same six pieces of data for particle 2 at the initial time and again for particle 3 at the initial time and so on.

To view a particular particles position at a given time an IDL code called “trajout.pro” is required (/project/strat_anl/traj_online/trajout.pro). This IDL routine will, given the number of particles, the number of attributes to the particles and the number of timesteps contained in the output file, read the data from the trajectory output .txt file and put it into an array called POSN. The array POSN is such that POSN(number of timesteps, number of particles, number of pieces of data for a particle) where the particle data is given by (x, y, z, attribute 1, attribute 2, attribute 3, ..., attribute n). Therefore the vertical coordinate of particle 1 after two timesteps (*i.e.* after 12 hours) is contained in POSN(2,0,2). Also in trajout.pro there is an example of plotting the trajectory data at $t = 40$ days in the longitude-latitude plane and colouring the particles positions depending on their pressure. This is useful because even though the

particles are plotted in a horizontal plane the colouring gives information about their vertical positions.

Bibliography

- Ambaum, M. H. P., & Hoskins, B. J. 2002. The NAO Troposphere-Stratosphere Connection. *J. Climate*, **15**, 1969–1978.
- Andrews, D. G., Holton, J. R., & Leovy, C. B. 1987. Middle atmosphere dynamics. *Academic Press*.
- Baldwin, M. P., & Dunkerton, T. J. 1999. Propagation of the Arctic Oscillation from the stratosphere to the troposphere. *J. Geophys. Res.*, **104**, 30937–30946.
- Baldwin, M. P., & Dunkerton, T. J. 2001. Stratospheric Harbingers of Anomalous Weather Regimes. *Science*, **294**, 581–584.
- Baldwin, M. P., Gray, L. J., Dunkerton, T. J., Hamilton, K., Haynes, P. H., Randel, W. J., Holton, J. R., Alexander, M. J., Hirota, I., Horinouchi, T., Jones, D. B. A., Kinnersley, J. S., Marquardt, C., Sato, K., & Takahashi, M. 2001. The quasi-biennial oscillation. *Rev. Geophys.*, **39**, 179–230.
- Benney, D., & Bergeron, R. E. 1969. A new class of nonlinear waves in parallel flows. *Stud. Appl. Math.*, **48**, 181–204.
- Black, R. X. 2002. Stratospheric Forcing of Surface Climate in the Arctic Oscillation. *J. Climate*, **15**, 268–277.
- Bretherton, F. P. 1966. Critical Layer Instability in Baroclinic Flows. *Q. J. R. Meteorol. Soc.*, **92**, 325–334.

- Brewer, A. W. 1949. Evidence for a World Circulation Provided by Measurements of Helium and Water Vapour Distribution in the Stratosphere. *Q. J. R. Meteorol. Soc.*, **75**, 351–363.
- Burroughs, W. J., Crowder, B., Robertson, T., Vallie-Talbot, E., & Whitaker, R. 1996. *Weather*. HarperCollinsPublishers.
- Butchart, N., & Remsberg, E. E. 1986. The area of the stratospheric polar vortex as a diagnostic for tracer transport on an isentropic surface. *J. Atmos. Sci.*, **43**, 1319–1339.
- Charlton, A. J., & Polvani, L. M. 2007. A new look at stratospheric sudden warmings. Part I. Climatology and modeling benchmarks. *J. Climate*, **20**, 449–469.
- Charlton, A. J., O’Neill, A., Stephenson, D. B., Lahoz, W. A., & Baldwin, M. P. 2003. Can knowledge of the state of the stratosphere be used to improve statistical forecasts of the troposphere? *Q. J. R. Meteorol. Soc.*, **129**, 3205–3224.
- Charney, J. G., & Drazin, P. G. 1961. Propagation of planetary-scale disturbances from the lower into the upper atmosphere. *J. Geophys. Res.*, **66**, 83–109.
- Davis, R. E. 1969. On the high Reynolds number flow over a wavy boundary. *J. Fluid Mech.*, **36**, 337–346.
- Dickinson, R. E. 1970. Development of a Rossby Wave Critical Level. *J. Atmos. Sci.*, **27**, 627–633.
- Dobson, G. M. B. 1956. Origin and distribution of the polyatomic molecules in the atmosphere. *Proc. R. Soc. Lond.*, **236**, 187–193.
- Dobson, G. M. B., Harrison, D. N., & Lawrence, J. 1929. Measurements of the Amount of Ozone in the Earth’s Atmosphere and Its Relation to Other

- Geophysical Conditions. Part III. *Royal Society of London Proceedings Series A*, **122**, 456–486.
- Drazin, P. G., & Reid, W. H. 2004. *Hydrodynamic Stability*. Cambridge University Press.
- Dritschel, D. G. 1988. Contour surgery: A topological reconnection scheme for extended integrations using contour dynamics. *J. Comp. Phys.*, **77**, 240–266.
- Dritschel, D. G., & Ambaum, M. H. P. 1997. A contour-advective semi-Lagrangian numerical algorithm for simulating fine-scale conservative dynamical fields. *Q. J. R. Meteorol. Soc.*, **123**, 1097–1130.
- Dritschel, D. G., & McIntyre, M. E. 2008. Multiple Jets as PV Staircases: The Phillips Effect and the Resilience of Eddy-Transport Barriers. *J. Atmos. Sci.*, **65**, 855–874.
- Dritschel, D. G., & Saravanan, R. 1994. Three-dimensional quasi-geostrophic contour dynamics, with an application to stratospheric vortex dynamics. *Q. J. R. Meteorol. Soc.*, **120**, 1267–1297.
- Dritschel, D. G., Haynes, P. H., Jukes, M. N., & Shepherd, T. G. 1991. The stability of a two-dimensional vorticity filament under uniform strain. *J. Fluid Mech.*, **230**, 647–665.
- Dunkerton, T. J., & O’Sullivan, D. J. 1996. Mixing zone in the tropical stratosphere above 10 mb. *Geophys. Res. Lett.*, **23**, 2497–2500.
- Dunkerton, T. J., & Scott, R. K. 2008. A Barotropic Model of the Angular Momentum Conserving Potential Vorticity Staircase in Spherical Geometry. *J. Atmos. Sci.*, **65**, 1105–1136.

- Hartmann, D. L., Wallace, J. M., Limpasuvan, V., Thompson, D. W. J., & Holton, J. R. 2000. Can ozone depletion and global warming interact to produce rapid climate change? *Proc. Nat. Acad. Sci. (Wash. DC)*, **97**, 1412–1417.
- Haynes, P. H. 1989. The effect of barotropic instability on the nonlinear evolution of a Rossby-wave critical layer. *J. Fluid Mech.*, **207**, 231–266.
- Haynes, P. H., & McIntyre, M. E. 1987. On the Representation of Rossby Wave Critical Layers and Wave Breaking in Zonally Truncated Models. *J. Atmos. Sci.*, **44**, 2359–2382.
- Haynes, P. H., & Shuckburgh, E. F. 2000a. Effective diffusivity as a diagnostic of atmospheric transport 1. Stratosphere. *J. Geophys. Res.*, **105**, 22777–22794.
- Haynes, P. H., & Shuckburgh, E. F. 2000b. Effective diffusivity as a diagnostic of atmospheric transport 2. Troposphere and lower stratosphere. *J. Geophys. Res.*, **105**, 22795–22810.
- Haynes, P. H., McIntyre, M. E., Shepherd, T. G., Marks, C. J., & Shine, K. P. 1991. On the ‘Downward Control’ of Extratropical Diabatic Circulations by Eddy-Induced Mean Zonal Forces. *J. Atmos. Sci.*, **48**, 651–680.
- Haynes, P. H., Scinocca, J., & Greenslade, M. 2001. Formation and maintenance of the extratropical tropopause by baroclinic eddies. *Geophys. Res. Lett.*, **28**, 4179–4182.
- Hendricks, E. A., & Schubert, W. H. 2009. Transport and mixing in idealized barotropic hurricane-like vortices. *Q. J. R. Meteorol. Soc.*, **135**, 1456–1470.
- Holton, J. R. 2004. An introduction to dynamics meteorology. *Elsevier Academic Press*.
- Holton, J. R., & Lindzen, R. S. 1972. An Updated Theory for the Quasi-Biennial Cycle of the Tropical Stratosphere. *J. Atmos. Sci.*, **29**, 1076–1080.

- Holton, J. R., & Tan, H.-C. 1980. The Influence of the Equatorial Quasi-Biennial Oscillation on the Global Circulation at 50 mb. *J. Atmos. Sci.*, **37**, 2200–2208.
- Hoskins, B. J., McIntyre, M. E., & Robertson, A. W. 1985. On the use and significance of isentropic potential vorticity maps. *Q. J. R. Meteorol. Soc.*, **111**, 877–946.
- Juckes, M. N. 1994. Quasigeostrophic dynamics of the tropopause. *J. Atmos. Sci.*, **51**, 2756–2779.
- Killworth, P. D., & McIntyre, M. E. 1985. Do Rossby-wave critical layers absorb, reflect or over-reflect? *J. Fluid Mech.*, **161**, 449–492.
- Kodera, K., Yamazaki, K., Chiba, M., & Shibata, K. 1990. Downward propagation of upper stratospheric mean zonal wind perturbation to the troposphere. *Geophys. Res. Lett.*, **17**, 1263–1266.
- Kundu, P. J., & Cohen, I. M. 2004. Fluid Mechanics. *Elsevier Academic Press*.
- Kushner, P. J., & Polvani, L. M. 2004. Stratosphere-troposphere coupling in a relatively simple AGCM: the role of eddies. *J. Climate*, **17**, 629–639.
- Lait, L. R. 1994. An Alternative Form for Potential Vorticity. *J. Atmos. Sci.*, **51**, 1754–1759.
- Lindzen, R. S. and Holton, J. R. 1968. A theory of quasi-biennial oscillation. *J. Atmos. Sci.*, **29**, 1095–1107.
- Macaskill, C., Padden, W. E. P., & Dritschel, D. G. 2003. The CASL algorithm for quasi-geostrophic flow in a cylinder. *J. Comp. Phys.*, **188**, 232–251.
- Matsuno, T. 1971. A dynamical model of the stratospheric sudden warming. *J. Atmos. Sci.*, **28**, 1479–1494.

- McIntyre, M. E. 1982. How well do we understand the dynamics of stratospheric warmings? *J. Meteor. Soc. Japan*, **60**, 37–65.
- McIntyre, M. E., & Palmer, T. N. 1983. Breaking planetary waves in the stratosphere. *Nature*, **305**, 593–600.
- McIntyre, M. E., & Palmer, T. N. 1984. The 'surf zone' in the stratosphere. *J. Atmos. Terrest. Phys.*, **46**, 825–849.
- McIntyre, M. E., & Palmer, T. N. 1985. A note on the general concept of wave breaking for rossby and gravity waves. *Pure Appl. Geophys.*, **123**, 964–975.
- Methven, J. 1997. Offline trajectories: Calculation and accuracy. *UGAMP Tech. Rep. 44*, 18.
- Mote, P. W., Rosenlof, K. H., McIntyre, M. E., Carr, E. S., Gille, J. C., Holton, J. R., Kinnerson, J. S., Pumphrey, H. C., Russell, III, J. M., & Waters, J. W. 1996. An atmospheric tape recorder: The imprint of tropical tropopause temperatures on stratospheric water vapor. *J. Geophys. Res.*, **101**, 3989–4006.
- Muller, J. C. 1991. Baroclinic instability in a two-layer, vertically semi-infinite domain. *Tellus A*, **43**, 275–284.
- Nakamura, N. 1996. Two-dimensional mixing, edge formation, and permeability diagnosed in an area coordinate. *J. Atmos. Sci.*, **53**, 1524–1537.
- Neu, J. L., & Plumb, A. R. 1999. Age of air in a "leaky pipe" model of stratospheric transport. *J. Geophys. Res.*, **104**, 19243–19255.
- Plumb, A. R. 1996. A "tropical pipe" model of stratospheric transport. *J. Geophys. Res.*, **101**, 3957–3972.
- Plumb, R. A., & McEwan, A. D. 1978. The Instability of a Forced Standing Wave in a Viscous Stratified Fluid: A Laboratory Analogue of the Quasi-Biennial Oscillation. *J. Atmos. Sci.*, **35**, 1827–1839.

- Polvani, L. M., & Kushner, P. J. 2002. Tropospheric response to stratospheric perturbations in a relatively simple general circulation model. *Geophys. Res. Lett.*, **29**, 18-1-18-4.
- Polvani, L. M., & Saravanan, R. 2000. The Three-Dimensional Structure of Breaking Rossby Waves in the Polar Wintertime Stratosphere. *J. Atmos. Sci.*, **57**, 3663-3685.
- Punge, H. J., Konopka, P., Giorgetta, M. A., & Muller, R. 2009. Effects of the quasi-biennial oscillation on low-latitude transport in the stratosphere derived from trajectory calculations. *J. Geophys. Res.*, **114**, D03102, 16 PP.
- Ray, E. A., Moore, F. L., Rosenlof, K. H., Davis, S. M., Boenisch, H., Morgenstern, O., Smale, D., Rozanov, E., Hegglin, M., Pitari, G., Mancini, E., Braesicke, P., Butchart, N., Hardiman, S., Li, F., Shibata, K., & Plummer, D. A. 2010. Evidence for changes in stratospheric transport and mixing over the past three decades based on multiple data sets and tropical leaky pipe analysis. *J. Geophys. Res.*, **115**, D21304, 16 PP.
- Scaife, A. A., & Knight, J. R. 2008. Ensemble simulations of the cold European winter of 2005-2006. *Q. J. R. Meteorol. Soc.*, **134**, 1647-1659.
- Schneider, T., Held, I. M., & Garner, S. T. 2003. Boundary Effects in Potential Vorticity Dynamics. *J. Atmos. Sci.*, **60**, 1024-1040.
- Scott, R. K., & Dritschel, D. G. 2005. Downward wave propagation on the polar vortex. *J. Atmos. Sci.*, **62**, 3382-3395.
- Scott, R. K., Shuckburgh, E. F., Cammas, J. P., & Legras, B. 2003. Stretching rates and equivalent length near the tropopause. *J. Geophys. Res.*, **108**, 4394.
- Shepherd, T. G. 2002. Issues in Stratosphere-troposphere Coupling. *J. Meteor. Soc. Japan*, **80**, 769-792.

- Shindell, D. T., Rind, D., Balachandran, N., Lean, J., & Lonergan, P. 1999. Solar cycle variability, ozone, and climate. *Science*, **284**, 305–308.
- Shindell, D. T., Schmidt, G.A., Mann, M. E., Rind, D., & Waple, A. 2001. Solar forcing of regional climate change during the maunder minimum. *Science*, **294**, 2149–2152.
- Shuckburgh, E. F., & Haynes, P. H. 2003. Diagnosing transport and mixing using a tracer-based coordinate system. *Phys. Fluids*, **15**, 3342–3357.
- Shuckburgh, E. F., Norton, W., Iwi, A., & Haynes, P. H. 2001. Influence of the quasi-biennial oscillation on isentropic transport and mixing in the tropics and subtropics. *J. Geophys. Res.*, **106**, 14327–14337.
- Smy, L. A., & Scott, R. K. 2009. The influence of stratospheric potential vorticity on baroclinic instability. *Q. J. R. Meteorol. Soc.*, **135**, 1673–1683.
- Solomon, S., Kiehl, J. T., Garcia, R. R., & Grose, W. 1986. Tracer Transport by the Diabatic Circulation Deduced from Satellite Observations. *J. Atmos. Sci.*, **43**, 1603–1642.
- Song, Y., & Robinson, W. A. 2004. Dynamical mechanisms for stratospheric influences on the troposphere. *J. Atmos. Sci.*, **61**, 1711–1725.
- Stewartson, K. 1978. The evolution of the critical layer of a Rossby-wave. *Geophys. Astrophys. Fluid Dyn.*, **9**, 185–200.
- Stewartson, K. 1981. Marginally stable inviscid flows with critical layers. *IMA J. Appl. Maths.*, **27**, 133–175.
- Thompson, D. W. J., & Wallace, J. M. 1998. The arctic oscillation signature in the wintertime geopotential height and temperature fields. *Geophys. Res. Lett.*, **25**, 1297–1300.

- Thompson, D. W. J., & Wallace, J. M. 2000. Annular modes in the extratropical circulation. Part 1: Month-to-month variability. *J. Climate*, **13**, 1000–1016.
- Thompson, D. W. J., Baldwin, M. P., & Wallace, J. M. 2002. Stratospheric connection to northern hemisphere wintertime weather: implications for prediction. *J. Climate*, **15**, 1421–1428.
- Thompson, D. W. J., Furtado, J. C., & Shepherd, T. G. 2006. On the tropospheric response to anomalous stratospheric wave drag and radiative heating. *J. Atmos. Sci.*, **63**, 2616–2629.
- Thorncroft, C. D., Hoskins, B. J., & McIntyre, M. E. 1993. Two paradigms of baroclinic-wave life-cycle behaviour. *Q. J. R. Meteorol. Soc.*, **119**, 17–55.
- Volk, C. M., Elkins, J. W., Fahey, D. W., Salawitch, R. J., Dutton, G. S., Gilligan, J. M., Proffitt, M. H., Loewenstein, M., Podolske, J. R., Minschwaner, K., Margitan, J. J., & Chan, K. R. 1996. Quantifying Transport between the Tropical and Mid-Latitude Lower Stratosphere. *Science*, **272**, 1763–1768.
- Warn, T., & Warn, H. 1978. The evolution of a nonlinear critical level. *Stud. Appl. Maths*, **59**, 37–71.
- Waugh, D. W. 1996. Seasonal variation of isentropic transport out of the tropical stratosphere. *J. Geophys. Res.*, **101**, 4007–4024.
- Wittman, M. A. H., Polvani, L. M., Scott, R. K., & Charlton, A. J. 2004. Stratospheric influence on baroclinic lifecycles and its connection to the Arctic Oscillation. *Geophys. Res. Lett.*, **31**, L16113.
- Wittman, M. A. H., Charlton, A. J., & Polvani, L. M. 2007. The effect of lower stratospheric shear on baroclinic instability. *J. Atmos. Sci.*, **64**, 479–496.

WMO. 2007. *Scientific Assessment of Ozone Depletion: 2006. (WMO Global Ozone Research and Monitoring Project Report No. 50)*. Geneva: World Meteorol. Org.

Yulaeva, E., Holton, J. R., & Wallace, J. M. 1994. On the cause of the annual cycle in tropical lower stratospheric temperatures. *J. Atmos. Sci.*, **51**, 167–174.